

A TDDFT Computational Study of Platinum Complexes Bound to Nucleobases

Golda Mensa-Bonsu

MSc by Research

University of York

Chemistry

January 2016

Abstract

The electronic spectra of a number of platinum (II) complexes bound to single nucleobases have been investigated using Time-Dependent Density Functional Theory (TDDFT). The calculated spectra obtained in this work have been benchmarked against recent gas-phase photo-dissociation spectra of platinum complex-nucleobase clusters. UV spectra have been calculated for a range of density functionals and basis sets to determine the best functional-basis set combination for reproducing the experimental spectra.

The first series of TDDFT calculations conducted in this work investigated the electronic transitions of iodide ion-nucleobase clusters and their constituent “monomer” parts (i.e. the isolated iodide anion and isolated nucleobases). Calculations on the $I \cdot Nu$ clusters (Nu = Uracil, Thymine or Adenine) and isolated uracil, cytosine, thymine and adenine produced computed UV spectra and the associated electronic transitions were characterised by inspection of respective molecular orbitals. For the nucleobases, these orbitals were revealed to be mainly of $\pi \rightarrow \pi^*$ character. The electronic transitions of the $I \cdot Nu$ clusters were dominated by excitations involving orbitals localised on the nucleobases.

A second series of studies focused on the electronic transitions of isolated platinum (II) and platinum (IV) cyanide complexes as well as their clusters involving a single water molecule. The excited states of the $Pt(CN)_{4,6}^{2-} \cdot H_2O$ complexes were found to involve only platinum localised orbitals. The final set of TDDFT calculations were performed on $Pt(CN)_{4,6}^{2-} \cdot M$ complexes (M = Uracil or Cytosine). The electronic transitions occurring in the $Pt(CN)_4^{2-} \cdot Uracil$ and $Pt(CN)_4^{2-} \cdot Cytosine$ complexes were found to be of a short-range charge transfer nature. Conversely, the electronic transitions of $Pt(CN)_4^{2-} \cdot Uracil$ involved uracil localised orbitals that were of $\pi \rightarrow \pi^*$ character.

Contents

Abstract.....	<i>ii</i>
Contents.....	<i>iii</i>
List of Figures.....	<i>vi</i>
List of Tables.....	<i>xi</i>
Author's Declaration.....	<i>xiv</i>
Chapter 1: Introduction.....	1
1.1 The Study of Biological Ions in the Gas Phase.....	1
1.2 Electronic Spectroscopy of Biological Ions in the Gas Phase.....	2
1.3 Computational Methods for the Study of Biological Ions the Gas Phase.....	3
1.4 Platinum Based Complexes as Anticancer Agents.....	6
1.5 Overview of Thesis	9
Chapter 2: Computational Methods.....	10
2.1 Density Functional Theory.....	10
2.2 Density Functionals.....	14

2.3	Time Dependent Density Functional Theory.....	16
2.4	Basis Sets.....	18
2.5	Solvation Models.....	23
2.6	Computational Details.....	26
Chapter 3: A TDDFT Computational Study of Iodide Ion-Nucleobase Complexes.....		27
3.1	Introduction.....	27
3.2	Computational Methods.....	28
3.3	Results and Discussion.....	29
3.3.1	Iodide.....	29
3.3.2	Isolated Nucleobases.....	30
3.3.2.a	Uracil.....	30
3.3.2.b	Cytosine.....	40
3.3.2.c	Thymine.....	47
3.3.2.d	Adenine.....	52
3.3.3	I ⁻ Nu Complexes.....	58
3.3.3.a	Iodide-Uracil.....	58
3.3.3.b	Iodide-Thymine.....	63
3.3.3.c	Iodide-Adenine.....	67
3.4	Conclusion.....	70

Chapter 4: A TDDFT computational study of platinum (II) complexes bound water.....	72
4.1 Introduction.....	72
4.2 Computational Methods.....	73
4.3 Results and Discussion.....	74
4.3.1 Platinum (II) Tetracyanide.....	74
4.3.2 Platinum (IV) Hexacyanide.....	84
4.3.3 Platinum (II) Tetracyanide·Water	89
4.4 Conclusion.....	93
Chapter 5: A TDDFT computational study of platinum (II) and (IV) complexes bound to a single nucleobase.....	94
5.1 Introduction.....	94
5.2 Computational Methods.....	96
5.3 Results and Discussion.....	97
5.3.1 Pt(CN) ₄ ²⁻ ·uracil.....	97
5.3.2 Pt(CN) ₄ ²⁻ ·cytosine.....	107
5.3.3 Pt(CN) ₆ ²⁻ ·uracil.....	116
5.4 Conclusion.....	121
References.....	122

List of Figures

Chapter 3: A TDDFT Computational Study of Iodide Ion-Nucleobase Complexes

Figure 3.1	The B3LYP/LANL2DZ optimised ground state structures of a) uracil b) cytosine c) thymine d) adenine. The magnitude and direction of the dipole moments of these nucleobases are represented by the blue vector.	30
Figure 3.2	Comparison of the computational and experimental UV spectra of uracil: —— Experimental UV spectrum (courtesy of Sen et al.) - - - - B3LYP/LANL2DZ, ——— M062X/LANL2DZ andM11/ LANL2DZ.....	32
Figure 3.3	Comparison of the theoretical and experimental UV spectra of uracil: —— Experimental UV spectrum (courtesy of Sen et al.), ——— B3LYP/Def2- TZVPP and MN12-SX/Def2-TZVPP.....	35
Figure 3.4	Comparison of the experimental and theoretical electronic spectra of uracil: —— Experimental aqueous UV absorption (courtesy of Sen et al.), ——— Gas phase B3LYP/LANL2DZ (10 states) and Solution phase IEFPCM/B3LYP/LANL2DZ (10 states).....	37
Figure 3.5	Experimental aqueous UV absorption spectrum of uracil (courtesy of Sen et al.).....	38
Figure 3.6	MOs involved in the electronic transitions of uracil. MOs were calculated at the B3LYP/LANL2DZ level of theory.....	39
Figure 3.7	Comparison of the theoretical and experimental UV spectra of cytosine: —— Experimental UV spectrum (courtesy of Sen et al.), ——— M062X/LANL2DZ and M11/LANL2DZ.....	42
Figure 3.8	Comparison of the experimental and theoretical electronic spectra of cytosine: —— Experimental aqueous UV absorption (courtesy of Sen et al.), ——— Gas phase B3LYP/LANL2DZ (10 states) and Solution phase IEFPCM/B3LYP/LANL2DZ (10 states).....	44
Figure 3.9	MOs involved in the electronic transitions of cytosine. MOs were calculated at the B3LYP/LANL2DZ level of theory.....	46
Figure 3.10	Comparison of the experimental and theoretical electronic spectra of thymine: —— Experimental aqueous UV absorption (courtesy of Sen et al.), ——— M11/ LANL2DZ, - - - B3LYP/LANL2DZ and M062X/LANL2DZ.....	48
Figure 3.11	MOs involved in the electronic transitions of thymine. MOs were calculated at the B3LYP/LANL2DZ level of theory.....	50







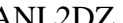

Figure 3.12	Comparison of the experimental and theoretical electronic spectra of thymine: ———— Experimental aqueous UV absorption (courtesy of Sen et al.), ———— Gas phase B3LYP/LANL2DZ (10 states) and ······· Solution phase IEFPCM/B3LYP/LANL2DZ (10 states).....	52
Figure 3.13	Comparison of the experimental and theoretical electronic spectra of adenine: ———— Experimental aqueous UV absorption (courtesy of Sen et al.) and ———— B3LYP/LANL2DZ	54
Figure 3.14	Comparison of the experimental and theoretical electronic spectra of adenine: ———— Experimental aqueous UV absorption (courtesy of Sen et al.), ———— Gas phase B3LYP/LANL2DZ (10 states) and ······· Solution phase IEFPCM/B3LYP/LANL2DZ (10 states)	55
Figure 3.15	MOs involved in the electronic transitions of adenine. MOs were calculated at the B3LYP/LANL2DZ level of theory.....	57
Figure 3.16	The B3LYP/LANL2DZ optimised ground state structures of I·Ur. Hydrogen bonds are indicated with a dashed line with bond distances in Å.....	58
Figure 3.17	Comparison of the experimental and theoretical electronic spectra of I·Ur: · Experimental photodepletion (absorption) spectrum (unpublished work courtesy of Yoshikawa et al.), ———— Band profile for photodepletion (absorption) spectrum and ———— B3LYP/LANL2DZ (50 states).....	60
Figure 3.18	MOs involved in the electronic transitions of I·uracil. MOs were calculated at the B3LYP/LANL2DZ level of theory.....	62
Figure 3.19	The B3LYP/LANL2DZ optimised ground state structures of I·thymine. Hydrogen bonds are indicated with a dashed line with bond distances in Å.....	63
Figure 3.20	Comparison of the experimental and theoretical electronic spectra of I·Thy: · Experimental photodepletion (absorption) data (unpublished work courtesy of Yoshikawa et al.), ———— Band profile for the photodepletion (absorption) spectrum and ———— B3LYP/LANL2DZ (30 states).....	65
Figure 3.21	MOs involved in the electronic transitions of I·thymine. MOs were calculated at the B3LYP/LANL2DZ level of theory.....	66
Figure 3.22	The B3LYP/LANL2DZ optimised ground state structures of I·adenine. Hydrogen bonds are indicated with a dashed line with bond distances in Å...67	67
Figure 3.23	Computed UV spectrum of I·Adenine, calculated at 50 states using B3LYP/LANL2DZ.....	68
Figure 3.22	MOs involved in the electronic transitions of I·Adenine. MOs were calculated at the B3LYP/LANL2DZ level of theory.....	69

Chapter 4: A TDDFT computational study of platinum (II) complexes bound water

Figure 4.1	Experimental gas phase photodepletion (absorption) spectrum of $\text{Pt}(\text{CN})_4^{2-}$. (Courtesy of Sen et al.).....	75
Figure 4.2	Comparison of the experimental and theoretical electronic spectra of $\text{Pt}(\text{CN})_4^{2-}$: \diamond Experimental photodepletion (absorption) spectrum (courtesy of Sen et al.), ⁴³ ———— Band profile for photodepletion spectrum B3LYP/SDD (ECP) and - - - - PBE0/SDD (ECP).....	78
Figure 4.3	Comparison of the experimental and theoretical electronic spectra of $\text{Pt}(\text{CN})_4^{2-}$: \diamond Experimental photodepletion (absorption) spectrum (courtesy of Sen et al.), ⁴³ ———— Band profile for photodepletion spectrum, - - - - MN12-SX/SDD (ECP), B3LYP/ LANL2DZ (ECP) and ———— B3LYP/SDD(ECP).....	79
Figure 4.4	Comparison of the theoretical and experimental electronic spectra of $\text{Pt}(\text{CN})_4^{2-}$: \diamond Experimental photodepletion spectrum (courtesy of Sen et al.), ⁴³ ———— Band profile for photodepletion spectrum, M11/Def2-TZVPP (ECP) and - - - B3LYP/Def2-TZVPP (ECP).....	80
Figure 4.5	MOs involved in the electronic transitions of $\text{Pt}(\text{CN})_4^{2-}$. MOs have been calculated at the MN12-SX /LANL2DZ level of theory.....	81
Figure 4.6	Comparison of the solution and gas phase experimental UV spectra of $\text{Pt}(\text{CN})_4^{2-}$: ———— Aqueous absorption spectrum and \bullet Photodepletion (absorption) spectrum. The solid black line is a tentative band profile for the photodepletion spectrum.....	82
Figure 4.7	Comparison of the computed and experimental absorption spectra of $\text{Pt}(\text{CN})_4^{2-}$: ———— Solution-phase absorption spectrum produced by IEFPCM/MN12-SX/LANL2DZ, Gas-phase absorption spectrum produced by MN12-SX/LANL2DZ, ———— Aqueous experimental UV spectrum.....	83
Figure 4.8	Theoretical UV spectrum of $\text{Pt}(\text{CN})_6^{2-}$ generated using LANL2DZ and the following functionals: - - - B3LYP(50 States), ———— PBE0 (50 States) and ———— MN12-SX (90 states).....	85
Figure 4.9	Aqueous experimental absorption spectrum of $\text{Pt}(\text{CN})_6^{2-}$ (courtesy of Sen et al.).....	86
Figure 4.10	MOs involved in the electronic transitions of $\text{Pt}(\text{CN})_6^{2-}$, calculated at the MN12-SX/LANL2DZ level of theory.....	88
Figure 4.10	MN12-SX/LANL2DZ optimised ground state geometry of $\text{Pt}(\text{CN})_4^{2-}\cdot\text{H}_2\text{O}$...	89
Figure 4.11	Comparison of the theoretical UV spectra produced using the following functionals and LANL2DZ: - - - PBE0, ———— B3LYP and ———— MN12-SX	90

Chapter 5: A TDDFT computational study of platinum (II) and (IV) complexes bound to a single nucleobase

Figure 5.1	Ground state B3LYP/LANL2DZ optimised geometry of Pt(CN) ₄ ²⁻ ·Uracil. Hydrogen bonds are indicated as dashed lines and bond lengths are in Angstroms.....	97
Figure 5.2	Comparison between the computed and experimental electronic spectra of Pt(CN) ₄ ²⁻ ·Uracil: • Photodepletion (absorption) spectrum (courtesy of Sen et al.), ⁴¹ — Band profile for photodepletion (absorption) spectrum, — MN12-SX/LANL2DZ (ECP) (90 states).....	100
Figure 5.3	Comparison between the computed and experimental electronic spectra of Pt(CN) ₄ ²⁻ ·Uracil: ◊ Photodepletion (absorption) spectrum (courtesy of Sen et al.), ⁴¹ — Band profile for photodepletion (absorption) spectrum, B3LYP/SDD (ECP) (50 states) and — B3LYP/LANL2DZ (50 states).....	101
Figure 5.4	Comparison between the computed and experimental electronic spectra of Pt(CN) ₄ ²⁻ ·Uracil: ◊ Photodepletion (absorption) spectrum (courtesy of Sen et al.), ⁴¹ — Band profile for photodepletion (absorption) spectrum, MN12-SX/Def2-TZVPP (ECP) (50 states) and — B3LYP/Def2-TZVPP (ECP) (50 states).....	102
Figure 5.5	Error in excitation energy plotted against Λ values for TDDFT calculations employing the following functionals: (a) PBE (b) B3LYP and (c) CAM-B3LYP. Each point represents a single excitation: (Δ) local excitations, (\times) Rydberg excitations, and (\bullet) charge- transfer excitations. This figure has been reproduced from Ref [134].....	104
Figure 5.6	Comparison between the computed and experimental electronic spectra of Pt(CN) ₄ ²⁻ ·Uracil: ◊ Photodepletion (absorption) spectrum (courtesy of Sen et al.), ⁴¹ — Band profile for photodepletion (absorption) spectrum,M11/LANL2DZ (50 states) and — B3LYP/LANL2DZ (50 states).....	105
Figure 5.7	Molecular orbitals involved in the electronic transitions of Pt(CN) ₄ ²⁻ ·Uracil. MOs were calculated at the B3LYP/LANL2DZ level of theory.....	107
Figure 5.8	B3LYP/LANL2DZ optimised ground state geometry of Pt(CN) ₄ ²⁻ ·Cytosine. Hydrogen bonds are indicated as dashed lines and bond distances are in Angstroms.....	108
Figure 5.9	Comparison of the computed and experimental UV spectra of Pt(CN) ₄ ²⁻ ·cytosine: ◊ Photodepletion (absorption) spectrum (courtesy of Sen et al.), ⁴³ — Band profile for photodepletion (absorption) spectrum, MN12-SX/SDD (ECP) (50 states) and — MN12-SX/LANL2DZ (50 states).....	110
Figure 5.10	Comparison of the computed and experimental UV spectra of Pt(CN) ₄ ²⁻ ·cytosine: ◊ Photodepletion (absorption) spectrum (courtesy of Sen et al.), ⁴³ — Band profile for photodepletion (absorption) spectrum,	

	B3LYP/LANL2DZ (50 states) and  B3LYP/SDD (ECP) (50 states).....	111
Figure 5.11	Comparison of the computed and experimental UV spectra of Pt(CN) ₄ ²⁻ ·Cytosine:  Photodepletion (absorption) spectrum (courtesy of Sen et al.), ⁴³  Band profile for photodepletion (absorption) spectrum,  PBE0/LANL2DZ (ECP) (90 states) and  B3LYP/LANL2DZ (ECP) (90 states).....	113
Figure 5.12	MOs involved in the electronic transitions of Pt(CN) ₄ ²⁻ ·Cytosine. MOs were calculate using B3LYP/LANL2DZ.....	115
Figure 5.13	Ground state structure of B3LYP/LANL2DZ optimised Pt(CN) ₆ ²⁻ ·Uracil.....	116
Figure 5.14	Comparison of the computed UV spectra of Pt(CN) ₆ ²⁻ ·Uracil:  B3LYP/LANL2DZ,  M062X/LANL2DZ and  CAM-B3LYP/LANL2DZ.....	118
Figure 5.15	MOs involved in the electronic transitions of Pt(CN) ₆ ²⁻ ·Uracil. MOs were calculated at the B3LYP/LANL2DZ level of theory	120

List of Tables

Chapter 3: A TDDFT Computational Study of Iodide Ion-Nucleobase Complexes

Table 3.1	Computed and experimental excitation energies (in eV) of uracil.....	31
Table 3.2	Mean absolute errors in excitation energy (eV) associated with TDDFT/LANL2DZ calculations of uracil at 10 states.....	31
Table 3.3	Mean absolute errors in excitation energy (eV) associated with TDDFT calculations of uracil at 10 states.....	34
Table 3.4	Comparison of the computed excitation energies of uracil (<i>in vacuo</i> and solution) with experimental results.....	36
Table 3.5	Assignment of the four lowest energy excited state transitions of uracil using B3LYP/LANL2DZ data.....	38
Table 3.6	Computed and experimental excitation energies of cytosine.....	40
Table 3.7	Mean absolute errors in excitation energy (eV) associated with TDDFT calculations of cytosine at 10 states.....	41
Table 3.8	Comparison of the computed excitation energies of cytosine (<i>in vacuo</i> and solution) with experimental results.....	43
Table 3.9	Assignment of the three lowest energy excited state transition of cytosine using B3LYP/LANL2DZ.....	45
Table 3.10	Computed and experimental excitation energies of thymine.....	47
Table 3.11	Mean absolute errors in excitation energy (eV) associated with TDDFT/LANL2DZ calculations of thymine at 10 states.....	48
Table 3.12	Assignment of the three lowest energy excited state transitions of thymine using B3LYP/LANL2DZ data.....	49
Table 3.13	Comparison of the computed excitation energies of thymine (<i>in vacuo</i> and solution) with experimental results.....	51
Table 3.14	Computed and experimental excitation energies for adenine.....	53
Table 3.15	Mean absolute errors in excitation energy (eV) associated with TDDFT/LANL2DZ calculations of adenine at 20 states.....	53
Table 3.16	Comparison of the experimental and computational excitation energies (<i>in vacuo</i> and solution phase) of adenine.....	55

Table 3.17	The assignment of the three lowest energy excited state transitions occurring in adenine using B3LYP/LANL2DZ data.....	56
Table 3.18	Computed and experimental excitation energies of I·Ur at 50 states.....	59
Table 3.19	Mean absolute errors in excitation energy (eV) associated with TDDFT/LANL2DZ calculations of I·Ur at 50 states.....	59
Table 3.20	Assignment of the four lowest energy excited state transitions of I·Uracil using B3LYP/LANL2DZ data.....	61
Table 3.21	Computed and experimental excitation energies of I·thymine at 30 states.....	64
Table 3.22	Mean absolute errors in excitation energy (eV) associated with TDDFT/LANL2DZ calculations of I·thymine at 30 states.....	64
Table 3.23	Assignment of the four lowest energy excited state transitions of I·thymine using B3LYP/LANL2DZ data.....	65
Table 3.24	Computed excitation energies of I·adenine at 50 states using LANL2DZ....	68
Table 3.25	The assignment of the three lowest energy excited state transitions occurring in I·adenine using B3LYP/LANL2DZ data.....	69

Chapter 4: A TDDFT computational study of platinum (II) complexes bound water

Table 4.1	Comparison between the theoretical excitation energies obtained using TDDFT at 30 states and the experimental, gas phase results (in eV) of Pt(CN) ₄ ²⁻	76
Table 4.2	The mean absolute errors in excitation energy (eV) of Pt(CN) ₄ ²⁻	76
Table 4.3	Assignment of the vertical excitations of Pt(CN) ₄ ²⁻ using MN12-SX/LANL2DZ data.....	82
Table 4.4	Comparison of the experimental and computed excitation energies of Pt(CN) ₄ ²⁻ (in vacuo and solution).....	83
Table 4.5	Comparison between the computed and experimental excitation energies of Pt(CN) ₆ ²⁻	86
Table 4.6	Assignment of the vertical excitations of Pt(CN) ₆ ²⁻ using MN12-SX/LANL2DZ data.....	87
Table 4.7	Comparison between the computed excitation energies of Pt(CN) ₄ ²⁻ ·H ₂ O produced using TDDFT at 20 States.....	90
Table 4.8	Assignment of the electronic transitions of Pt(CN) ₄ ²⁻ ·H ₂ O.....	91
Table 4.9	A comparison between the MOs of Pt(CN) ₄ ²⁻ and Pt(CN) ₄ ²⁻ ·H ₂ O which are involved in the excited state transitions.....	92

Chapter 5: A TDDFT computational study of platinum (II) and (IV) complexes bound to a single nucleobase

Table 5.1	Selected bond distances (Å) in the B3LYP/LANL2DZ optimised geometry of Pt(CN) ₄ ²⁻ ·uracil.....	98
Table 5.2	Comparison between the theoretical excitation energies obtained using TDDFT and the experimental, gas phase results (in eV) of Pt(CN) ₄ ²⁻ ·uracil...99	99
Table 5.3	The mean absolute errors in excitation energy (eV) of Pt(CN) ₄ ²⁻ ·uracil.....99	99
Table 5.4	Assignment of the electronic transitions of Pt(CN) ₄ ²⁻ ·uracil. Excitation energies have been calculated using B3LYP/LANL2DZ.....	106
Table 5.5	Key bond distances (Å) in the B3LYP/LANL2DZ optimised geometry of Pt(CN) ₄ ²⁻ ·cytosine.....	108
Table 5.6	Comparison between the theoretical excitation energies obtained using TDDFT and the experimental, gas phase results (in eV) of Pt(CN) ₄ ²⁻ ·Cy....	109
Table 5.7	The mean absolute errors in excitation energy (eV) of Pt(CN) ₄ ²⁻ ·Cy.....	109
Table 5.8	Assignment of the electronic transitions of Pt(CN) ₄ ²⁻ ·cytosine using TD-B3LYP/LANL2DZ results.....	114
Table 5.9	Selected bond distances (Å) in the B3LYP/LANL2DZ optimised geometry of Pt(CN) ₆ ²⁻ ·uracil.....	116
Table 5.10	Comparison between the computed and experimental excitation energies of Pt(CN) ₆ ²⁻ ·uracil.....	117
Table 5.11	Mean absolute error in excitation energies (eV) for Pt(CN) ₆ ²⁻ ·uracil.....	117
Table 5.12	Assignment of the vertical excitations of Pt(CN) ₆ ²⁻ ·uracil using B3LYP/LANL2DZ data.....	119

Author's Declaration

I hereby certify that the research presented in this thesis is my own and to the best of my knowledge, is original except where due reference has been made to others. This work has not previously been presented for an award at this, or any other, University. All sources are acknowledged as References.

Chapter 1

Introduction

1.1 The Study of Biological Ions in the Gas Phase

Due to the well-established relationship between structure and function, the study of biologically relevant ions remains a significantly active area of research. It is expected that, through the characterisation of their geometric and electronic structures and dynamics, a unique perspective can be gained into the role of these biological molecules. Studying these species in the gas phase may initially appear counter intuitive, as most reactions involving biological ions occur within condensed phases. However, some biological activity occurs deep within proteins where solvent is absent. In addition, examination of these systems in isolation simplifies the complex native environment, allowing the initial studies of the intrinsic properties.¹

The rapid advances of computational and experimental methods has provided a means to probe the gas-phase properties of biological ions with efficiency. Over the last decade, density functional theory using popular functional such as B3LYP have been widely applied to calculate structures of bioions.² Conversely, the creation of experimental techniques such as femtosecond photoelectron spectroscopy has allowed the

photodynamics of these systems to be followed on a very small timescale.³ In this introductory chapter, a selection of the experimental and computational methods at our disposal will be reviewed, with cases of previous gas-phase studies of biomolecules also presented. The clinical context in which this work has taken place will also be explored.

1.2 Electronic Spectroscopy of Biological Ions in the Gas Phase

Information regarding the structure and excited-state dynamics of biological ions can be obtained through the use of electronic spectroscopy. Optical spectroscopic methods have been facilitated by the common availability of tunable dye lasers and OPO lasers have allowed for the collection of high-quality ultraviolet (UV) and fluorescence spectra.⁴

Aromatic amino acids and DNA bases are two biological systems which have been studied extensively in the gas phase using UV spectroscopy.⁵⁻⁸ Exposure to UV radiation can cause critical damage to peptides and proteins within the body, so the photodynamics of their chromophores have been intensively explored.⁹ The first gas-phase UV spectroscopic study in this area is widely acknowledged to have been produced by Levy et al. in 1985,⁵ in which supersonic molecular beams were used to prepare tryptophan. More recent work by Rizzo et al. has focused on the elucidation of the photofragmentation mechanism of gas phase peptides.⁶ Rosu et al. have used UV spectroscopy to gain insight into the photoreactivity of model DNA strands, producing for quadruplex, single and double stranded DNA in the gas-phase.⁷ In a separate series of experiments, fluorescence resonance energy transfer has been employed to examine the conformations of polyproline peptides by Jockusch et al.⁸

Photoelectron spectroscopy (PES) can provide an insight in to the composition and electronic states of ions through the determination of quantities such the electron binding energy and angular distributions of the electrons.⁹ There are a range of PES techniques which incorporate lasers including Ultraviolet Photoelectron Spectroscopy (UPS) and time resolved PES.¹⁰ The biological marker, green fluorescent protein (GFP) has been intensively studied over recent years using this technique.¹¹ Mooney et al. employed femtosecond time-resolved PES to follow the dynamics of the GFP chromophore, while Verlet et al. have utilised UPS to investigate its vertical and adiabatic detachment energies.^{12,13}

Several studies have used time resolved PES to investigate the photophysical properties of nucleobases. Femtosecond time resolved PES has previously been employed by Ullrich et al. to investigate the electronic relaxation dynamics of the following nucleobases, which had been isolated in a molecular beam: adenine, thymine, cytosine and uracil.¹⁴ Chatterley et al used time resolved PES to elucidate relaxation dynamics of various adenosine nucleotides and found that the decay mechanism was characterised by internal conversion from the $\pi\pi^*$ state to the electronic ground state.¹⁵

1.3 Computational Methods for the Study of Biological Ions the Gas Phase

The experimental studies described above are frequently supported by accompanying theoretical studies. The inclusion of computational work in experimental studies primarily serves as a tool to fully interpret the experimental results. However, there is a synergy between experimental gas-phase studies and computational chemistry as the

experiments provide important benchmarking data for testing the applicability of computational methods. In addition, computational methods can allow the analysis of systems for experimental data cannot be easily obtained. This is illustrated in a study by De Leon et al., in which density functional theory (DFT) calculations were used to probe binding properties of fullerenes with amino acids.¹⁶

For the analysis of biological ions, the quantum mechanical methods at disposal range from the lower level semi empirical methods to more accurate levels of theory such as Coupled Cluster.¹⁷ Theoretical studies usually commence with an investigation of the relevant molecule's conformational space using lower levels of theory. Previous studies have shown that post Hartree-Fock methods such as Møller-Plesset perturbation theory (MP n) can be used successfully in this initial identification.^{18,19} Cassady et al. previously used to MP2 level calculations in the conformational search of several gas-phase amide acidities, deducing that the lowest energy conformer was *cis* in nature.²⁰

The main limitation of MP n methods is its inability to describe the properties of systems with complex and atypical electronic structures.¹⁷ A higher level of accuracy can be attained for such systems, through the use of Quadratic Configuration Interaction and Coupled Cluster methods including QCISD(T) and CCSD(T). These methods take into account more rigorously, the effects arising from electron correlation such as dispersion forces.^{21,22} Hobza et al. have utilised CCSD(T) for the study of an anisole dimer (in which dispersion forces are prevalent), producing binding energies with a high degree of accuracy.²³ It is for this reason that CCSD is commonly referred to as the “gold standard”

of theoretical methods.²⁴ However for both QCISD(T) and CCSD(T), the computational expense associated with performing calculations on even modestly large molecules is often high. Therefore, its use is mainly limited to small and medium sized species such as individual nucleobases.²⁵

For larger systems, Density Functional Theory (DFT) provides a credible alternative for the analysis of the predominantly ground state properties of biomolecules. Facilitated by the advent of exchange correlation hybrid functionals, the electron density based method has undergone a rapid expansion in use in recent years.¹⁷ Prior to this development, DFT was viewed as too inaccurate due to its neglect of electron correlation and exchange interaction and was rejected in favour of its wave function based predecessors. Through the examination of glycine and alanine acidities in the gas phase, Toscano et al. demonstrated that B3LYP is capable providing a satisfactory balance between accuracy, computational cost and time.²⁶

While DFT can be used to describe the ground state properties of systems containing up to 200 atoms, the accuracy of the results can often be reduced in larger systems due to the failure of standard hybrid functionals to account for the London dispersion energy.²⁷ This failure is addressed by modern dispersion corrected DFT (DFT-D) functionals, which rectify the incorrect long-range asymptotic decay behaviour of local hybrid functionals.^{27,}

28

An extension of DFT, Time Dependent Density Functional Theory (TDDFT) can be used to quantify the excited state properties of biological systems. Properties including excitation energies and UV/vis spectra can be calculated using this method. TDDFT

differs from DFT due to the application a time dependent potential (e.g. a magnetic field).²⁹ To gain information regarding the previously mentioned properties, the effect of this potential on the system must be analysed. As an example, Rogers et al. used the B3LYP/6-311++G(d) level of theory to investigate the excited state transitions occurring within tryptophan and approximate the vertical excitation energies of the chromophore.³⁰

1.4 Platinum Based Complexes as Anticancer Agents

Since the serendipitous discovery of their antineoplastic properties in 1965, platinum based complexes such as Cisplatin have become one of the most widely used drugs within chemotherapy.³¹ It has been found that these compounds instigate cell death by crosslinking to cellular DNA nucleotides.³² While there is consensus that platinum based drugs occupy a crucial role in the treatment of advanced cancers, there is also acknowledgement of their shortcomings, which include acquired drug resistance by cells and severe side effects such as neurotoxicity and nephrotoxicity.^{33,34} These issues coupled with the desire to increase the efficacy, have fuelled interest in the use of platinum based complexes in conjunction with Photodynamic therapy (PDT).³⁵

PDT has a wide range of clinical applications and is used in the treatment of cancers such as that of the lung and skin, and for some acute non-malignant conditions such as acne.³⁶ In its most common form, its use requires a photosensitising agent (a drug which makes cells sensitive to light) and a light source of a specific wavelength. Upon irradiation, the photosensitiser undergoes photoexcitation and a series of other photophysical processes,

which culminates in the production of the highly reactive and cytotoxic singlet oxygen species ($^1\text{O}_2$).

Following the absorption of a photon of energy, the photosensitiser is promoted from its groundstate (^1GS) to a singlet excited state (^1ES). The ^1ES is relatively short-lived as intersystem crossing occurs soon after, generating the photosensitiser triplet excited state (^3ES). Provided that the ^3ES is long-lived, it can participate in an energy transfer process with adjacent oxygen molecules, generating $^1\text{O}_2$ from molecular oxygen in its triplet groundstate ($^3\text{O}_2$).³⁷

Latest research has focused on the use of transition metals in Photoactivated Chemotherapy (PACT), where photoexcitation is used to control the transition metal reactivity.³⁸ Recent studies such as that by Sadler et al. have explored the photochemistry of platinum (II) and (IV) complexes in an attempt to gain insight into the effectiveness of these complexes as metallophotosensitisers.³⁹ In addition, a number of recent studies have involved photoexcitation of intercalated transition metal complexes.⁴⁰

As a first step toward providing a fundamental, molecular level understanding of transition metal complex-DNA photocleavage mechanisms, Sen et al. have recently performed the first laser photodissociation studies on platinum complexes bound to individual nucleobases. Initial work involved obtaining the photodepletion (absorption) spectra of $\text{Pt}(\text{CN})_4^{2-} \cdot \text{uracil}$ and $\text{Pt}(\text{CN})_6^{2-} \cdot \text{uracil}$ complexes. Upon consideration of the two observed in the UV spectral range, a preliminary assignment of the excited-state transitions observed were attributed to $\pi \rightarrow \pi^*$ nucleobase-centred transitions.⁴¹

This work built on earlier research carried out by the group in which the collision induced dissociation of $\text{Pt}(\text{CN})_4^{2-}$ and $\text{Pt}(\text{CN})_6^{2-}$ complexes bound to various nucleobases had been studied. Using a combination of theoretical and experimental methods, pathways for ground state collision induced dissociation were suggested, and the geometric structures and isomers of these complexes were identified. Whereas, the $\text{Pt}(\text{CN})_6^{2-} \cdot$ nucleobase clusters were shown to fragment by solvent evaporation, the $\text{Pt}(\text{CN})_4^{2-}$ clusters fragmented by a combination of solvent evaporation and proton transfer between the nucleobase and dianion.⁴²

Other work by Sen et al. has characterized in detail the relationship between the nucleobase and the photophysics of the platinum complexes. Photodepletion and photofragmentation spectra for $\text{Pt}(\text{CN})_4^{2-} \cdot \text{Nu}$ complexes have been obtained (Nu = adenine, cytosine, thymine or uracil) to explore the influence of changing the nucleobase. The photodepletion spectra displayed a broad absorption band of varying widths at ca. 4.70 eV for all systems. The variation in band width was found to correlate with a changes in the photofragmentation product ions produced after photoexcitation.⁴³

Aside from platinum, many other transition metals exhibit anti-cancer activity. These include ruthenium, osmium and gold.⁴⁴ In particular, osmium (II) and ruthenium (II) polypyridyl complexes are often researched as they absorb richly in the visible region and display comparatively long metal to ligand charge transfer (MLCT) states, making them ideal candidates for PDT. Earlier experimental studies by Meyer et al. have probed the decay kinetics of these MLCT states for osmium and ruthenium complexes.⁴⁵ Menéndez

et al. have conducted theoretical work in this area. TDDFT was used to examine the excited states transitions occurring within ruthenium polypyridyl, and found that the M05 functional found to be the best performed best at predicting the UV absorption spectrum.⁴⁶ Zheng et al. have previously employed both PES spectroscopic methods and DFT level calculations to investigate the ground state properties of nucleobase-gold complexes.⁴⁷

1.5 Overview of Thesis

The main aim of this project is to investigate the nature of the excited state transitions occurring within nucleobase-Pt systems using computational methods such as TDDFT. In particular, this work is aimed at providing a more detailed assignment of the previously measured, UV photodepletion (absorption) spectra of $\text{Pt}(\text{CN})_6^{2-}\cdot\text{uracil}$ and $\text{Pt}(\text{CN})_4^{2-}\cdot\text{uracil}$.^{41,44} In addition, the project will investigate the applicability of TDDFT for the interpretation and prediction of the electronic excited states of these complex systems.

Chapter 2 presents the computational methods and models that are used throughout this thesis. Chapter 3 describes the results of a study exploring the excited state transitions occurring within $\text{I}^-\cdot\text{Nucleobase}$ complexes to focus on nucleobase localised excitations. Chapter 4 presents work on the electronic transitions of $\text{Pt}(\text{CN})_4^{2-}\cdot\text{H}_2\text{O}$ to focus on $\text{Pt}(\text{CN})_4^{2-}$ centred excitations. Chapter 5 describes the study of the excited-state transitions of $\text{Pt}(\text{CN})_4^{2-}\cdot\text{nucleobase}$ and $\text{Pt}(\text{CN})_6^{2-}\cdot\text{nucleobase}$ systems, where both the dianion and nucleobase have active chromophores.

Chapter 2

Computational Methods

2.1 Density Functional Theory

The fundamental aim of Density Functional Theory (DFT) and other quantum mechanical calculations is to provide a solution to the Schrödinger equation,

$$\hat{H}\Psi = E\Psi \quad (2.01)$$

where \hat{H} is the Hamiltonian operator, E is the energy of the system and Ψ is the wavefunction.²⁵ In quantum mechanical systems, \hat{H} defines the total energy as the sum of its kinetic and potential energies. For systems containing more than one particle, i.e many body, \hat{H} must also take into account the interaction energy between the electrons. Thus, the Hamiltonian operator can further be defined as:

$$\hat{H} = \hat{T} + \hat{V} + \hat{W} \quad (2.02)$$

where \hat{T} is the kinetic energy operator, \hat{V} is the potential energy operator and \hat{W} is the electron-electron interaction operator.⁴⁸ For one electron atoms, the Schrödinger equation can be solved exactly. However, obtaining a solution to the Schrödinger equation is complicated for many body systems due to electron correlation and the number of variables which determine the wavefunction.⁴⁹ The wavefunction is dependent on $3N$ variables (N being the number of electrons) and therefore becomes too complex to solve analytically. To calculate a solution for many electron systems, approximations must be made.

One such approximation was proposed by Born and Oppenheimer.⁵⁰ The Born-Oppenheimer approximation simplifies the Schrödinger equation by separating the nuclear and electronic

terms. The basis for this division arises from the difference in mass of the nuclei and electrons. Although they both apply the same momentum, nuclei have a considerably larger mass than electrons. Therefore, nuclei have such a small velocity that their position can be considered fixed. This allows the motion of the nuclei to be disregarded and the wavefunction of the molecule to be expressed as a product of electronic and nuclear wavefunctions.²⁵

DFT provides an alternative method for solving the Schrödinger equation. In contrast to wavefunction based methods, the determining factor in DFT is electron density. From this the energy of the system and its ground state properties can be ascertained. DFT greatly simplifies the Schrödinger equation as the number of variables in the determining factor is reduced from $3N$ to 3.⁴⁹ In contrast to wavefunction based methods, the independence of electron density's spatial coordinates from N renders DFT suitable for larger many-body systems.

The origins of DFT lie in the Thomas-Fermi (TF) model which relates the electron density $\rho(\mathbf{r})$ to the kinetic energy to the system $T_{[\rho]}$.⁵¹ This relationship is given in equation 2.03 below.

$$T_{[\rho]} = C_F \int \rho^{5/3}(\mathbf{r}) d\mathbf{r} \quad (2.03)$$

Where:

$$C_F = \frac{3}{10} (3\pi^2)^{2/3} = 2.8712 \quad (2.04)$$

As shown in equation 2.05, the total energy of a system can be expressed as the sum of its kinetic energy, the electron-electron interaction V_{ee} and external potential interaction V_{ext} .^{25,52} This can also be written as:

$$E[\rho] = T[\rho] + V_{ext}[\rho] + V_{ee}[\rho] \quad (2.05)$$

The external potential and electron-electron interaction terms can be further defined as follows:

$$V_{ext}[\rho] = \int V_{ext} \rho(\mathbf{r}) d\mathbf{r} \quad (2.06)$$

$$V_{ee}[\rho] = \frac{1}{2} \iint \frac{\rho(\mathbf{r}_1)\rho(\mathbf{r}_2)}{|\mathbf{r}_1 - \mathbf{r}_2|} d\mathbf{r}_1 d\mathbf{r}_2 \quad (2.07)$$

The substitution of equations 2.06 and 2.07 into equation 2.05 produces the TF energy functional:⁵³

$$E_{TF}[n] = C_F \int \rho^{5/3}(\mathbf{r}) d\mathbf{r} + \frac{1}{2} \iint \frac{\rho(\mathbf{r}_1)\rho(\mathbf{r}_2)}{|\mathbf{r}_1 - \mathbf{r}_2|} d\mathbf{r}_1 d\mathbf{r}_2 + \int V_{ext} \rho(\mathbf{r}) d\mathbf{r} \quad (2.08)$$

The main error in the TF model originates from the kinetic energy. The model produces an inaccurate kinetic energy value because it treats the electrons as non-interacting particles and therefore does not include an electron correlation or exchange term. The TF model was later revised by Dirac who added the following expression to account for the exchange energy of electrons:⁵³

$$-\frac{1}{4\pi^3} (3\pi^2)^{4/3} \int \rho^{4/3}(\mathbf{r}) d\mathbf{r} \quad (2.09)$$

In spite of this amendment, the kinetic energy was still inaccurate because the energy functional contained a large error in the exchange term and still ignored the correlation energy. Crucially, the TF and Thomas-Fermi-Dirac (TFD) models could not be used as a practical electronic structure method as they produced a poor description of molecular bonding. The energies produced by the functionals were unexpectedly higher than their atomic parts.

The TF and TFD models were used as a basis for the Hohenburg-Kohn (HK) theorems.⁵⁴ The work by Hohenburg and Kohn provided further proof of the relationship between electron

density and the ground-state properties of a system. The first HK theorem uses a *reductio ad absurdum argument* to prove that the ground state electron density determines the external potential.²⁵ It states that for two systems of interacting electrons moving in two external potentials v_1 and v_2 , v_1 and v_2 cannot differ by more than a constant if both systems have the same electron density.⁴⁹ The first HK theorem is fundamental to DFT as it demonstrates that the electron density $n(\mathbf{r})$ can be used to solve the Schrödinger equation. Electron density determines the number of electrons in the system and the external potential, from which the Hamiltonian can be calculated.

The second HK theorem introduces a universal density functional F_n from which the minimal value of the energy functional, $E_v[n]$, i.e the exact energy of the groundstate can be obtained.⁵² The density functional is defined as:

$$F_n = \min_{\Psi \rightarrow n} \langle \Psi | T + V_{ee} | \Psi \rangle \quad (2.10)$$

For a system containing N electrons in an external potential, v , the minimum values of F_n and $E_v[n]$ can be obtained from equation 2.11 when the value of $n(\mathbf{r})$ is correct.⁵⁴

$$E_v[n] = \int v(\mathbf{r}) n(\mathbf{r}) d\mathbf{r} + F[n] \quad (2.11)$$

The framework of modern DFT can be found in the Kohn-Sham theory which uses a set of differential equations to address the fundamental problems of the TF and TFD models.⁵⁵

Kohn and Sham devised a fictitious system of non-interacting electrons in an external potential (referred to as the effective potential v_{eff}). The electron density was described using Kohn-Sham orbitals ϕ_i , and was made equivalent to the density of a real system of interacting electrons.⁵² Using a fictitious non-interacting system of electrons allows the orbitals to be expressed as Slater determinants.⁴⁸

The Kohn-Sham energy functional is of the form:⁵⁶

$$E[n] = \int v(\mathbf{r}) n(\mathbf{r}) d\mathbf{r} + \frac{1}{2} \iint \frac{n(\mathbf{r}_1)n(\mathbf{r}_2)}{|\mathbf{r}_1 - \mathbf{r}_2|} d\mathbf{r}_1 d\mathbf{r}_2 + T_s[n] + E_{xc}[n] \quad (2.12)$$

From which the exact value of the unknown kinetic energy operator, $T_s[n]$ can be calculated as:⁵²

$$T_s[n(\mathbf{r})] = -\frac{1}{2} \sum_{i=1}^N \int \phi_i^*(\mathbf{r}) \nabla^2 \phi_i(\mathbf{r}) d\mathbf{r} \quad (2.13)$$

The exchange correlation energy E_{xc} in equation 2.12, is a correction term which describes the error in electron-electron repulsion and the kinetic energy. The difference in electron-electron repulsion arises from its classical treatment in the Kohn-Sham theory. The error in kinetic energy results from the variation between the fictitious Kohn-Sham system and the interacting system.²⁵ The solution to equation 2.12 provides a value which is extremely close to the kinetic energy of the real interacting system. However, it does not offer an exact value for the exchange-correlation operator, therefore E_{xc} must be approximated.

2.2 Density Functionals

There are numerous classes of functionals which have been developed to approximate the exchange-correlation energy. The simplest of these are local density approximation (LDA) functionals in which the electron density is treated as a uniform electron gas and its value at a specific point \mathbf{r} is known. Generalised Gradient Approximation (GGA) functionals improved LDAs by adding a gradient correction term to account for the inhomogeneity of a real system.^{52,55}

The exchange energy is far greater than the correlation energy and so must be accurately defined. This difference is recognised in Hybrid GGA functionals which incorporate a Hartree Fock (exact) term. Hybrid GGA functionals combine a fraction of exact exchange

with GGA exchange and correlation terms.⁵⁷ Two popular hybrid functionals are B3LYP and PBE0.^{58,59} B3LYP is a combination of the Becke's three parameter (B3) exchange functional and the Lee-Yang-Parr (LYP) GGA correlation functional.^{55,60} B3LYP contains 20% exact exchange. PBE0 contains 25% Hartree-Fock exchange, with 75% Perdew, Burke and Ernzerhof (PBE) exchange, and uses the full PBE correlation functional.

A long-range corrected version of B3LYP, CAM-B3LYP was developed to rectify the incorrect long-range behaviour of the B3LYP exchange potential.⁶¹ This inaccuracy was thought to be the reason behind a number of B3LYP's failures including the calculation of excited states using TDDFT and charge-transfer excitations.^{61,62} CAM-B3LYP uses the Coulomb-attenuating method to range separate the total exchange functional in B3LYP. CAM-B3LYP treats short-range exchange interactions with mostly DFT exchange and long-range interactions largely with exact exchange integrals. The Coulomb operator is partitioned using the following formula:

$$\frac{1}{r_{12}} = \frac{1 - (\alpha + \beta \cdot \text{erf}(\mu r_{12}))}{r_{12}} + \frac{\alpha + \beta \cdot \text{erf}(\mu r_{12})}{r_{12}} \quad (2.14)$$

Where erf is the standard error function, μ is the range separated parameter and $\alpha + \beta$ determine the value of exact exchange at $r_{12} = 0$ and $r_{12} = \infty$. In CAM-B3LYP $\alpha = 0.19$ and $\beta = 0.46$.^{61,63}

Jensen and Govind used CAM-B3LYP to investigate the lowest vertical excitation energy transitions of several individual nucleobases and base pairs.⁶⁴ In addition to CAM-B3LYP, the study compared the performance of the long-range corrected BNL and LC-PBE0 functionals. Jensen and Govind found that CAM-B3LYP performed comparatively well, successfully describing the charge transfer nature of the HOMO \rightarrow LUMO transition in the adenine-thymine base pair.

The newer generation meta-GGA functionals are dependent on the kinetic energy density and/or the second derivative of electron density.⁵⁵ The Truhlar group have created a certain range of hybrid meta-GGA functionals which incorporate a percentage of exact exchange.⁶⁵ These include the M06 and M11 families of functionals. The M06 and M06-2X functionals contain 27% and 54% HF exchange respectively.⁶⁵ M11 is a range-separated hybrid meta-GGA functional with the following amounts of HF exchange: 42.8% HF in the short range and 100% in the long range.⁶⁶ In a TDDFT study, Aquino et al. used M06-2X and M06-HF to characterise the excited-state transitions of adenine-thymine and cytosine-guanine base pairs.⁶⁷ The group also investigated the effect of solvation on the charge transfer states at the M06-2X/TZVP level of theory.

Other Minnesota functionals include the meta-nonseparable gradient approximation (meta-NGA) MN12 family. In contrast to GGAs, NGAs do not treat the exchange and correlation terms separately.⁶⁸ Akin to meta-GGAs, meta-NGAs can depend on the electron and/or kinetic energy densities. MN12-SX is a hybrid meta-NGA functional that is range separated.⁶⁹ MN12-SX has 25% exact exchange in the short range and no long-range exact exchange component. Due to the absence of HF exchange in the long range, MN12-SX is described as a hybrid screened exchange (SX) functional.

2.3 Time-Dependent Density Functional Theory

Time-dependent density functional theory (TDDFT) is an extension of DFT which can be used to study the excited-state properties of a system.⁷⁰ The basis of TDDFT lies in a theorem that is analogous to the time-independent Hohenberg-Kohn theorem. The Runge-Gross theorem demonstrated the relationship between the time-dependent external potential $v_{\text{ext}}(\mathbf{r},t)$ and the electron density of the system $n(\mathbf{r},t)$. Runge and Gross showed that when two external potentials $v_{\text{ext}}(\mathbf{r},t)$ and $v_{\text{ext}}'(\mathbf{r},t)$ have a difference of more than a time-dependent function,

their respective electron densities $n(\mathbf{r},t)$ and $n'(\mathbf{r},t)$ also differ. This led Runge and Gross to conclude that for a many-body system, evolving from a fixed initial wavefunction, there is a one-to-one mapping between $v_{\text{ext}}(\mathbf{r},t)$ and $n(\mathbf{r},t)$.⁷¹ The relationship between $v_{\text{ext}}(\mathbf{r},t)$ and $n(\mathbf{r},t)$ is significant because the Hamiltonian (and consequently the solution to the Schrödinger equation) can be calculated from the external potential.⁷² Therefore, the energy and other properties of the system can be expressed as a function of the time-dependent electron density.⁴⁸

Similarly to DFT, the time-dependent Hamiltonian can be partitioned into its constituent operators: the kinetic and time dependent potential operators T and $\hat{V}(t)$, respectively. Time-dependent Kohn-Sham equations were constructed to calculate the system's kinetic energy and electron density accurately.⁷² In this theorem, the non-interacting electrons once again reside in Kohn-Sham orbitals φ_i and the fictitious Kohn-Sham system is given electron density equivalent to that of a “real” system of interacting electrons. The electron density of the real system is:

$$n(\mathbf{r},t) = \sum_i^{\text{occ}} |\varphi_i(\mathbf{r},t)|^2 \quad (2.15)$$

The electrons in the fictitious time-dependent system move in an external Kohn-Sham potential, v_{KS} . As displayed in equation 2.16, the Kohn-Sham potential is the sum of the external, the electrostatic Hartree and exchange potentials.

$$v_{KS}(\mathbf{r},t) = v_{\text{ext}}(\mathbf{r},t) + v_{\text{HARTREE}}(\mathbf{r},t) + v_{xc}(\mathbf{r},t) \quad (2.16)$$

Equations 2.17 and 2.18 further define the Hartree and exchange potentials, v_{HARTREE} and v_{xc} , respectively.

$$v_{HARTREE}(\mathbf{r}, t) = \int d^3r' \frac{n(\mathbf{r}, t)}{|\mathbf{r} - \mathbf{r}'|} \quad (2.17)$$

$$v_{xc}(\mathbf{r}, t) = \left. \frac{\delta \tilde{A}_{xc}}{\delta n(\mathbf{r}, \tau)} \right|_{n(\mathbf{r}, t)} \quad (2.18)$$

v_{xc} is defined using the exchange correlation component of the action potential \tilde{A}_{xc} and the pseudo time τ . Analogously to the time-independent Kohn-Sham equations, functionals must be used to approximate v_{xc} because its value is unknown.

There are many studies which have successfully used TDDFT to investigate the optical properties of nucleobases and transition metal complexes. Tai et al. have studied the absorption properties of diazido platinum (IV) complexes using TDDFT.⁷³ The computational and experimental excitation energies were found to be in good agreement with errors under 0.3 eV.⁷⁰

Varsano et al. and Tsolakidis et al. employed TDDFT to investigate the vertical excitations of individual DNA nucleobases and their base pairs.⁷⁴ Both studies offer a comparison between the calculated excitation energies, experimental results and excitation energies obtained using other methods such as CASSCF and CASPT2. The theoretical values produced by TDDFT were generally in good agreement with the experimental values and results obtained using the more computationally demanding methods.

2.4 Basis Sets

Both ab initio and DFT methods employ basis sets to mathematically describe the molecular orbitals in a system. A basis set is composed of a series of functions known as basis functions. Basis functions are one electron functions which approximate the atomic orbitals in a system. Due to the various generalisations made during their calculation, basis functions cannot be viewed as exact representations of atomic orbitals.⁷⁵

Basis functions can be arranged in a linear combination to give rise to a wavefunction. Since electron density can itself be expressed as a wavefunction, the molecular orbitals of a system can be determined.²⁵

Atomic orbitals are represented by two main types of basis functions: Slater-Type Orbitals (STOs) and Gaussian-Type Orbitals (GTOs). STOs bear strong resemblance to the atomic orbitals of hydrogen and are of the form:

$$\Psi = Ar^{n-1} e^{-\zeta r} Y_{l,m}(\theta, \phi) \quad (2.19)$$

Where A is the normalisation constant, n , l and m are quantum numbers, ζ is the orbital exponent and $Y_{l,m}(\theta, \phi)$ are the spherical harmonics.

In comparison to GTOs, STOs are considered a more accurate representation of atomic orbitals due to their correct short and long range behaviour. STOs satisfy the nuclear cusp condition in the short range and display exponential decay in the long range. This accounts for the maximum in electron density reached at the nucleus and the exponential decrease in electron density at increasingly large distances away from the nucleus. Long range decay is controlled by the orbital exponential factor which is denoted in Equation 2.19 as ζ .⁷⁵

The major disadvantage of STOs is the lengthy computational time that they are associated with. This originates from the computational demanding calculations of various molecular integrals. This numerical difficulty is such that STOs are only rendered suitable for atoms and a small range of molecules.^{25,75}

Boys put forward a simpler method for the evaluation of the molecular integrals using GTOs. The general form of a Cartesian GTO is:

$$\Psi_{ijk} = Ax^i y^j z^k e^{-\zeta r^2} \quad (2.20)$$

where i, j and k are positive Cartesian integers. Each GTO is usually expressed as a linear combination of Cartesian Gaussians (also known as Gaussian primitives).⁷⁵ This produces a contracted basis set with the form:

$$\chi_i(\mathbf{r}) = \sum_{j=1}^N d_j g_j(\mathbf{r}) \quad (2.21)$$

Where N is the length of contraction, d_j is the contraction coefficient and g_j is a normalised Gaussian primitive.⁷⁶

Gaussian functions do not exhibit the same short and long-range behaviour as STOs and therefore are not as accurate. They tend to show a rapid decrease in electron density at large distances away from the nucleus and do not replicate the nuclear cusp.^{75,76}

A basis set which uses only one basis function to represent each atomic orbital is known as a minimal basis set. Calculations employing minimal basis set are very low in computational demand, making their use very attractive. However, minimal basis sets are only capable of describing the most basic features of an orbital and therefore produce results of relatively low accuracy.⁷⁵

An enhanced description of atomic orbitals can be gained by increasing the amount and size of the basis functions. Double and triple zeta basis sets employ two and three basis functions, respectively, for each orbital. Each set of functions can be differently sized to account for the variation in charge distribution throughout a molecule.²² The size of an orbital is controlled by the orbital exponential, ζ . As the value of ζ decreases, the width of the orbital increases and becomes more diffuse.^{75,22}

Increasing the number of basis functions can be problematic as it often results in an increase in computational time. Split-valance basis sets try to counter this increase by making an important distinction between the core and valence electrons. It is primarily valence electrons

that are involved in chemical bonding, core electrons remain largely unperturbed by it. Therefore there are no significant benefits that can be achieved by increasing the number of functions for the core electrons.⁷⁵ To reflect this observation, split basis sets use a one basis function to describe the core atomic orbitals, while the valence orbitals are represented by multiple functions. The reduction in the overall size of the basis set yields a decrease in computational time.^{25,75}

A popular family of split-valence basis sets are those produced by Pople et al., denoted as N-M1G or N-M11G. N and M are the basis functions representing the core and valence orbitals respectively. N and M are integers which denote the number of Gaussian primitives used in each function.⁷⁵ The 6-311G basis set is commonly used in calculations involving nucleobases. Ren et al. used the PBE0/6-311++G(2d,2p) level of theory when investigating the spectral shifts in the UV spectra of solvated uracil.⁷⁷ Improta and Barone also employed PBE0/6-311++G(2d,2p) to calculate the gas- and solution-phase absorption spectra of uracil.⁷⁸

Another frequently used family of basis sets are those by Ahlrichs et al. Def2 basis sets use either single, double, triple or quadruple zeta basis sets to describe the valence orbitals.⁷⁹ They are suitable for light atoms and first-row transition metals but can also be employed as an effective core potential (ECP) for heavier atoms. Wu et al. used Def2-TZVP (ECP) in conjunction with 6-31G(d) in a recent investigation of the photophysical properties of various phosphorescent Pt(II) complexes.⁸⁰ DFT calculations were performed at the following levels of theory to test the reliability of the results: TPSS/TPSS, TPSSh, B3LYP and PBE0.⁸¹ During the DFT geometry optimisation of Pt(CN)₄²⁻, Dohn et al. assessed the performance of various Ahlrichs basis sets including Def2-TZVP and Def2-QZVP.⁸² Optimisations were performed at BLYP, B3LYP, PBE and PBE0 levels of theory.^{60,83}

The accuracy of a basis set can be further improved by addition of polarisation and diffuse functions. When AOs participate in bonding, their shape can become slightly asymmetric as electron density becomes polarised in the direction of the bond. Polarisation functions reproduce this asymmetry by adding a function which possesses a higher angular momentum than the valence AOs. This introduces angular flexibility into the basis set and allows for increased accuracy in the description of electron density in bonded areas.²⁵

Diffuse functions are usually added to a basis set to describe areas with expansive electron density. They have very small exponents and exhibit slow decay in the long range. Diffuse functions are necessary to accurately represent the electron distribution in anions, highly electronegative atoms and long, weak bonds.^{25,75}

The plus sign (+) is used in Pople-type basis sets to denote the presence of a polarisation function. + specifies that diffuse functions have been added to heavy atoms, while ++ indicates that diffuse functions have also been added to light atoms.⁷⁵ Although their inclusion can increase the computational cost, a basis set is only regarded as balanced if it contains both diffusion and polarisation functions.²²

The significance of adding polarisation and diffuse functions is outlined in a study on nucleic bases by Shukla and Leszczynski. A range of 6-311G basis sets with varying degrees of polarization and diffusion were used in conjunction with TD-B3LYP to calculate the excitation energies of different nucleobases. Shukla and Leszczynski found that the use of larger, more diffuse basis sets [e.g. 6-311(5+,5+)G(df,pd), in which the fourth and fifth sets of diffusion functions are used on all atoms] increased the accuracy of the results.⁸⁴

Studying systems which contain heavy elements can be challenging because of the lengthy computational times involved with calculations. Effective core potentials (ECP) reduce the CPU time cost of these systems by substituting the core electrons for a pseudopotential. The

pseudopotential is an effective potential constructed from the product of the polynomial radial functions and spherical harmonics. It gives rise to a pseudo wavefunction that does not contain any nodes. Additionally, ECPs can be formulated to describe scalar and spin-orbit relativistic effects, both of which can be prominent in heavy elements.²²

LANL2DZ is a double-zeta basis set that is frequently used in the study of transition metals.²⁵

LANL2DZ is composed of the Los Alamos pseudopotential and double zeta valance basis set. During their recent TDDFT investigation on Pt (II) complexes with picolinate ligands, Zhang et al. employed LANL2DZ as an ECP for Pt and 6-31G* for the light atoms.⁸⁵

Geometry optimisations and excited-state calculations were performed using the B3LYP functional. Ghani and Mansour performed DFT geometry optimisations of palladium (II) and platinum (II) complexes with benzimidazole ligands at B3LYP level of theory using LANL2DZ and 6-31G*.⁸⁶

2.5 Solvation Models

Quantum chemistry packages typically represent molecules as isolated, non-interacting species in the gas phase. Whilst this creates a simplistic environment in which calculations can be performed, the effect of the chemical surroundings on the system are neglected. For biologically relevant molecules these effects can be significant as almost all biological processes occur in solution.²⁵

The effects of solvation on the electronic states of various nucleobases have been investigated extensively using a range of theoretical methods.⁸⁷ Such effects are exemplified in theoretical studies by DeFusco et al. and Ren et al., in which the positions of the two lowest energy bands in the UV absorption spectrum of uracil were shown to be altered by solvation. Both studies found that the lowest energy spectral band of uracil was shifted to a shorter wavelength when the absorption spectrum was calculated in solution. Conversely, a

significant shift in the position of the second lowest energy spectral band to a longer wavelength was observed in the computed aqueous absorption spectra of uracil.^{77,87} Solvent shifts in spectral absorption band positions to either longer or shorter wavelengths are referred to as bathochromic or hypsochromic shifts, respectively.

In addition to solvent induced shifts in the position of spectral absorption bands, solvation can also alter the intensity of the bands. An increase in the absorption intensity of a spectral band is referred to as a hyperchromic shift, while a decrease in the absorption intensity is known as a hypochromic shift.⁸⁸

Over recent years, a substantial amount of research has been devoted to developing models to study solvation effects. These methods can be divided into two main types: explicit and implicit models. In explicit solvation models, the solute is surrounded by a number of discrete solvent molecules.⁸⁹ Although this method provides a very detailed and accurate description of solute-solvent interactions, it is also very computationally expensive due to the increased system size. A substantial proportion of the computational demand originates from the calculation of statistical mechanical averages. As the system contains a large number of molecules, statistical averages are required to ascertain its equilibrium properties. The size of the system is such that the use of explicit solvation models is generally restricted to Monte Carlo and Molecular Dynamics simulations.⁹⁰

Implicit models reduce the computational cost required by substituting the individual solvent molecules for a continuous medium. In implicit continuum models, the solvent media surrounds a cavity in which the system is located.⁹⁰ The shape of the cavity is close to that of the system under study but its precise dimensions are dependent on the particular continuum model used. Few parameters are used to define the continuum. It is usually characterised by properties such as the dielectric constant or surface tension and has values in line with the

ideal solvent.⁹¹ Implicit models provide an averaged representation of solute-solvent interactions and therefore are not suitable in studies where the explicit behaviour of the solvent is important.²⁵

A commonly used implicit method is the Polarizable Continuum Model (PCM). Here, the cavity is composed of overlapping spheres with radii that are scaled to that of a van der Waals atom. As each sphere is atom centred, the overall shape of the cavity is defined by the solute. There are regions of the cavity that solvent cannot interact with, therefore an area known as the solvent accessible surface (SAS) is outlined around the cavity.⁹²

The continuum and its degree of polarisation is solely defined by the dielectric constant. Polarisation of the solvent occurs in a self-consistent fashion. The charge density of the solute induces the polarisation of the dielectric continuum. This in turn causes the solute to become polarised and the formation of a reaction field.⁹² As the reaction field is present as a charge spread across the cavity surface, it can be calculated using point charges. The SAS is divided into small fragments known as tesserae and the point charge at each fragment is then determined.⁹¹

Models from the PCM family are frequently used in conjunction with TDDFT to incorporate solvent effects into excited-states studies. Han et al. employed a variant of PCM, IEFPCM to study the photophysical properties of various heterocyclic carbene platinum (II) complexes.⁹³ Calculations using IEFPCM/TD-B3LYP produced absorption and emission spectra, from which the excited state transitions could be characterised. Gustavsson et al. conducted experimental and theoretical investigations of numerous uracil derivatives, in which PCM/TD-PBE0 was employed to calculate absorption and emission spectra.⁹⁴

2.6 Computational Details

TDDFT was used to study the excited-state transitions of the following complexes and their constituent monomer parts: $I \cdot Nu$, $Pt(CN)_4^{2-} \cdot H_2O$, $Pt(CN)_4^{2-} \cdot Nu$ and $Pt(CN)_6^{2-} \cdot Nu$. Aside from TDDFT, there a wide range of methods which can be used to study the excited states. These include wavefunction-based methods such as CIS, CC2 and CASSCF. However, the size limitations of these methods renders them unsuitable for the systems under consideration. All calculations were performed using the d01 version of the Gaussian 09 (G09) package.⁹⁵

In addition to assigning the excited state transitions of the named systems, the performance of a range of density functionals and basis sets will be assessed. For every system studied, the following functionals were tested: B3LYP, CAM-B3LYP, M062X, M11, MN12-SX and PBE0.^{58-61, 65-66}

When investigating the excited states of uracil and cytosine, the performance of the LANL2DZ, 6-311++G(2d,2p) and def2-TZVPP basis sets were evaluated. Calculations on $Pt(CN)_4^{2-} \cdot uracil$ and $Pt(CN)_4^{2-}$ tested the following range of pseudopotentials: LANL2DZ, def2-TZVPP and SDD. ECPs were used on platinum, while either 6-311++G(2d,2p) or LANL2DZ was used on the C, N, H and O atoms .

The computational results were compared to either experimental UV-Vis or photodepletion (absorption) spectra. Gas-phase photodepletion spectra was not available for the isolated nucleobase monomers studied, therefore these results were compared to the condensed phase UV-vis spectra.

To permit a direct comparison between the computational and experimental UV-vis spectra, solvation modelling was incorporated into the excited state calculations of the nucleobase and $Pt(CN)_4^{2-}$ monomers. The method used to model solvation was the default version of PCM in

G09, Integral Equation Formalism PCM (IEFPCM). IEFPCM is a reformulation of PCM, which aims to enhance the performance by including gradient and molecular response calculations in its formalism.^{25,96}

Chapter 3

A TDDFT Computational Study of Iodide Ion-Nucleobase Complexes

3.1 Introduction

UV spectra of gas-phase platinum cyanide complexes bound to a single nucleobase have previously been acquired by Sen et al. using laser spectroscopy. The $\text{Pt}(\text{CN})_n^{2-}\cdot\text{Nu}$ complexes act as model systems in the examination of the photochemical processes associated with PDT.⁴³ These studies have produced UV spectra with unique absorption bands for each complex, however only initial assignments of these bands have been made. Therefore, there is now a need to confirm these assignments using computational chemistry. The complexity of studying these systems theoretically are such that the much simpler, iodide-nucleobase ($\text{I}\cdot\text{Nu}$) clusters will be investigated first.

Gas-phase iodide ion-nucleobase clusters have been studied previously, both experimentally and theoretically. King et al. have used iodide-nucleobase clusters as model systems for studying the mechanisms by which low-energy electrons interact with nucleobases, causing DNA double strand breakage.⁹⁷ Their investigations used time-resolved photoelectron spectroscopy to explore the dynamics and kinetics of near-threshold iodide-thymine and iodide-uracil clusters.⁹⁸

King et al. have very recently reported computational data as part of their latest study. Time-Dependent Density Functional Theory (TDDFT) calculations were performed at the ωB97XD level to determine the equilibrium geometries of various iodide-nucleobase binary clusters in

their electronically excited states. Additionally, the differences in electron density of the optimised iodide-thymine and iodide-uracil geometries at the ground and first excited states were investigated.^{99,100} Mak et al. have used both quantum chemical and molecular dynamics calculations to conduct theoretical studies of photoexcited iodide-methanol clusters. The properties of the ground, excited and ionised states of these clusters were explored at MP2, CCSD(T) and CASSCF levels of theory respectively. *Ab initio* molecular dynamics simulations were employed to elucidate the detailed nature of dynamical relaxation pathways of the clusters.¹⁰¹

The aim of this chapter will be to use TDDFT to calculate electronic spectra for I·Nu complexes (Nu = adenine, thymine or uracil) and their constituent “monomer” parts, (i.e. the isolated I ion and isolate nucleobase). The variation in excitation energies resulting from the use of different functionals and basis sets will also be assessed.

3.2 Computational Methods

Excited state, geometry optimisation and frequency calculations were performed using the Gaussian 09 (G09) programme package, version d01.⁹⁵ The ground-state geometries of I·Nu complexes were optimised using Density Functional Theory (DFT) at the following levels of theory in conjunction with the LANL2DZ basis set: B3LYP, CAM-B3LYP, M062X, M11, MN12-SX and PBE0.^{58-61, 64-65} For studies involving cytosine and uracil, the basis set used was also varied between LANL2DZ, 6-311++G(2d,2p) and Def2-TZVPP.¹⁰² Mean Absolute Errors (MAEs) were then calculated for each density functional/basis set combination. Frequency calculations were performed to ensure that the optimised ground-state geometric structures calculated represent true minima on the potential energy surfaces.

The experimental spectra that are used to benchmark the calculations presented in this work were measured from clusters generated using electrospray ionisation. This preparation method is known to predominantly produce the nucleobase in its native tautomeric form.¹⁰³

Therefore, only the native tautomers are studied here.

To study the excited states, TDDFT calculations were then performed on the optimised ground-state structures at the various levels of theory listed above. Formatted checkpoint files were generated for each system using B3LYP/LANL2DZ in order to view the molecular orbitals (MOs).

The effect of solvation on the excitation energies of the nucleobases was also investigated using the default version of PCM in G09, IEFPCM. IEFPCM/TDDFT calculations were performed at the B3LYP/LANL2DZ for uracil, cytosine, thymine and adenine. IEFPCM calculations involving uracil, cytosine and thymine were performed using water as the solvent. The solvent used in the aqueous excited-state calculation on adenine was methanol.

The solvents used in the IEFPCM excited-state calculations were the same as those employed by Sen et al. to obtain the aqueous experimental spectra of the nucleobases.

3.3 Results and Discussion

3.3.1 Iodide

B3LYP, CAM-B3LYP, M062X, M11 and MN12-SX in conjunction with the LANL2DZ basis set were used to perform the electronic ground state and TDDFT calculations on I⁻. The TDDFT calculations (at 10 and 30 states) of I⁻, both produced spectra in which no bands were present, as expected due to the lack of any stable (i.e. undetached) excited states for I⁻.

3.3.2 Isolated Nucleobases

3.3.2.a. Uracil

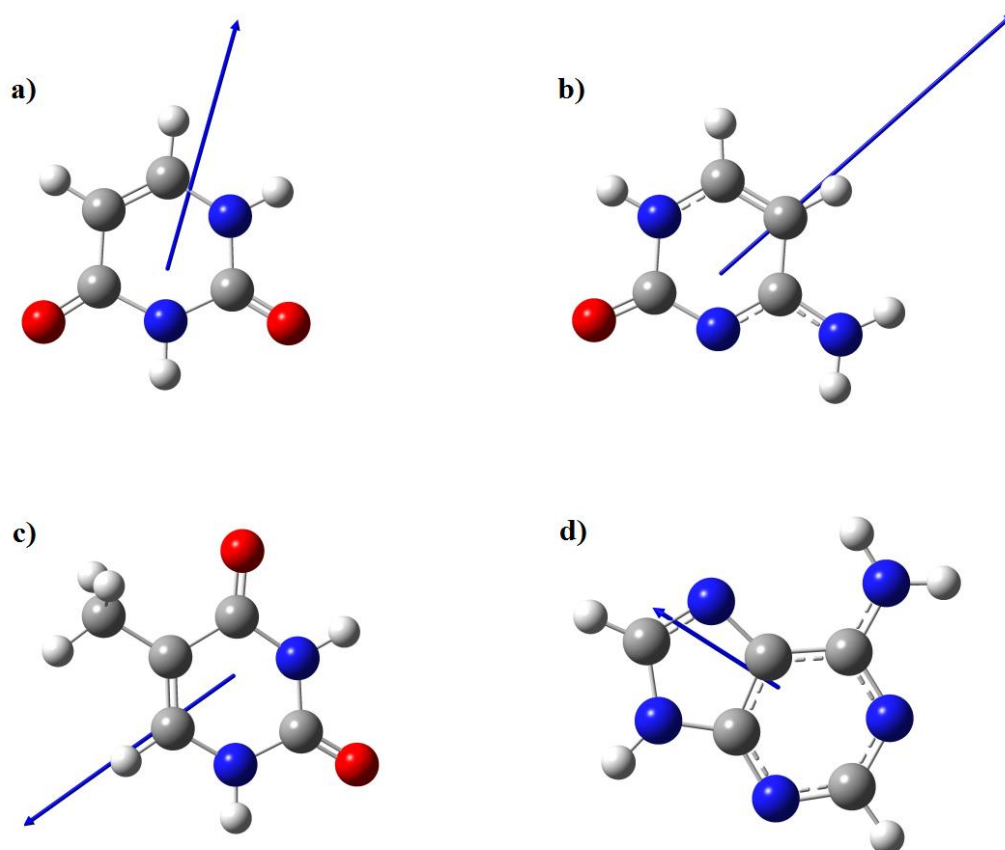


Figure 3.1: The B3LYP/LANL2DZ optimised ground state structures of a) uracil b) cytosine c) thymine and d) adenine. The magnitude and direction of the dipole moments of these nucleobases are represented by the blue vector.

Figure 3.1a depicts the B3LYP/LANL2DZ optimised ground-state structure of uracil. Within this planar arrangement, the $N\cdots H$ and $C\cdots H$ bond lengths were calculated as 1.01 and 1.08 Å respectively and the dipole moment was 4.93 Debye. These results are in good agreement with other theoretical values available in the literature and thus provide support for the level of theory used here.^{104,105} No imaginary frequencies were found during the ground-state calculation, indicating that the optimised structure represents a true PES minimum.

Following optimisation, TDDFT calculations were performed using a range of density functional and basis set combinations. These combinations are listed in Table 3.1, along with the resulting excitation energies. As can be seen from this table, all functional/basis set combinations reproduced the two spectral bands seen in the experimental spectra, along with an additional third band at around 7.6 eV (above the spectral range). 10 states were found to be sufficient for these calculations.

Table 3.1: Computed and experimental excitation energies (in eV) of uracil, where **a**, **b** and **c** are the lowest energy spectral bands.^{a,b}

Functional	LANL2DZ			6-311++G(2d,2p)			Def2-TZVPP		
	a	b	c	a	b	c	a	b	c
B3LYP	5.10	6.36	7.28	5.17	6.45	7.42	5.22	6.57	7.60
CAM-B3LYP	5.46	6.82	7.64	5.46	6.89	7.77	5.54	7.01	7.97
M062X	5.54	6.91	7.68	5.50	6.89	7.78	5.58	7.05	7.93
M11	5.59	7.04	7.68	5.52	7.02	7.70	5.59	7.14	7.95
MN12-SX	5.38	6.72	7.62	5.36	6.56	7.50	5.45	6.97	8.01
PBE0	5.28	6.60	7.50	5.30	6.66	7.63	5.37	6.75	7.78
Experimental ^b	4.80	6.12	-	4.80	6.12	-	4.80	6.12	-

^a Calculations performed at 10 states

^b Aqueous UV absorption experimental data (courtesy of Sen et al.).^{41,42}

Table 3.2: Mean absolute errors in excitation energy (eV) associated with TDDFT/LANL2DZ calculations of uracil at 10 states

Functional	Mean Absolute Error (eV)
B3LYP	0.27
CAM-B3LYP	0.68
M062X	0.77
M11	0.86
MN12-SX	0.59
PBE0	0.48

Further analysis of the excitation energy variations is provided in Table 3.2, where the mean absolute errors (MAEs) have been calculated for the various functionals using the LANL2DZ basis set. The B3LYP functional was shown to have the lowest error of 0.27 eV, indicating it had the highest accuracy. As shown in Figure 3.2 below, a good agreement was found between the B3LYP/LANL2DZ and experimental UV spectra. The next accurate functional was PBE0, however it had an error nearly double that of B3LYP, making its use unsuitable.

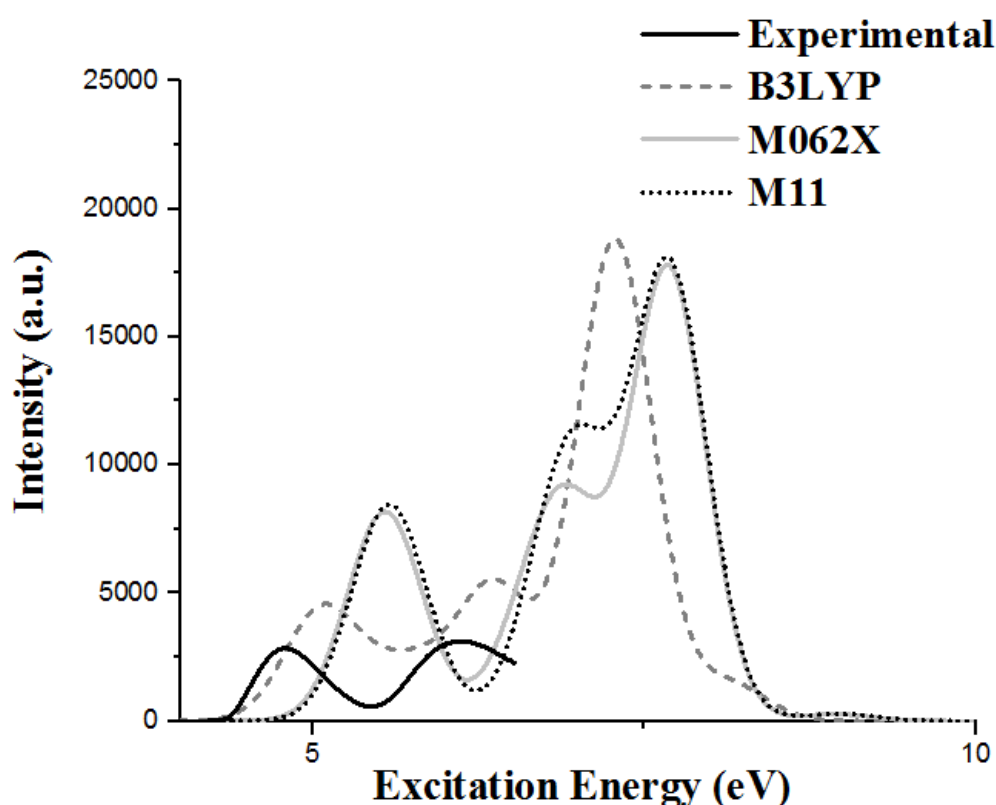


Figure 3.2: Comparison of the computational and experimental UV spectra of uracil: — Experimental UV spectrum (courtesy of Sen et al.),^{41,42} - - - B3LYP/LANL2DZ, — M062X/LANL2DZ and M11/LANL2DZ.

M11 followed by M062X displayed the least accuracy, with its results consistently much higher than the corresponding experimental data (Table 3.1). A poor agreement was found between the M062X, M11 and experimental UV spectra. As shown in Figure 3.2, M062X/LANL2DZ and M11/LANL2DZ over predicted the excitation energies of the experimental spectral bands. It is interesting to observe that the intensity of the lowest energy

band produced by M062X/LANL2DZ and M11/LANL2DZ was considerably higher than that of B3LYP/LANL2DZ.

The inclusion of exact exchange into hybrid B3LYP and PBE0 functionals is likely to be responsible for the relatively good performance of these functionals. The Hartree-Fock exchange component of these functionals partially cancels out the self-interaction error present in DFT.¹⁰⁶ Although the M11 and M062X functionals are also hybrid in nature, they contain a larger percentage of Hartree-Fock (exact) exchange. An increase in percentage Hartree-Fock exchange should result in a more accurate description of ground-state quantities. However, various studies have acknowledged that while systematic increases in percentage exact exchange may provide a more accurate description of electronic ground-state properties such as kinetics, it adversely affects the quality of excitation energies results.^{107,108} Using this theory, the satisfactory performance of MN12-SX can be explained by its Hartree-Fock component being comparable to that of B3LYP.

Despite the comparatively good performance of B3LYP in this study, its inability to predict excitation energies accurately using TDDFT is a well-recognised failure of B3LYP.⁶¹ This failure can be attributed to the incorrect behaviour of the exchange interaction potential at long range. In CAM-B3LYP, the exchange potential is range separated and exact exchange is largely used to describe long-range interactions.¹⁰⁸ These modifications rectify the long-range behaviour of the exchange potential, therefore CAM-B3LYP was expected to predict the excitation energies of uracil with greater accuracy than B3LYP. However, in this respect, CAM-B3LYP performed poorly, overestimating the excitation energies. The underperformance of CAM-B3LYP could be due to dispersion forces not being as significant in the system in question. To summarise, the order of accuracy was deduced as follows:
B3LYP > PBE0 > MN12-SX > CAM-B3LYP > M062X > M11.

Following the analysis of the density functionals, the basis set used was also varied to study its effects on the excitation energies. The results of these basis set comparisons are outlined in Table 3.1 and the corresponding MAEs have been calculated in Table 3.3.

Table 3.3: Mean absolute errors in excitation energy (eV) associated with TDDFT calculations of uracil at 10 states.

Functional	LANL2DZ	6-311++G(2d,2p)	Def2-TZVPP
B3LYP	0.27	0.35	0.33
CAM-B3LYP	0.68	0.72	0.71
M062X	0.77	0.74	0.75
M11	0.86	0.81	0.80
MN12-SX	0.59	0.50	0.64
PBE0	0.48	0.52	0.49

Interestingly, the trend witnessed previously in density functional performance remained unchanged when the basis set is varied. B3LYP/LANL2DZ proved to be the best performing combination while M11/LANL2DZ was shown to be the worst. The order of basis set performance can be summarised as LANL2DZ > 6-311++G (2d,2p) > Def2-TZVPP.

Generally, both LANL2DZ and 6-311++G (2d,2p) performed well, producing results with a high degree of accuracy. However, LANL2DZ was deemed to be the better performing basis set of the two due to its lower CPU time cost. On average, the 6-311++G (2d,2p) set took 2.62 hours longer than LANL2DZ to complete a TDDFT calculation for Uracil at 20 states.

The Def2-TZVPP basis set was deemed to be the worst performing following analysis of its MAEs and computational time. Although the MAEs recorded for Def2-TZVPP were not grossly higher than those of LANL2DZ, examination of the TDDFT/Def2-TZVPP spectra in Figure 3.3 revealed that Def2-TZVPP consistently, overestimated the positions of the higher energy spectral bands. As the MAEs only take into account the lowest energy spectral

bands, the significant overestimation of the higher energy bands by Def2-TZVPP is not reflected.

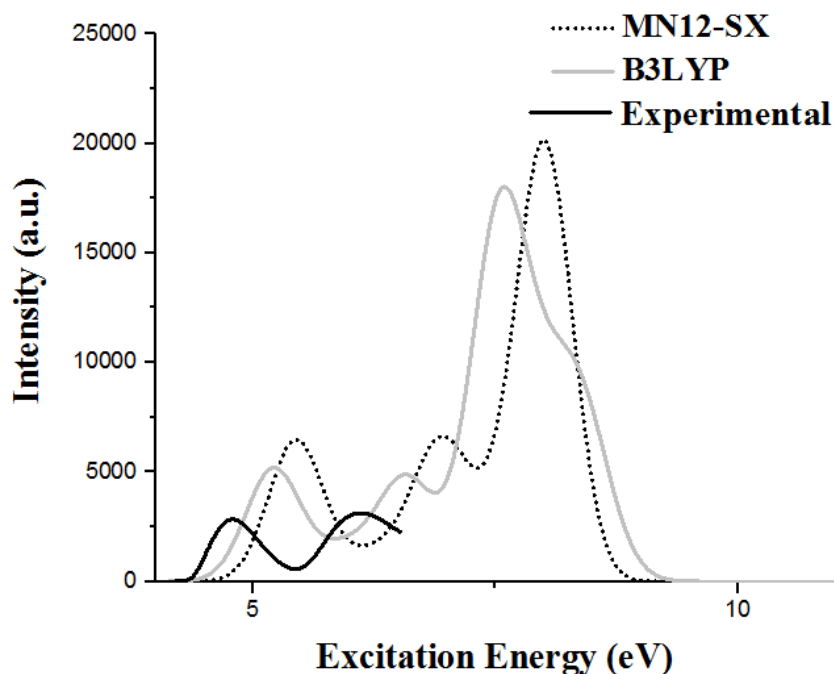


Figure 3.3: Comparison of the theoretical and experimental UV spectra of uracil: — Experimental UV spectrum (courtesy of Sen et al.),^{41,43} — B3LYP/Def2-TZVPP and MN12-SX/Def2-TZVPP.

The lengthy computational time associated with performing calculations confirmed the unsuitability of this basis set. On average, it took 2.25 hours longer than the LANL2DZ basis set to perform a TDDFT calculation for uracil at 20 states. As these results have been performed for a relatively small system, it is clear that the use of this basis set would be unsuitable for the larger I·Nu complexes. This high CPU time cost can be straightforwardly explained by the relatively large size of this triple-zeta basis set.

It must also be acknowledged that some error in the excitation energies would have arisen from the comparison of the experimental and theoretical spectra in different phases. The experimental UV absorption spectrum of uracil was in solution phase, whilst the theoretical UV spectra were calculated in vacuo. In order to probe the effect of the solvent on the

excitation energies, the theoretical UV spectrum of uracil was calculated in solution at B3LYP/LANL2DZ level using the default Gaussian model IEFPCM. The computational excitation energies produced from the TD-IEFPCM calculation are listed in Table 3.4, where they have also been compared to computational gas-phase results and experimental excitation energies.

Table 3.4: Comparison of the computed excitation energies of uracil (*in vacuo* and solution) with experimental results, where **a**, **b** and **c** are the lowest energy spectral bands.^{a-c}

	Excitation Energy (eV)		
	a	b	c
Vacuum ^a	5.10	6.37	7.27
Solution ^b	5.00	6.16	7.20
Experimental ^c	4.80	6.12	-

^a TD-B3LYP/LANL2DZ calculation performed at 10 states

^b TDDFT calculation performed at IEFPCM/B3LYP/LANL2DZ level (10 states) and employed water as the solvent.

^c Aqueous UV absorption spectrum obtained by Sen et al.^{41, 43}

In comparison to the gas-phase computational results (Table 3.4), the TD-IEFPCM calculation produced lower excitation energies for uracil. As seen in Figure 3.4, the addition of solvation to TD-B3LYP/LANL2DZ results in the considerable hypsochromic shift of the gas-phase absorption spectrum. Consequently, a better agreement between the experimental and (solution-phase) computational spectra is found. For the excitations at 5.10, 6.37 and 7.27 eV, the solvent shifts (of the theoretical spectra) were 0.10, 0.21 and 0.07 eV, respectively.

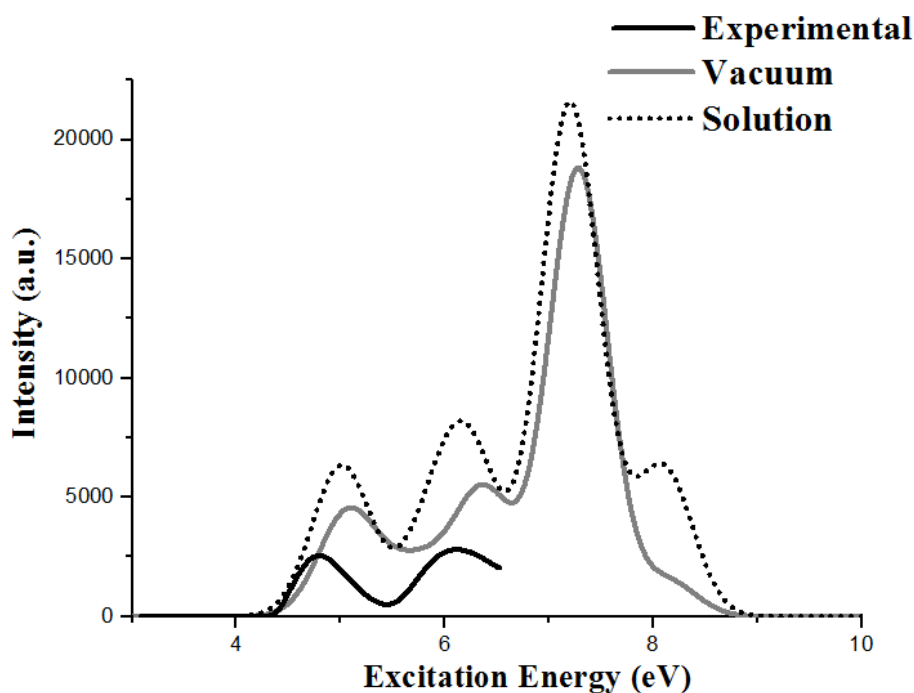


Figure 3.4: Comparison of the experimental and theoretical electronic spectra of uracil:

— Experimental aqueous UV absorption (courtesy of Sen et al.),⁴¹ — Gas phase B3LYP/LANL2DZ (10 states) and Solution phase IEFPCM/B3LYP/LANL2DZ (10 states).

Aside from the excitation energies, there are notable differences in the aqueous and gas phase B3LYP/LANL2DZ spectra. The IEFPCM/B3LYP/LANL2DZ calculation at 10 states produced four distinct bands at 5.00, 6.16, 7.20 and 8.06 eV. Although present, the intensity of the highest energy band was comparatively low in the gas-phase B3LYP/LANL2DZ spectrum. As shown in Figure 3.4 above, the highest energy band is present on the rise edge of the adjacent band at 7.27 eV. Interestingly, all of the bands in the solution-phase computational spectrum were of greater intensity to that in the gas-phase theoretical spectrum.

As B3LYP/LANL2DZ was shown to have produced the most accurate results, this data set was used in the assignment of the excited-state transitions. In Table 3.5, these transitions are detailed. The three absorption bands present in the spectra at 5.10, 6.36 and 7.28 eV all

corresponded to transitions that were $\pi \rightarrow \pi^*$ in nature. These theoretical results confirm the assignment made previously by Sen et al.⁴¹ As previously discussed, Sen et al. investigated the UV photophysics of $\text{Pt}(\text{CN})_n^{2-}$ ·uracil complexes and their isolated $\text{Pt}(\text{CN})_n^{2-}$ and uracil monomers. These studies produced the aqueous UV absorption spectrum of uracil shown in Figure 3.5.^{41,43} Sen et al. characterised the nature of the transition at 4.80 eV as $\pi \rightarrow \pi^*$.⁴¹

Table 3.5: Assignment of the four lowest energy excited-state transitions of uracil using B3LYP/LANL2DZ data.

Excitation Energy (eV)	Oscillator Strength (a.u.)	MO Transition	CI Coefficient (% contribution)	Assignment of Transition
4.38	0.0001	HOMO-1 \rightarrow LUMO	0.68270 (93.22)	$n \rightarrow \pi^*$
5.08	0.1090	HOMO \rightarrow LUMO	0.64971 (84.42)	$\pi \rightarrow \pi^*$
6.37	0.1302	HOMO \rightarrow LUMO+1	0.64664 (83.63)	$\pi \rightarrow \pi^*$
7.28	0.4635	HOMO-2 \rightarrow LUMO+1	0.65572 (85.99)	$\pi \rightarrow \pi^*$

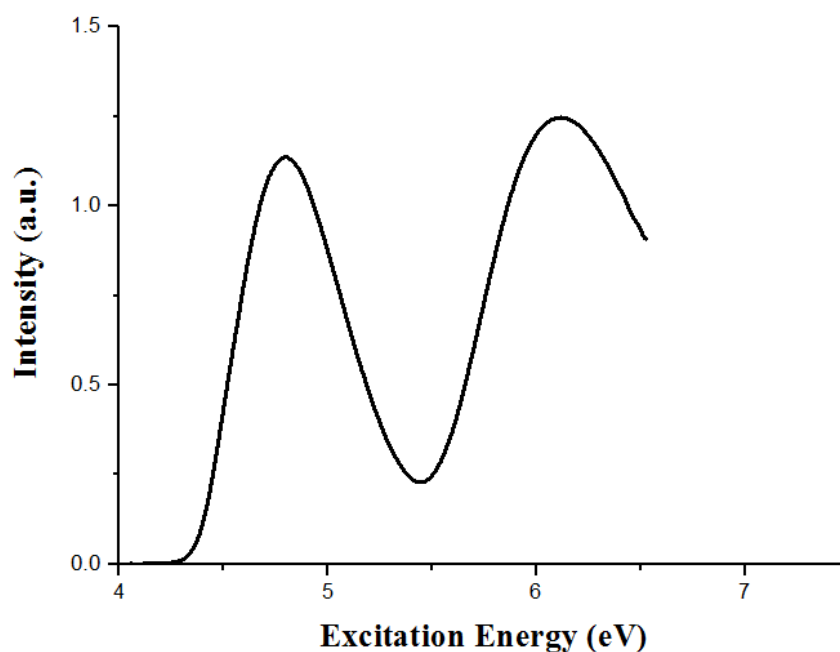


Figure 3.5: Experimental aqueous UV absorption spectrum of uracil (courtesy of Sen et al.).^{41,43}

Also present within the calculated spectra was a forbidden transition occurring at 4.38 eV. Upon inspection of the relevant MOs (Figure 3.6), this transition was identified as being $n \rightarrow \pi^*$ in nature. The assignments presented here are in line with results of an earlier investigation conducted by Ren et al.⁷⁷ In this computational study, TDDFT level calculations were used to analyse the spectral shifts for the two lowest energy excited-state transitions occurring within solvated uracil.

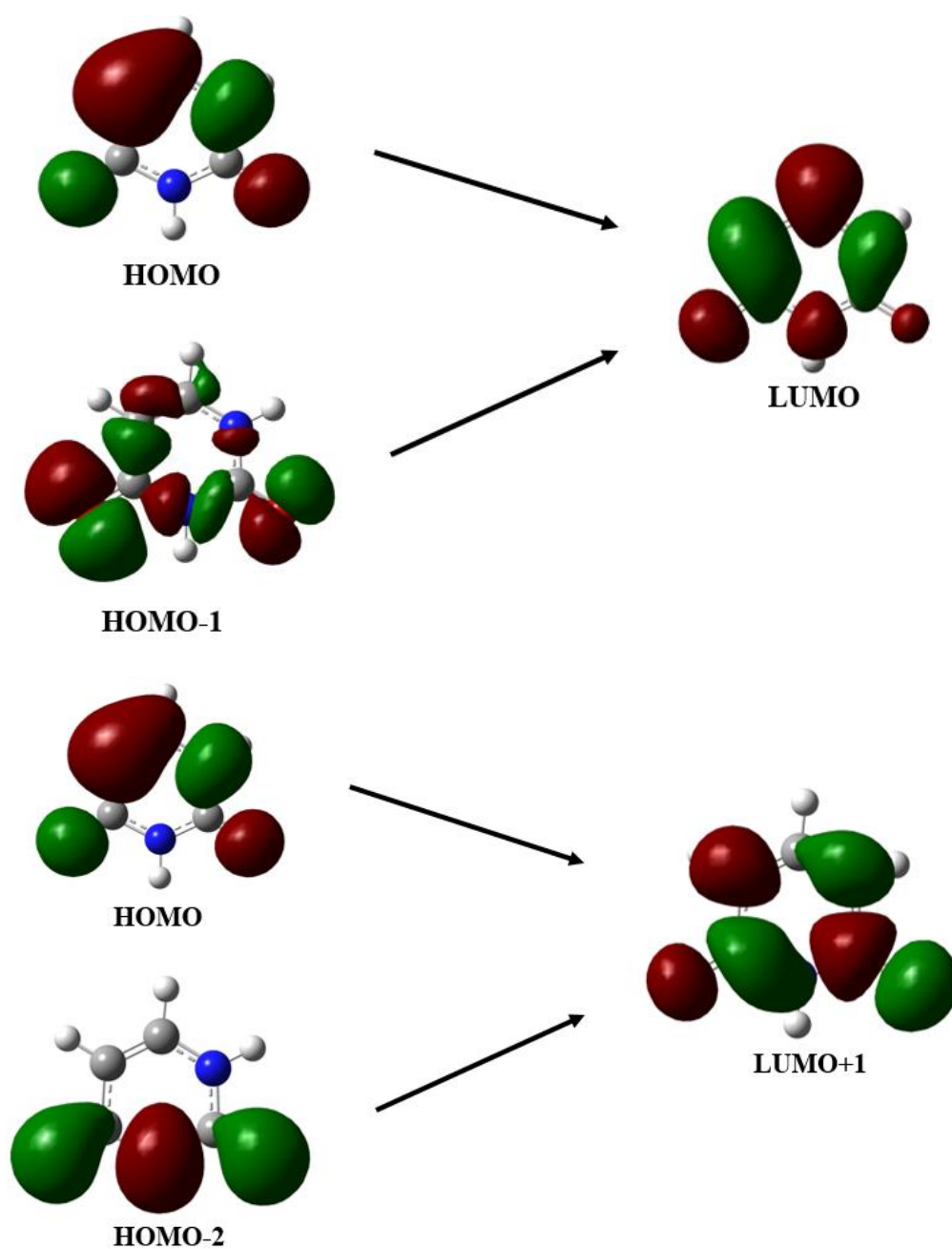


Figure 3.6: MOs involved in the electronic transitions of uracil. MOs were calculated at the B3LYP/LANL2DZ level of theory.

3.3.2.b. Cytosine

Preliminary DFT calculations were carried out and the ground-state properties of the resulting structure were analysed. The dipole moment was observed as 7.41 Debye and lay agreeably between the reported experimental values of 6.8 and 8 Debye.¹⁰⁹ No imaginary frequencies were found.

In order to validate the basis set and density functional trends set by uracil, TDDFT calculations were performed using the same density functional/basis set combinations that were employed previously, with the results presented in Table 3.6. Analysis of the results showed that at 10 states, three bands were produced at the following average excitation energies: 4.8, 5.8 and 6.8 eV.

Table 3.6: Computed and experimental excitation energies of cytosine, where **a**, **b** and **c** are the lowest energy spectral bands.^{a,b}

Functional	LANL2DZ			6-311++G(2d,2p)			DEF2-TZVPP		
	a	b	c	a	b	c	a	b	c
B3LYP	4.55	5.37	6.55	4.64	5.43	6.55	4.75	5.50	6.78
CAM-B3LYP	4.94	5.91	6.82	5.02	5.94	6.75	5.06	6.03	7.00
M062X	5.02	5.98	6.80	5.06	5.98	6.70	5.11	6.09	6.92
M11	5.10	6.12	6.82	5.13	6.09	6.60	5.20	6.23	6.91
MN12-SX	4.73	5.63	6.80	4.78	5.42	6.49	4.90	5.74	7.04
PBE0	4.72	5.58	6.74	4.83	5.61	6.72	4.94	5.73	6.98
Experimental ^b	4.64	6.00	6.12	4.64	6.00	6.12	4.64	6.00	6.12

^a All calculations were performed at 10 states

^b Aqueous UV absorption spectrum obtained by Sen et al.⁴³

Table 3.7: Mean absolute errors in excitation energy (eV) associated with TDDFT calculations of cytosine at 10 states.

Functional	LANL2DZ	6-311++G(2d,2p)	Def2-TZVPP
B3LYP	0.27	0.35	0.33
CAM-B3LYP	0.68	0.72	0.71
M062X	0.77	0.74	0.75
M11	0.86	0.81	0.80
MN12-SX	0.59	0.50	0.64
PBE0	0.48	0.52	0.49

Table 3.7 provides the MAEs for cytosine for the different density functional/basis set combinations used. Initial inspection of the results showed only slight differences in error irrespective of the functional and basis sets. These differences were incredibly minor between the LANL2DZ and 6-311++G (2d,2p) basis sets, especially. As for uracil, Def2-TZVPP produced the most inaccurate results with an average error for cytosine of 0.47 eV.

Inspection of the experimental and computational spectra offers an explanation for the small error differences observed overall. It can be seen in the experimental spectrum of cytosine (Figure 3.7) that while the lowest and highest energy bands are well defined, the second band at 6 eV is not. This band is present as a peak on the rising edge of the highest energy band. If the computational and experimental energies of the highest and lowest energy bands are compared (Table 3.6), the trends observed for uracil are reproduced.

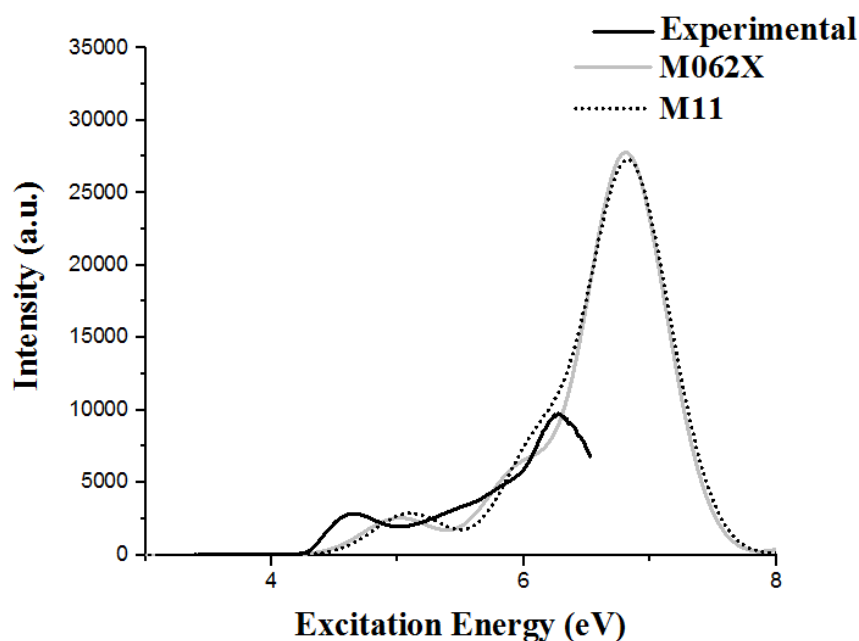


Figure 3.7: Comparison of the theoretical and experimental UV spectra of cytosine: — Experimental UV spectrum (courtesy of Sen et al.),⁴³ — M062X/LANL2DZ and M11/LANL2DZ.

B3LYP/6-311++G(2d,2p) and B3LYP/LANL2DZ give the most accurate results in terms of predicting the experimental excitation energies, followed by MN12-SX/LANL2DZ and MN12-SX/6-311++G(2d,2p). The introduction of the middle band into the calculations distorts the MAEs because M11 and M062X were the only functionals to describe accurately the shape and position of the second band. This results in lower MAEs for the M11 and M062X, making them appear to be as accurate as the other functionals. The poor agreement between the M062X, M11 and experimental spectra can be seen in Figure 3.7, where the position of the experimental spectral bands were overestimated by M062X/LANL2DZ and M11/LANL2DZ. Interestingly, M11/LANL2DZ was the only functional to describe accurately the position of the middle spectral band as being on the rising of the highest energy band.

As the experimental band at 6.12 eV was the most intense, it was used as the determining factor in the assessment of the functional and basis set performance. Comparison with that

band indicated that MN12-SX/6-311++G(2d,2p) was the most accurate functional. However, due to the high CPU time cost associated with this combination, B3LYP/LANL2DZ provides the best balance between accuracy and computational cost.

The MAEs associated with the various functional/ basis set combinations can in part be attributed to the comparison of experimental and theoretical results that are in different phases. All TDDFT calculations were conducted in gas-phase and were compared to aqueous experimental results. The extent to which solvation affects the theoretical excitation energies of cytosine was investigated using IEFPCM. As B3LYP/LANL2DZ was deemed to be the best performing functional/basis set combination, it was employed in an IEFPCM/TDDFT calculations at 10 states. The solvent used in this calculation, water, was the same as that used by Sen et al. to produce the aqueous experimental spectrum of cytosine. The excitation energies produced by IEFPCM/B3LYP/LANL2DZ have been compared to the gas-phase theoretical and aqueous experimental energies of cytosine in Table 3.8.

Table 3.8: Comparison of the computed excitation energies of cytosine (*in vacuo* and solution) with experimental results, where **a**, **b**, **c** and **d** are the lowest energy spectral bands.
a-c

	Excitation Energy (eV)			
	a	b	c	d
Vacuum ^a	4.52	5.37	6.55	-
Solution ^b	4.73	5.47	6.46	7.85
Experimental ^c	4.64	6.00	6.39	-

^a TD-B3LYP/LANL2DZ calculation at 10 states

^b IEFPCM/B3LYP/LANL2DZ calculation at 10 states, modelled in a solution of water.

^c Aqueous UV absorption spectrum (courtesy of Sen et al.).⁴³ Water was used to solvate cytosine.

In comparison to the gas-phase theoretical results, IEFPCM/B3LYP/LANL2DZ predicted higher excitation energies for the two lowest absorption bands. The resulting bathochromic shift of the two lowest spectral bands can be seen in Figure 3.8, where the solution and gas-

phase theoretical spectra have been compared. Using the values in Table 3.8, bathochromic shifts of 0.21 and 0.10 eV were calculated for the two lowest energy bands, respectively. Conversely, a hypsochromic shift of 0.09 eV was observed for the second highest energy band in the aqueous theoretical spectrum. As a result of the bathochromic and hypsochromic shifts, a better agreement between the experimental and theoretical spectra was found.

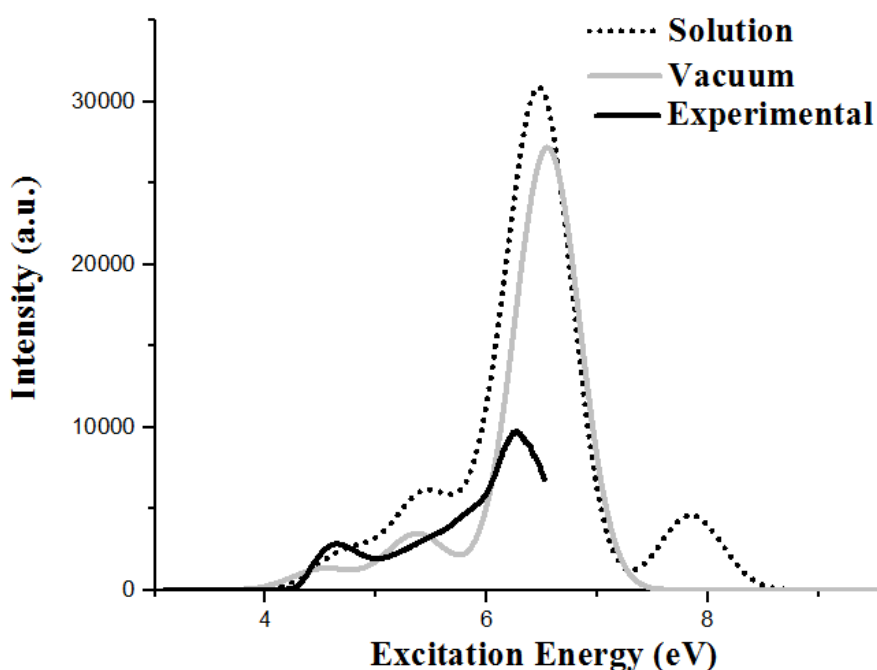


Figure 3.8: Comparison of the experimental and theoretical electronic spectra of cytosine: **—** Experimental aqueous UV absorption (courtesy of Sen et al.),⁴³ **—** Gas phase B3LYP/LANL2DZ (10 states) and **.....** Solution phase IEFPCM/B3LYP/LANL2DZ (10 states).

Similar to uracil, a significant hyperchromic shift was observed for all bands in the solution-phase spectrum. Interestingly, IEFPCM/B3LYP/LANL2DZ described the spectral band at 5.47 eV more accurately than gas-phase B3LYP/LANL2DZ. In the experimental spectrum, the second highest band is present on the rising edge of the highest energy band at 6 eV. IEFPCM/B3LYP/LANL2DZ reproduced the relatively low intensity and position of this spectral band better than the gas-phase B3LYP/LANL2DZ calculation. Also similar to uracil, an additional spectral band was produced by IEFPCM/B3LYP/LANL2DZ at 10 states. The

additional fourth band (seen at 7.85 eV in the IEFPCM/B3LYP/LANL2DZ spectrum), was not observed in the gas-phase B3LYP/LANL2DZ results or aqueous experimental results.

An interpretation of the dominant transitions occurring at the three excitation energies is presented in Table 3.9. The MOs involved in these transitions are displayed in Figure 3.9.

Table 3.9: Assignment of the three lowest energy excited-state transition of cytosine using B3LYP/LANL2DZ.

Excitation Energy (eV)	Oscillator Strength (a.u.)	MO Transition	CI Coefficient (% contribution)	Assignment of Transition
4.52	0.0310	HOMO → LUMO	0.69845 (97.57)	$\pi \rightarrow \pi^*$
5.37	0.0848	HOMO-2 → LUMO	0.64797 (89.97)	$\pi \rightarrow \pi^*$
6.58	0.5658	HOMO → LUMO+1	0.49066 (48.15)	$\pi \rightarrow \pi^*$

Similarly to uracil, all three bands were attributed to $\pi \rightarrow \pi^*$ transitions with the lowest energy band involving electron density movement from the HOMO to LUMO. The percentage contribution of the highest energy transition at 6.58 eV was relatively low (48.15%). With such a value, there is doubt if the HOMO→LUMO+1 transition can be viewed as truly representative of all the excitations occurring at that particular energy.

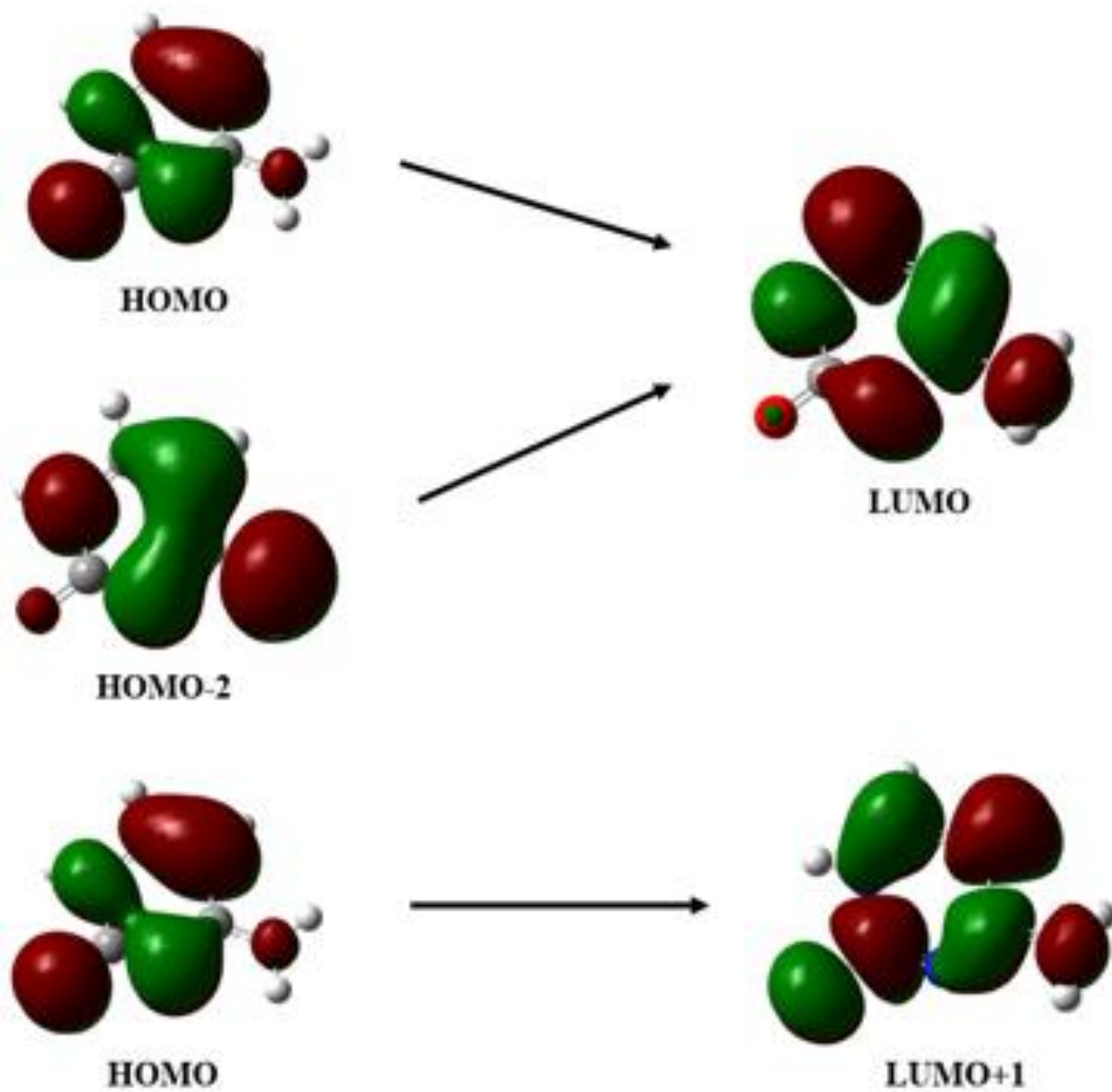


Figure 3.9: MOs involved in the electronic transitions of cytosine. MOs were calculated at the B3LYP/LANL2DZ level of theory.

3.3.2.c Thymine

The results presented previously for uracil and cytosine had indicated that LANL2DZ is the best performing basis set. Therefore, it was the only basis set employed in calculations for thymine, including the density functionals comparisons.

The ground-state geometry generated by the DFT calculation is depicted in Figure 3.1c. The key bond lengths such as O \cdots H (1.25 Å) and N \cdots H (1.08 Å) compared favourably to both theoretical and experimental literature values.⁸⁴ As a consequence of their similar geometric arrangements, the calculated dipole moment was very close to that of uracil at 4.92 Debye.

As demonstrated in Table 3.10, all TDDFT calculations that were performed at 10 states produced three absorption bands at ca. 5.2, 6.5 and 7.6 eV. Inspection of the MAEs in Table 3.11 revealed once again that B3LYP/LANL2DZ produces the most accurate results with a relatively small error of 0.16 eV associated with the calculation. B3LYP/LANL2DZ was shown to have predicted the energy the second band incredibly accurately. It displayed a difference of only 0.05 eV between the theoretical and experimental values. This accuracy is also reflected in the MAEs, which are the lowest overall for thymine in comparison to the other nucleobases.

Table 3.10: Computed and experimental excitation energies of thymine, where **a**, **b** and **c** are the lowest energy spectral bands.^{a,b}

Functionals	Excitation Energy (eV)		
	a	b	c
B3LYP	4.91	6.06	7.30
CAM-B3LYP	5.29	6.63	7.69
M062X	5.38	6.73	7.74
M11	5.42	6.84	7.78
MN12-SX	5.17	6.43	7.65
PBE0	5.08	6.30	7.52
Experimental ^b	4.65	5.99	-

^a All calculations were performed at 10 states.

^b Aqueous UV absorption spectrum obtained by Sen et al.⁴³

Table 3.11: Mean absolute errors in excitation energy (eV) associated with TDDFT/LANL2DZ calculations of thymine at 10 states.

Functional	Mean Absolute Error (eV)
B3LYP	0.17
CAM-B3LYP	0.64
M062X	0.74
M11	0.81
MN12-SX	0.48
PBE0	0.37

In keeping with the trends displayed by uracil and cytosine, the next best performing functional was shown to be MN12-SX. The least accurate functionals were again M11 and M062X. These functionals tended to grossly overestimate the energy of the absorptions bands. In addition to this, the oscillator strengths are also significantly overestimated in the M062X and M11 UV spectra (Figure 3.10), thus providing a less accurate reproduction of the experimental spectra.

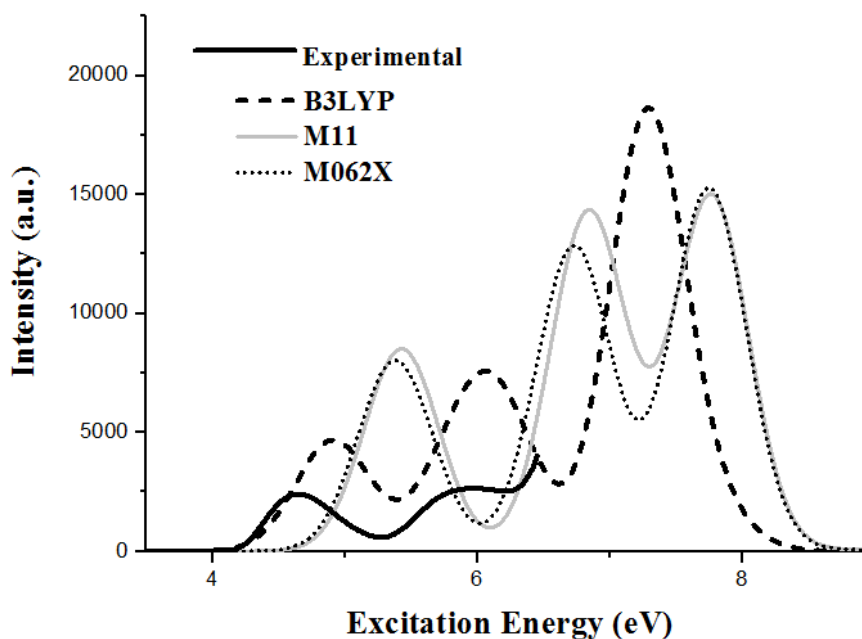


Figure 3.10: Comparison of the experimental and theoretical electronic spectra of thymine:

— Experimental aqueous UV absorption (courtesy of Sen et al.),⁴³ — M11/LANL2DZ, - - - B3LYP/LANL2DZ and M062X/LANL2DZ.

Using the B3LYP/LANL2DZ TDDFT data set, the excitations occurring at 4.91, 6.18 and 7.29 eV were deduced as being HOMO \rightarrow LUMO, HOMO \rightarrow LUMO+1 and HOMO-2 \rightarrow LUMO+1, respectively (Table 3.12). Examination of the shape of these MOs (Figure 3.11) confirmed that all three transitions are $\pi \rightarrow \pi^*$ in nature.

Table 3.12: Assignment of the three lowest energy excited state transitions of thymine using B3LYP/LANL2DZ data.

Excitation Energy (eV)	Oscillator Strength (a.u.)	MO Transition	CI Coefficient (% contribution)	Assignment of Transition
4.91	0.1151	HOMO \rightarrow LUMO	0.66640 (88.82)	$\pi \rightarrow \pi^*$
6.18	0.1301	HOMO \rightarrow LUMO+1	0.62572 (78.31)	$\pi \rightarrow \pi^*$
7.29	0.4534	HOMO-2 \rightarrow LUMO+1	0.65676 (86.27)	$\pi \rightarrow \pi^*$

Referring overleaf to Figure 3.11, it is interesting to compare the difference in shape between the HOMO and HOMO-2 orbitals. Electron density in the HOMO is distributed around the system, with a large amount concentrated on the C4-C5 π bond. This typical π arrangement contrasts to that observed in the HOMO-2 orbital. Here, electron density is situated solely on the adjacent N-H, C=O and C-Me bonds and therefore occupies one half of the molecule. Nevertheless, both are still thought to be π in nature.

A theoretical study by Shukla et al. gives credence to this assignment.⁸⁴ In this work, the excited-state transitions for all five nucleobases were calculated using the B3LYP functional and a range of 6-311G type basis sets with varying degrees of added diffusion and polarisation. They assigned the corresponding excitation (7.43 eV) as also being $\pi \rightarrow \pi^*$ nature. They also put forward an explanation for the atypical nature of MOs involved in that

transition, as arising from Rydberg contamination. It was suggested Rydberg $\pi \rightarrow \sigma^*$ contamination of 25% was present at this excitation energy.

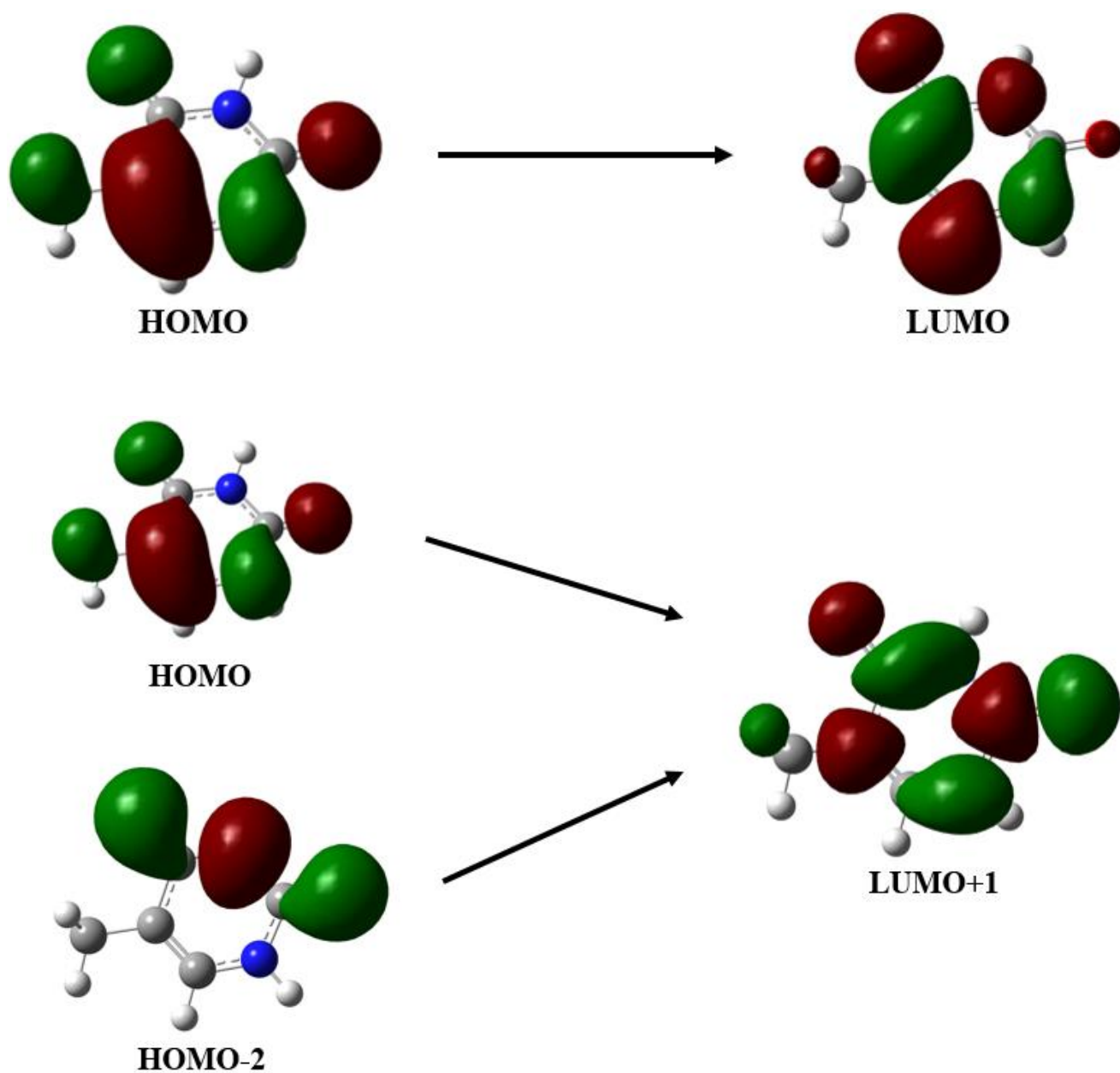


Figure 3.11: MOs involved in the electronic transitions of thymine. MOs were calculated at the B3LYP/LANL2DZ level of theory.

To study the effect of solvation on the excitation energies, a TDDFT calculation was performed in solution using IEFPCM. As B3LYP/LANL2DZ was deemed the best performing basis sets in terms of the excitation energy predications, it was used to calculate the solution-phase UV spectrum of thymine. The IEFPCM/B3LYP/LANL2DZ calculation was conducted at 10 states. The excitation energies produced by the solution-phase B3LYP/LANL2DZ calculation is outlined in Table 3.13.

Table 3.13: Comparison of the computed excitation energies of thymine (*in vacuo* and solution) with experimental results, where **a**, **b** and **c** are the lowest energy spectral bands.^{a-c}

	Excitation Energy (eV)		
	a	b	c
Vacuum ^a	4.91	6.06	7.30
Solution ^b	4.85	5.98	7.23
Experimental ^c	4.65	5.99	-

^a TD-B3LYP/LANL2DZ calculation at 10 states

^b IEFPCM/B3LYP/LANL2DZ calculation at 10 states, modelled in a solution of water.

^c Aqueous UV absorption spectrum obtained by Sen et al.⁴³ Water was used to solvate cytosine.

At 10 states, IEFPCM/B3LYP/LANL2DZ reproduced the three spectral bands seen in the gas phase B3LYP/LANL2DZ spectrum. In comparison to the gas-phase theoretical spectrum, the excitation energies the three bands in the solution-phase theoretical spectrum were smaller. The hypsochromic shifts of 0.06 and 0.08 eV for the respective bands at 4.85 and 5.98 eV in the B3LYP/LANL2DZ solution-phase spectrum, brings the theoretical solution-phase spectrum into very good agreement with the experimental spectrum (Figure 3.12). In particular, the position of the highest energy band in the experimental spectrum is predicted extremely accurately by IEFPCM/B3LYP/LANL2DZ. The difference between the excitation

energies of the second highest spectral band in the theoretical and experimental spectra is reduced by the inclusion of IEFPCM to 0.01 eV.

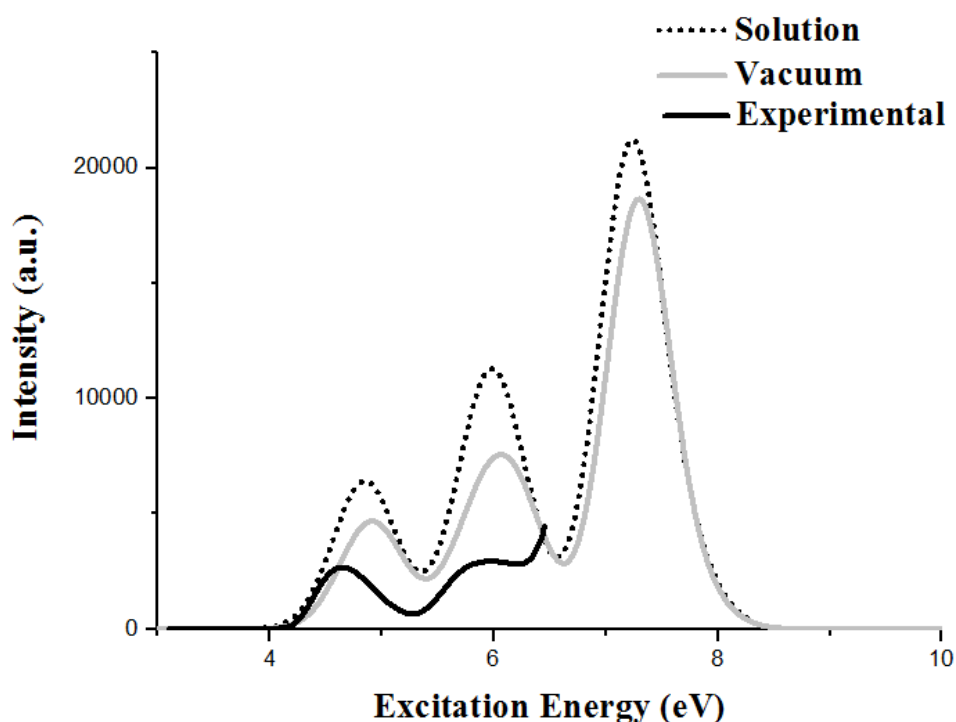


Figure 3.12: Comparison of the experimental and theoretical electronic spectra of thymine: **—** Experimental aqueous UV absorption (courtesy of Sen et al.),⁴³ **—** Gas-phase B3LYP/LANL2DZ (10 states) and **.....** Solution-phase IEFPCM/B3LYP/LANL2DZ (10 states).

3.3.2.d Adenine

Figure 3.1d illustrates the ground-state structure of B3LYP/LANL2DZ optimised adenine. In this diagram, the arrow representing the magnitude of the dipole moment (2.62 Debye) is shown to originate from the centre of mass. This result is comparable to those obtained by Ran et al.¹¹⁰ The N-H and C=N bonds crucial in hydrogen bonding were measured as 1.01 Å and 1.36 Å respectively. The results are also in line with those available in literature.¹¹¹

Following geometry optimisation, TDDFT calculations were carried out at 10 and 20 states using the following functionals and the LANL2DZ basis set: B3LYP, CAM-B3LYP,

M062X, M11, MN12-SX and PBE0. LANL2DZ was shown to be the best performing basis set during earlier investigations with cytosine and uracil and so was used exclusively in these calculations. Performing calculations at 20 states was found to be sufficient to produce the three bands observed in the experimental spectrum. The excitation energies produced by the various functionals are listed in Table 3.14 below.

Table 3.14: Computed and experimental excitation energies for adenine, where **a**, **b** and **c** are the lowest energy spectral bands.^{a,b}

Functionals	Excitation Energy (eV)		
	a	b	c
B3LYP	5.02	6.41	7.22
CAM-B3LYP	5.44	6.76	7.68
M062X	5.52	6.83	7.68
M11	5.60	6.90	7.78
MN12-SX	5.24	6.68	7.56
PBE0	5.22	6.59	7.51
Experimental ^b	4.75	5.90	

^a All calculations were performed at 20 states

^b Aqueous UV absorption spectrum obtained by Sen et al.⁴³

Table 3.15: Mean absolute errors in excitation energy (eV) associated with TDDFT/LANL2DZ calculations of adenine at 20 states.

Functional	Mean Absolute Error (eV)
B3LYP	0.39
CAM-B3LYP	0.78
M062X	0.85
M11	0.93
MN12-SX	0.64
PBE0	0.58

The trend in density functional performance displayed by adenine is similar to that exhibited by the other nucleobases studied. Comparison between the experimental and theoretical excitation energies for the different functionals (Table 3.14), shows that B3LYP is the most accurate in the prediction of the experimental excitation energies, followed by MN12-SX.

M11 and M062X were judged to be the least accurate of the functionals with errors two times higher than B3LYP (Table 3.15).

Attention should be drawn to the magnitude of the MAEs for adenine. In contrast to the other nucleobases investigated, adenine had the highest calculated MAEs. This suggests a poorer agreement between the calculated and experimental spectra. Nevertheless, a relatively good agreement was found between the experimental and B3LYP/LANL2DZ spectra (Figure 3.13).

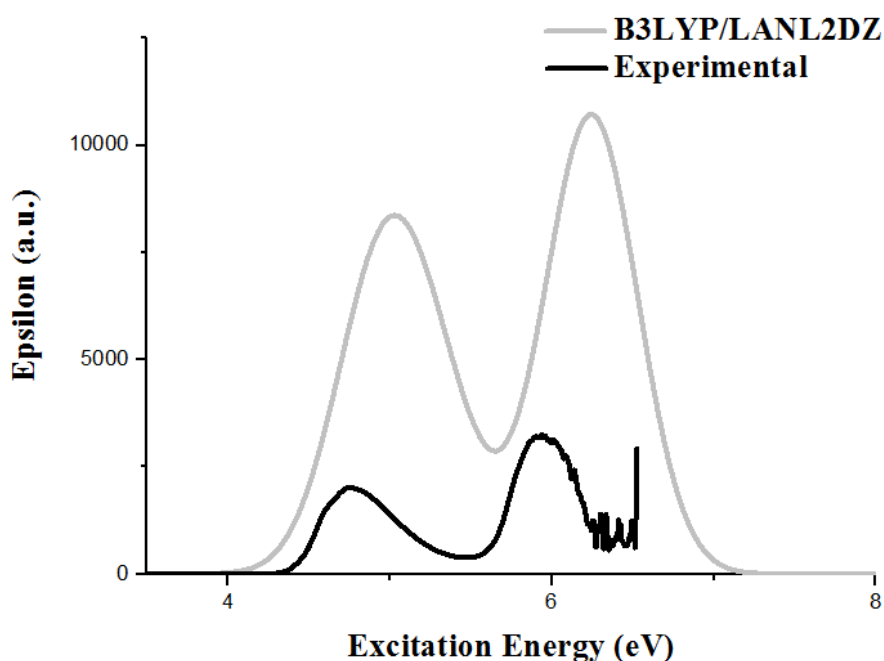


Figure 3.13: Comparison of the experimental and theoretical electronic spectra of adenine: — Experimental aqueous UV absorption (courtesy of Sen et al.) and — B3LYP/LANL2DZ.⁴³

The difference between the experimental and computational energies were in part due to the contrasting phases of the experimental and computational spectra. As the gas-phase computational spectrum was compared to solution-phase experimental spectrum, a systematic error in the MAEs could be present. To account for the difference between the gas and solution phase spectra, a TD-B3LYP/LANL2DZ calculation incorporating the IEFPCM

solvation model, was performed at 20 states on adenine. The resulting excitation energies produced by the IEFPCM/B3LYP/LANL2DZ are listed in Table 3.16.

Table 3.16: Comparison of the experimental and computational excitation energies (*in vacuo* and solution phase) of adenine, where **a**, **b**, **c** and **d** are the lowest energy spectral bands.

	Excitation Energy (eV)			
	a	b	c	d
Vacuum ^a	5.02	6.41	7.22	-
Solution ^b	4.99	6.28	6.99	8.28
Experimental ^c	4.75	5.94	-	-

^a TD-B3LYP/LANL2DZ calculation at 20 states

^b IEFPCM/B3LYP/LANL2DZ calculation at 20 states in methanol solution.

^c Aqueous UV absorption spectrum obtained from unpublished work by Sen et al. Methanol was used to solvated the nucleobase.

In comparison to the gas-phase theoretical UV spectrum, a notable hypsochromic shift of 0.03, 0.13 and 0.23 eV was seen for the respective three lowest energy spectral bands in the solution-phase B3LYP/LANL2DZ spectrum (Figure 3.14).

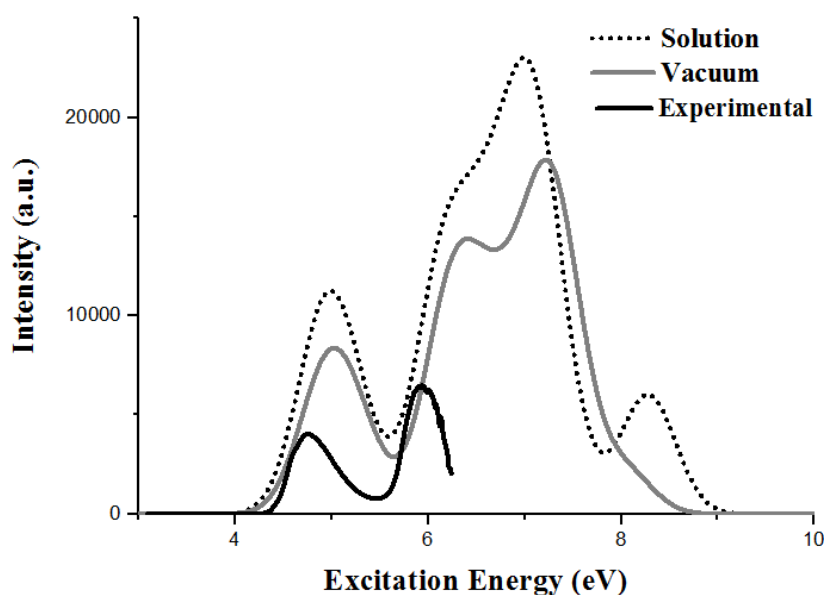


Figure 3.14: Comparison of the experimental and theoretical electronic spectra of adenine:

— Experimental aqueous UV absorption (courtesy of Sen et al.),⁴³ — Gas-phase B3LYP/LANL2DZ (10 states) and Solution-phase IEFPCM/B3LYP/LANL2DZ (10 states).

With respect to the gas-phase theoretical UV spectrum, a notable reduction of 0.1 eV in the spacing between the two lowest energy spectral bands at 4.99 and 6.28 eV is seen in the solution-phase theoretical spectrum. As shown in Figure 3.14, the hypsochromic shifts and smaller spectral band spacing of the bands at 6.28 and 6.99 eV, brings the aqueous computed UV spectrum into better agreement with the experimental UV spectrum.

As the most accurate functional/basis set combination, B3LYP/LANL2DZ TDDFT output data were analysed to gain insight into the nature of the excited-state transitions occurring. These results have been tabulated in Table 3.17. The MO transitions occurring at 4.93, 6.26 and 7.28 eV were found to correspond to HOMO → LUMO, HOMO-2 → LUMO and HOMO-4 → LUMO+1, respectively. The MOs involved in these transitions are depicted in Figure 3.15.

Table 3.17: The assignment of the three lowest energy excited state transitions occurring in Adenine using B3LYP/LANL2DZ data.

Excitation Energy (eV)	Oscillator Strength (a.u.)	MO Transition	CI Coefficient (% contribution)	Assignment of Transition
4.93	0.1546	HOMO → LUMO	0.60878 (74.12)	$\pi \rightarrow \pi^*$
6.26	0.1971	HOMO-2 → LUMO	0.43317 (37.53)	$\pi \rightarrow \pi^*$
7.28	0.2355	HOMO-4 → LUMO+1	0.60774 (73.87)	$\pi \rightarrow \pi^*$

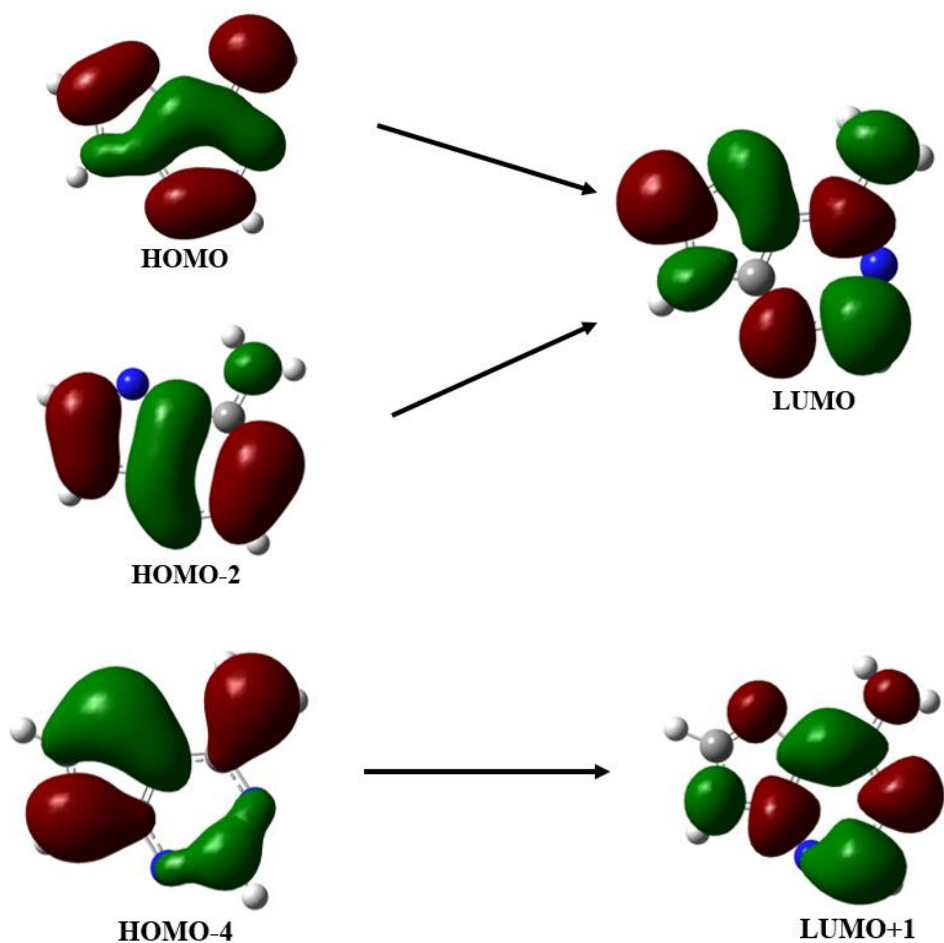


Figure 3.15: MOs involved in the electronic transitions of adenine. MOs were calculated at the B3LYP/LANL2DZ level of theory.

It should be noted that for the excitation occurring at 6.26 eV, HOMO-2 \rightarrow LUMO made a relatively small contribution (37.53%) to the transition. Although, this transition had the relatively largest CI coefficient (in comparison to the transitions occurring at that energy), it cannot be deemed the most dominant. The low CI coefficient of HOMO-2 \rightarrow LUMO suggests that other transitions contributed significantly to the excited state.

The present results have again been compared to those of Shukla et al. (TDDFT performed at 50 states using B3LYP/6-311++G(d,p)).⁸⁴ In their work, the first two transitions of adenine were described as being $\pi \rightarrow \pi^*$ in nature. Visualisation of the MOs using B3LYP/LANL2DZ put the calculated results in agreement with those of Shukla et al. Although thorough, their

work only detailed MO transitions up to ca. 6 eV for adenine. Therefore, no assignment is offered for the third band present at 7.26 eV. Again, the inspection of the MOs indicates that this third band is also $\pi \rightarrow \pi^*$ in nature.

3.3.3 I·Nu Complexes

3.3.3.a Iodide-Uracil

Initial ground-state geometry optimisation DFT calculations were performed on I·Ur calculations using a range of density functionals. Figure 3.16 displays a typical structure obtained at the B3LYP/LANL2DZ level of theory. The measured H···I distances (2.60 Å and 3.12 Å) were consistent with the parameters outlined previously by King et al.⁹⁸ Frequency calculations were also carried out alongside the geometry optimisation. The results contained no imaginary frequencies, therefore the cluster can be described a true minimum on the PES.

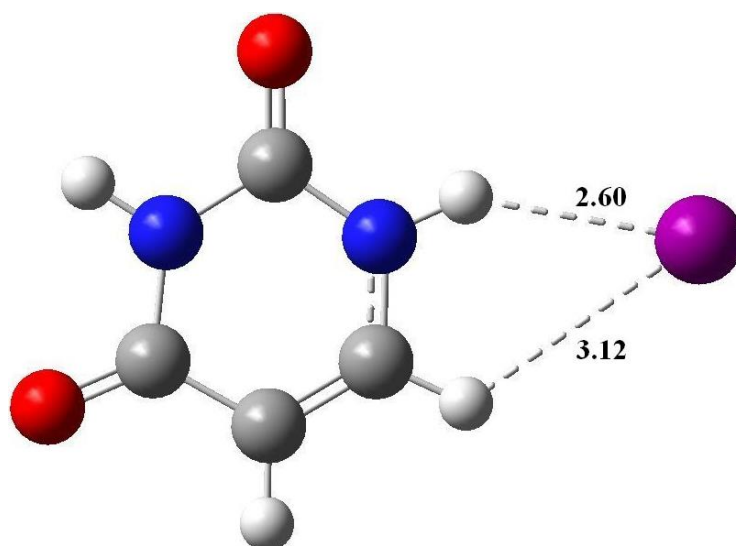


Figure 3.16: The B3LYP/LANL2DZ optimised ground-state structures of I·Ur. Hydrogen bonds are indicated with a dashed line with bond distances in Å.

TDDFT calculations were performed at 50 states in order to account for the all of the bands seen in the experimental spectra. As displayed in Table 3.18, the computational results generated from testing six different functionals were compared to the experimental, gas-phase data, and the resulting MAEs were calculated (Table 3.19).

Table 3.18: Computed and experimental excitation energies of I·Ur at 50 states, where **a**, **b**, **c** and **d** are the lowest energy spectral bands ^{a,b}

Functional	Excitation Energy (eV)			
	a	b	c	d
B3LYP	3.58	4.95	6.36	7.35
CAM-B3LYP	3.74	5.29	6.72	7.78
M062X	3.53	5.36	6.79	7.84
M11	4.54	5.38	6.90	7.76
MN12-SX	3.82	5.23	6.55	7.75
PBE0	4.07	5.14	6.55	7.54
Experimental ^b	4.03	4.84	-	-

^a TDDFT calculations were performed at 50 states.

^b Photodepletion (absorption) spectrum (unpublished work courtesy of Yoshikawa et al.).

Table 3.19: Mean absolute errors in excitation energy (eV) associated with TDDFT/LANL2DZ calculations of I·Ur at 50 states.

Functional	Mean Absolute Error (eV)
B3LYP	0.205
CAM-B3LYP	0.295
M062X	0.435
M11	0.625
MN12-SX	0.225
PBE0	0.290

The density functional MAEs displayed little deviation from the trend observed for the uncomplexed nucleobases. The accuracy of the functionals were determined as: B3LYP >

MN12-SX > CAM-B3LYP > PBE0 > M062X > M11. Although PBE0 predicted the energy of the first band most accurately, B3LYP still performs most accurately overall as it predicted the excitation energy for the second band most accurately. As this band was the most intense in the experimental data, its excitation energy was used as the principle performance criteria. Therefore, it was concluded that B3LYP/LANL2DZ gave the best performance and its data was used in the further analysis of the excited-state transitions. A very good agreement was found to exist between the B3LYP/LANL2DZ and photodepletion (absorption) spectra of I[•]Ur. This is shown in Figure 3.17.

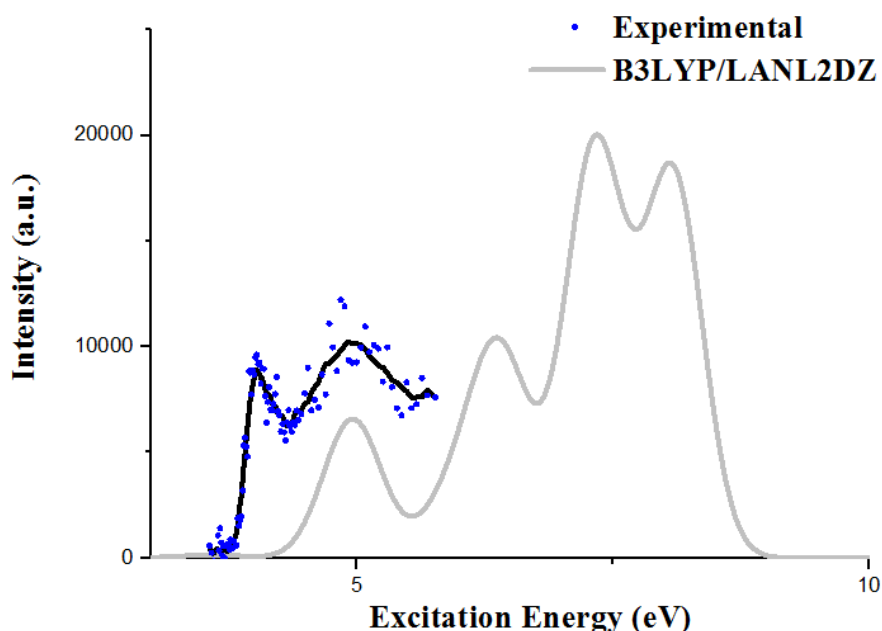


Figure 3.17: Comparison of the experimental and theoretical electronic spectra of I[•]Ur:
 • Experimental photodepletion (absorption) spectrum (unpublished work courtesy of Yoshikawa et al.),
 — Band profile for photodepletion (absorption) spectrum and
 — B3LYP/LANL2DZ (50 states).

It is fascinating to note in Figure 3.17 the very weak intensity of the lowest energy theoretical band (at 3.58 eV). No functional produced results in which this band had significant oscillator strength. At this excitation energy, a transition of electron density from iodide to a π^* orbital on uracil was witnessed involving the HOMO and LUMO+1 orbitals (Table 3.20 and Figure

3.18). The low oscillator strength of the first band could be attributed to the well-recognised failure of TDDFT to account for charge transfer transitions accurately.¹¹² As this deficiency is thought to stem from the incorrect long-range behaviour of the density functional's exchange potential, the long-range corrected CAM-B3LYP functional should have described the lowest energy band more accurately. However, the MAEs of CAM-B3LYP were much higher than that of B3LYP's. This suggests that the inaccurate description of the lowest energy band was not solely due to the density functional used.

Table 3.20: Assignment of the four lowest energy excited-state transitions of I⁻·uracil using B3LYP/LANL2DZ data.

Excitation Energy (eV)	Oscillator Strength (a.u.)	MO Transition	CI Coefficient (% contribution)	Assignment of Transition
3.58	0.0037	HOMO → LUMO+1	0.70679 (99.91)	I ⁻ → π*
4.96	0.1621	HOMO-3 → LUMO	0.66898 (89.51)	π → π*
6.34	0.1950	HOMO-3 → LUMO+1	0.59971 (71.93)	π → π*
7.30	0.3219	HOMO-5 → LUMO+1	0.59598 (71.04)	π → π*

The weak oscillator strength of the lowest energy band was most likely due to the nature of the excited-state transition occurring at that particular energy. From Figure 3.18, it is evident that the transition at 3.58 eV was of a charge transfer nature, however it was thought that the excitation was to a dipole bound excited state. In this dipole bound excited state, the excited electron is loosely bound to the nucleobase and occupies a diffuse orbital which is localised on the nucleobase.^{113,114} The relatively high dipole moment of uracil provides further evidence for the presence of a dipole bound excited state. Dipole-bound excited states typically require a dipole moment of 2.0 Debye or above and I⁻·uracil possesses a dipole moment of 3.95 Debye.^{114,115}

The failure of the TDDFT calculations to produce spectra in which the lowest energy band had a significant oscillator strength, stems from the basis set used. Calculations must take into account the diffuse nature of the orbital in which the excited electron resides. Consequently, a very diffuse basis set is often required in calculations involving dipole-bound excited states. Through further examination of the MOs involved in the electronic transitions of I⁻·uracil (Figure 3.18), the three higher energy transitions at 4.96, 6.34 and 7.30 eV were all confirmed as being $\pi \rightarrow \pi^*$ in nature.

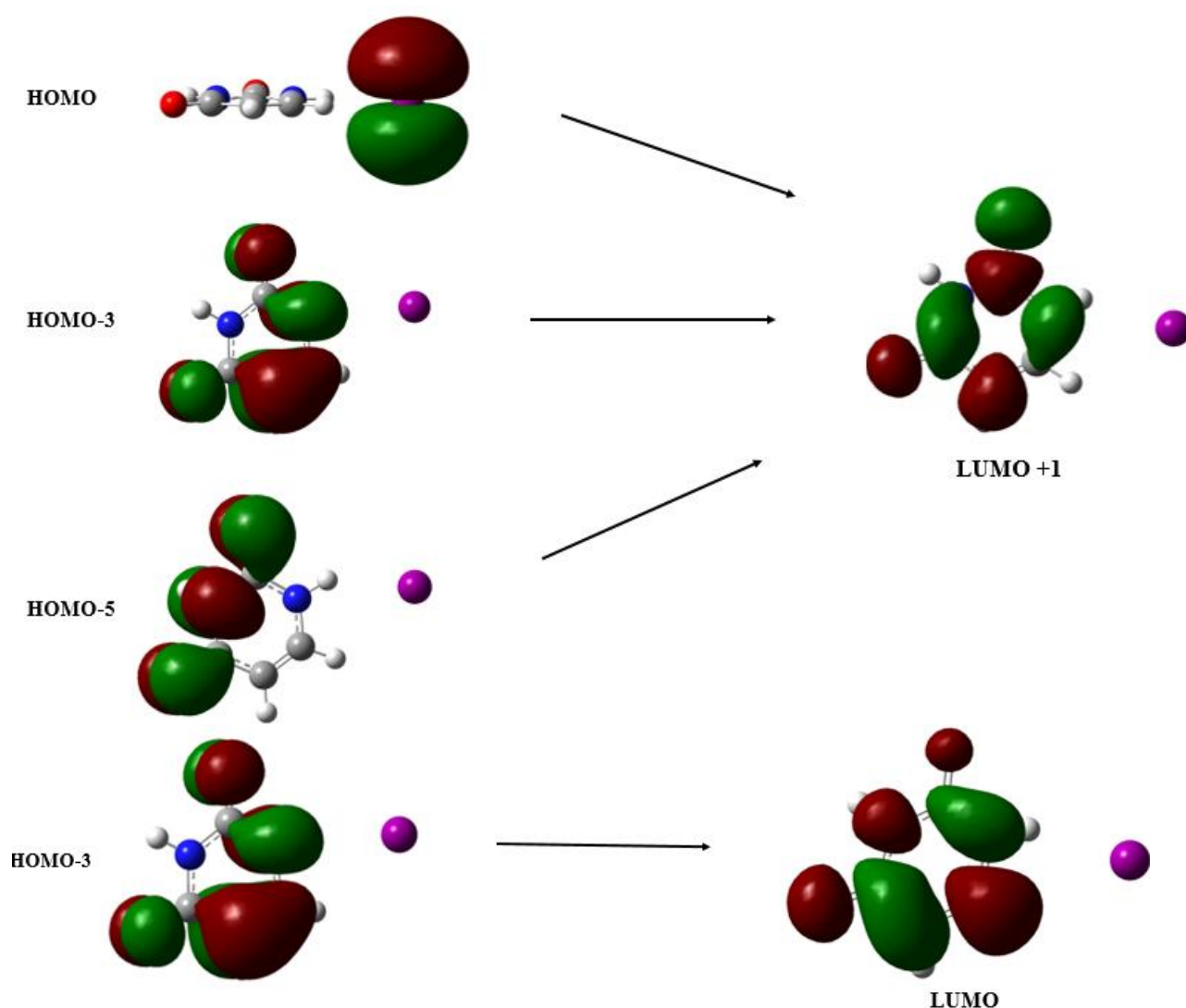


Figure 3.18: MOs involved in the electronic transitions of I⁻·uracil. MOs were calculated at the B3LYP/LANL2DZ level of theory.

3.3.3.b Iodide-Thymine

The geometry produced by the B3LYP/LANL2DZ optimisation can be seen in Figure 3.19. When compared to isolated thymine, slightly longer N \cdots H and C \cdots H bonds can be observed in this structure. It was thought that the presence of iodide was responsible for the elongation of these bonds by 0.03 and 0.01 Å, respectively. The calculated H \cdots I distances were 2.60 and 3.15 Å and in good agreement with literature values.⁹⁸ A large dipole moment of 5.61 Debye was calculated for this cluster.

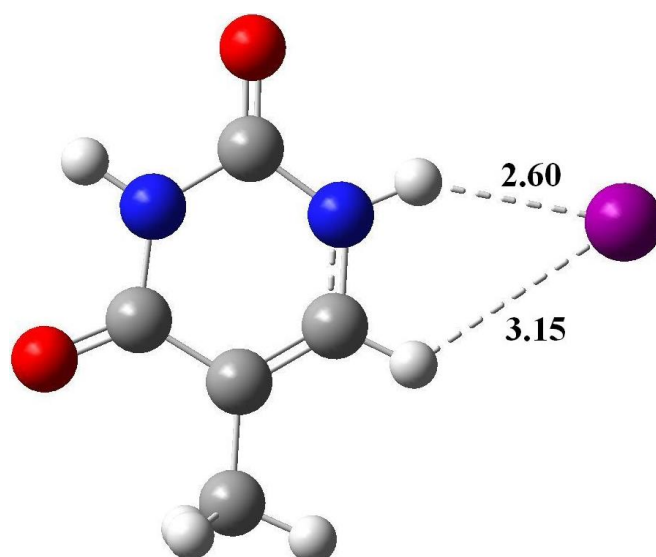


Figure 3.19: The B3LYP/LANL2DZ optimised ground-state structures of I \cdot thymine. Hydrogen bonds are indicated with a dashed line with bond distances in Å.

Using the previously optimised ground-state structures, TDDFT calculations were performed at 30 states for the six functionals listed in Table 3.21. All functionals produced spectra with four absorption bands at ca. 3.9, 5.1, 6.5 and 7.9 eV. From the calculated MAEs in Table 3.22, it is clear that the accuracy of the functionals observes the trend set by I \cdot uracil. The order of functional performance was determined as: B3LYP > MN12-SX > PBE0 > CAM-B3LYP > M062X > M11. The relatively small size of the MAEs indicates the overall good agreement between the experimental and calculated spectra.

Table 3.21: Computed and experimental excitation energies of I[•]-thymine at 30 states, where **a**, **b**, **c** and **d** are the lowest energy spectral bands. ^{a,b}

Functional	Excitation Energy (eV)			
	a	b	c	d
B3LYP	3.66	4.80	6.16	7.38
CAM-B3LYP	3.82	5.14	6.61	7.93
M062X	3.60	5.20	6.68	7.88
M11	4.54	5.24	6.78	8.68
MN12-SX	3.88	5.06	6.40	7.68
PBE0	4.14	4.97	6.34	7.61
Experimental ^b	3.90	4.63	-	-

^a TDDFT calculations were performed at 30 states.

^b Photodepletion (absorption) spectrum (unpublished work courtesy of Yoshikawa et al.).

Table 3.22: Mean absolute errors in excitation energy (eV) associated with TDDFT/LANL2DZ calculations of I[•]-thymine at 30 states.

Functional	Mean Absolute Error (eV)
B3LYP	0.103
CAM-B3LYP	0.148
M062X	0.218
M11	0.313
MN12-SX	0.113
PBE0	0.145

In similar fashion to I[•]-uracil, the lowest energy band on the calculated B3LYP/LANL2DZ spectra displays extremely low intensity (Figure 3.20). The oscillator strength of this transition is listed in Table 3.23 as 0.0036. As this transition was from iodide to a π^* state on thymine, the inaccuracy in oscillator strength can again be attributed to either the failure of TDDFT to account for charge transfer transitions or the basis set not being diffuse enough to describe the dipole-bound excited state on iodide.

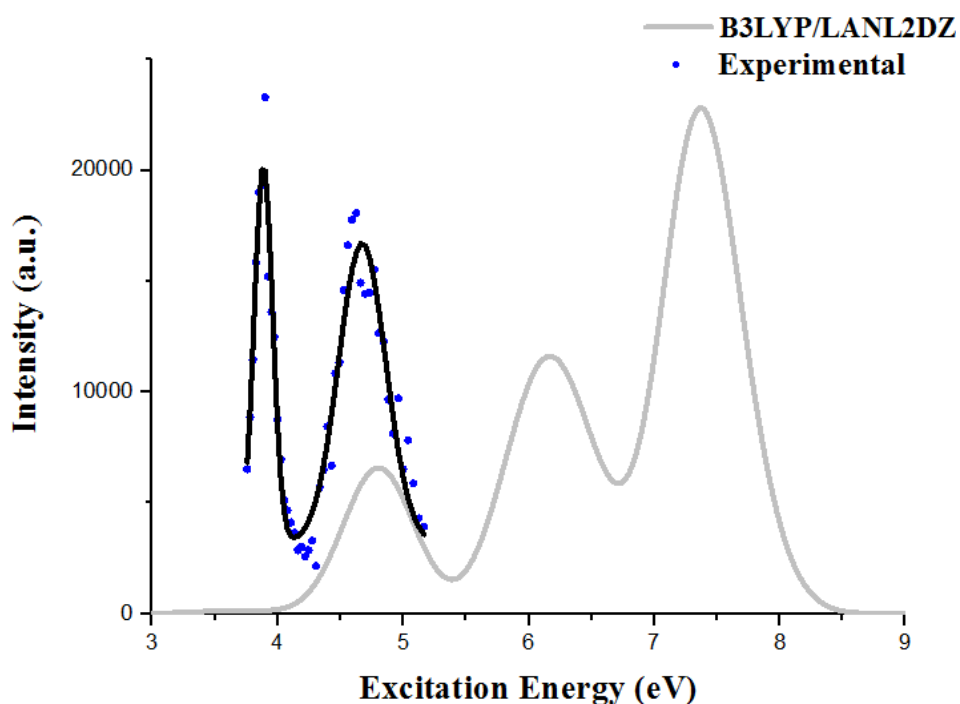


Figure 3.20: Comparison of the experimental and theoretical electronic spectra of I·Thy:
 • Experimental photodepletion (absorption) data (unpublished work courtesy of Yoshikawa et al.),
 — Band profile for the photodepletion (absorption) spectrum and — B3LYP/LANL2DZ (30 states).

Table 3.23: Assignment of the four lowest energy excited state transitions of I·Thymine using B3LYP/LANL2DZ data.

Excitation Energy (eV)	Oscillator Strength (a.u.)	MO Transition	CI Coefficient (% contribution)	Assignment of Transition
3.66	0.0036	HOMO → LUMO+1	0.70675 (99.90)	I → π*
4.80	0.1623	HOMO-3 → LUMO	0.67608 (91.42)	π → π*
6.21	0.1630	HOMO-3 → LUMO+1	0.52427 (54.98)	π → π*
7.33	0.4671	HOMO-5 → LUMO+1	0.64527 (83.27)	π → π*

Further inspection of the MOs in Figure 3.21 overleaf revealed that the three, higher energy bands at 4.80, 6.21 and 7.33 eV were dominated by transitions involving the nucleobase only. These transitions were all assigned as $\pi \rightarrow \pi^*$. Attention should be drawn to the low percentage contribution (54.98%) of the MOs involved in the transition at 6.21 eV. While the HOMO-3 \rightarrow LUMO+1 transition had the highest CI coefficient of all those listed, it is important to recognise that there would be a significant contribution from other MOs which give rise to the absorption band. For that reason it is with caution that the HOMO-3 \rightarrow LUMO+1 transition is described as dominant.

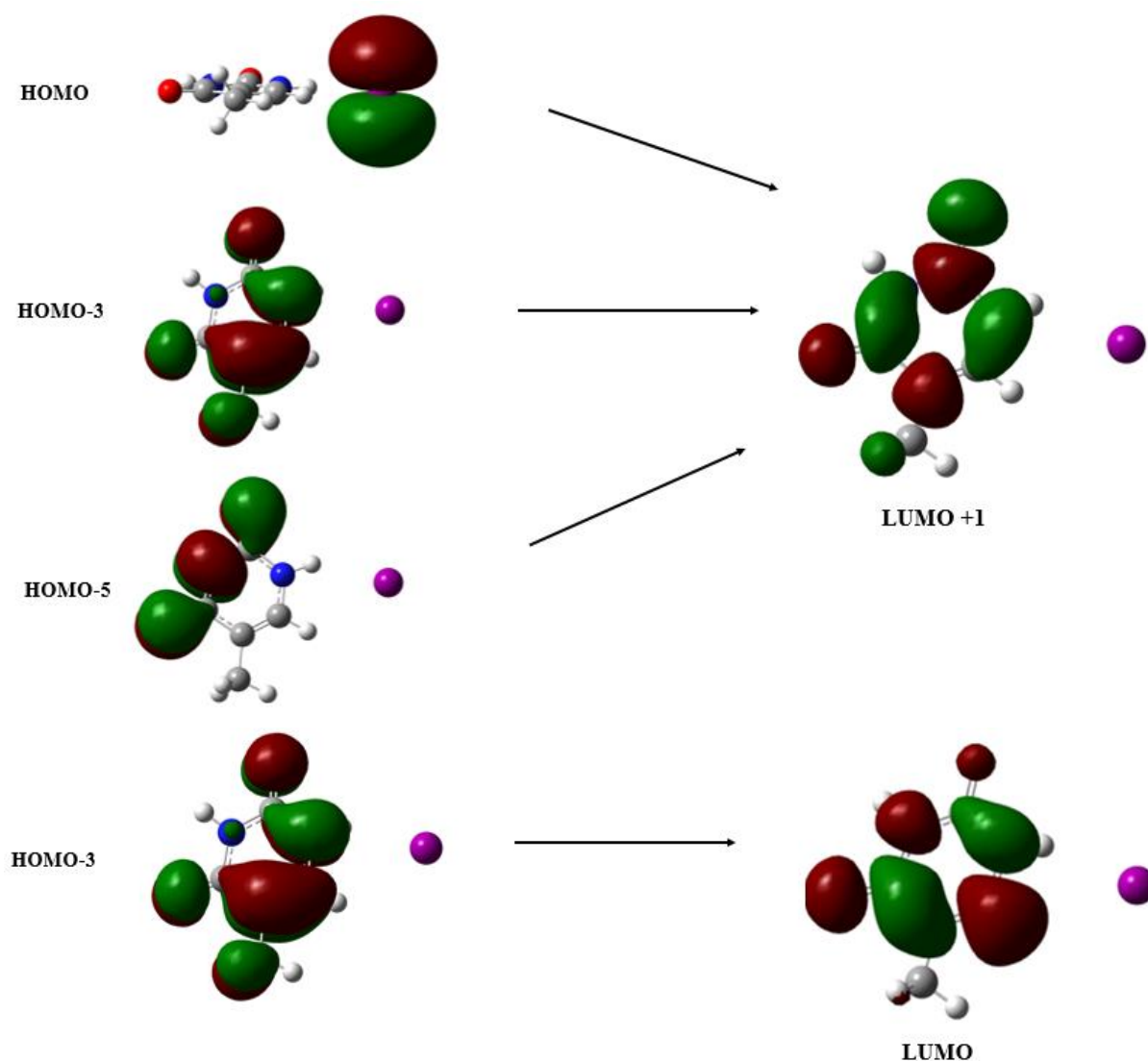


Figure 3.21: MOs involved in the electronic transitions of I·thymine. MOs were calculated at the B3LYP/LANL2DZ level of theory.

3.3.3.c Iodide-Adenine

A typical ground-state structure of I⁻·adenine produced by the DFT geometry optimisation calculations is depicted in Figure 3.22. Following DFT calculations, the resulting structure and ground-state properties were analysed. I⁻·adenine was found to have the largest dipole moment (9.32 Debye) of all the I⁻·Nu systems studied. A small increase in length (0.029 Å) can be observed for the N···H bond when compared to the corresponding isolated structure (Figure 3.1d). The H···I distances were calculated as 2.54 and 3.70 Å. These values are in reasonable agreement to those reported by Stephansen et al.¹¹⁶

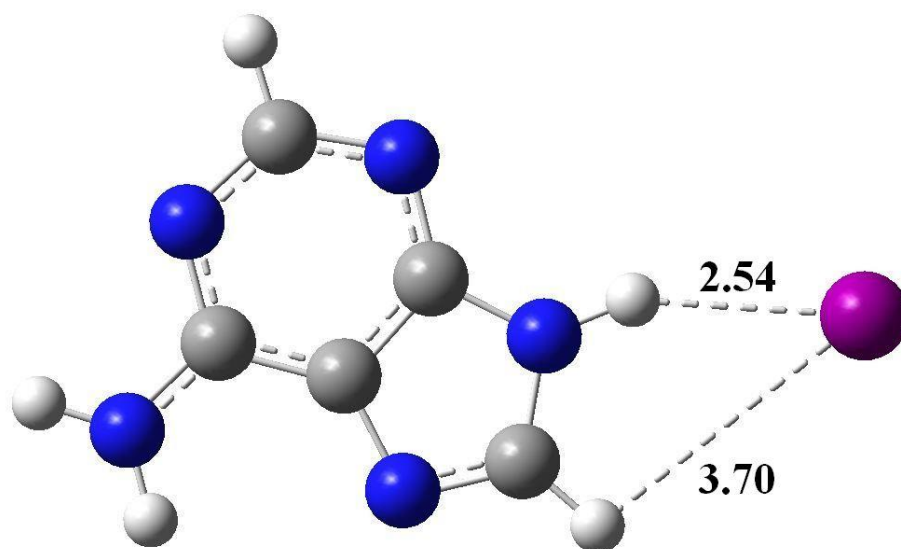


Figure 3.22: The B3LYP/LANL2DZ optimised ground-state structures of I⁻·adenine. Hydrogen bonds are indicated with a dashed line with bond distances in Å.

As there were no experimental data available for this system, MAEs could not be calculated and consequently the best performing functional could not be deduced. Nevertheless, the excitation energies produced by the various functionals are displayed in Table 3.24. Based on the high accuracy exhibited by B3LYP/LANL2DZ during the previous calculations of I⁻·Nu systems, its data were used in the assignment of the I⁻·adenine spectra.

Table 3.24: Computed excitation energies of I·adenine at 50 states using LANL2DZ, where **a**, **b** and **c** are the lowest energy spectral bands.

Functional	Excitation Energy (eV)		
	a	b	c
B3LYP	3.24	5.10	6.86
CAM-B3LYP	4.93	5.47	6.84
M062X	4.68	5.56	6.92
M11	5.00	5.64	6.92
MN12-SX	3.34	5.30	7.12
PBE0	3.70	5.28	7.10

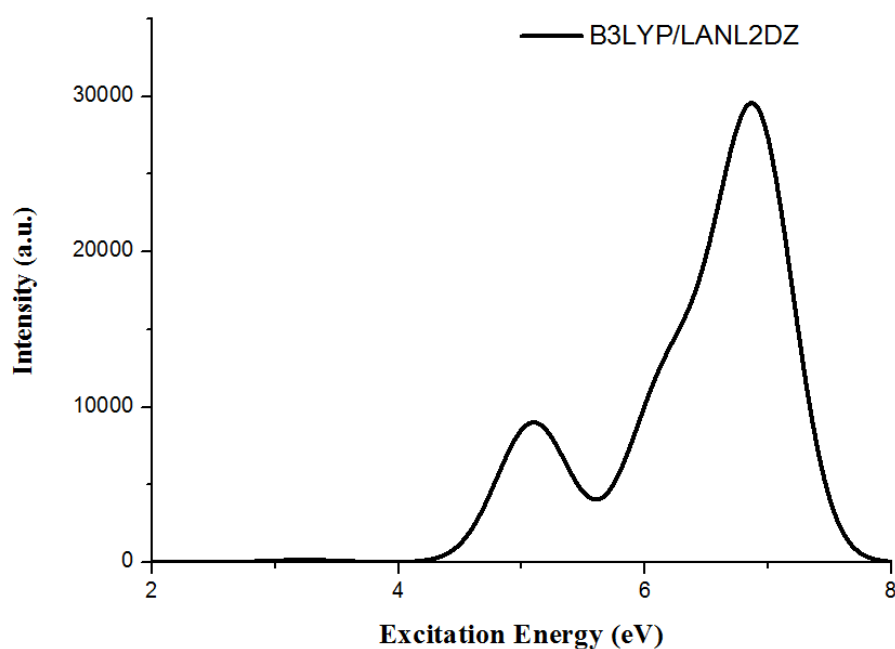


Figure 3.23: Computed UV spectrum of I·adenine, calculated at 50 states using B3LYP/LANL2DZ.

As observed for the other I·Nu complexes, the lowest energy band was found to be dominated by an excitation from iodide to a π^* state on adenine. The lowest energy band is again extremely weak in intensity with a relatively low oscillator strength of 0.004 a.u. (Figure 3.23). The subsequent three, higher energy bands were also found to be dominated by transitions that were thought to be $\pi \rightarrow \pi^*$ in nature. A summary of these assignments is given in Table 3.25. The MOs involved in the electronic transitions of I·adenine are displayed in Figure 3.24.

Table 3.25: The assignment of the three lowest energy excited-state transitions occurring in I·Adenine using B3LYP/LANL2DZ data.

Excitation Energy (eV)	Oscillator Strength (a.u.)	MO Transition	CI Coefficient (% contribution)	Assignment of Transition
3.24	0.0037	HOMO → LUMO+1	0.70665 (99.87)	I → π*(nucleobase)
5.04	0.1512	HOMO-3 → LUMO	0.57455 (66.02)	π → π*
6.08	0.1583	HOMO-5 → LUMO	0.47122 (44.41)	π → π*
6.91	0.4114	HOMO-5 → LUMO+1	0.56995 (64.97)	π → π*

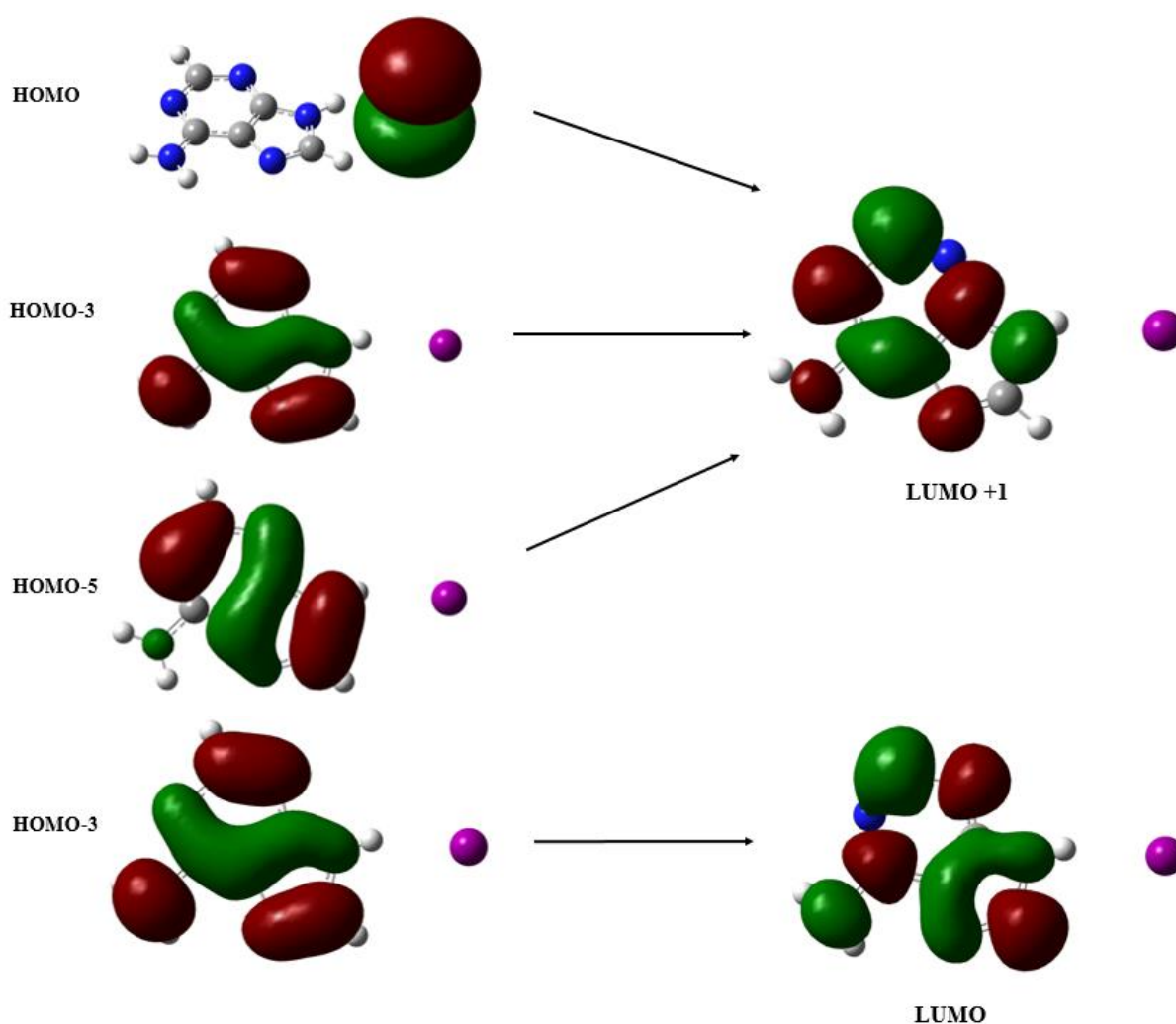


Figure 3.24: MOs involved in the electronic transitions of I·adenine. MOs were calculated at the B3LYP/LANL2DZ level of theory.

3.4 Conclusion

TDDFT calculations were performed on $I\cdot Nu$ complexes, where Nu = uracil, thymine and adenine, and their constituent “monomer” parts (i.e. the isolated iodide ion and isolated nucleobase monomer). Excited-state calculations produced UV absorption spectra from which the nature of the electronic transitions were assigned.

The electronic transitions of uracil, cytosine, adenine and thymine were very similar in nature and were revealed to be mostly of $\pi\pi^*$ character. Assignments made for the electronic spectra of the nucleobases were in agreement with those found in literature. TDDFT calculations of the isolated iodide ion produced UV spectra in which no bands were present. The absence of spectral bands was attributed to the lack of stable excited states for iodide.

Strong similarities were also observed in the electronic spectra of the $I\cdot Nu$ complexes studied. The higher energy spectral bands were all found to correspond to $\pi\rightarrow\pi^*$ transitions. Although the position of the lowest energy spectral bands were well described by B3LYP/LANL2DZ, calculations at this level of theory failed to accurately reproduce the intensity of these band, as seen in the experimental spectra. No functional/basis set combination produced spectra in which the lowest energy band had a significant oscillator strength. This failure was attributed to the nature of the electronic transition occurring at the first band. In all $I\cdot Nu$ spectra, the lowest energy spectral band corresponded to a charge transfer excitation to a dipole-bound excited state. To account for this transition, a more diffuse basis set must be used.

In a recent study by King et al., the aug-cc-pVDZ-PP basis set with several added sets of sp diffuse functions was used to investigate the difference in electron density for $I\cdot$ thymine and $I\cdot$ uracil following electronic excitation.^{99,117} Another study by this group employed the 6-

311++G(d,p) basis set with five additional sets of sp diffuse functions to investigate the photodynamics of dipole bound Γ -adenine clusters.¹¹⁶

Overall, B3LYP/LANL2DZ was found to be the best performing functional/basis set combination in terms of the prediction of the experimental excitation energies. The superior performance of B3LYP was attributed to its relatively smaller exact exchange component. Of the Γ -Nu and isolated nucleobases studied, M062X and M11 were deemed the worst performing functionals. M062X and M11 tended to grossly overpredict the experimental energies and provided a poor balance between computational time and accuracy.

The inclusion of a solvent in TDDFT calculations was found to increase the accuracy of the theoretical excitation energies. The significant solvent shifts observed in the B3LYP/LANL2DZ solution spectra brought the calculated UV spectra into further good agreement with the aqueous experimental spectra.

Chapter 4

A TDDFT Computational Study of Platinum (II)

Complexes Bound to Water

4.1 Introduction

As discussed in Chapter 3, gas-phase UV spectra of various $\text{Pt}(\text{CN})_n^{2-}\cdot\text{Nu}$ complexes have been obtained using laser spectroscopy and initial assignments of their excited-state transitions have been made.⁴³ A theoretical investigation of these systems is necessary to confirm the preliminary assignments. As a precursor to this, the UV electronic transitions of $\text{Pt}(\text{CN})_4^{2-}\cdot\text{H}_2\text{O}$ complexes will be explored in this chapter. This study aims to investigate the evolution of the transitions of bare $\text{Pt}(\text{CN})_4^{2-}$ into a complex with a solvent molecule that lacks a near-UV chromophore.

Although research into platinum complexes bound to water is limited, platinum (II) complexes are studied frequently due to their relationship to the anticancer drug cisplatin.^{86,118,119} Wang et al. have previously employed experimental and theoretical methods to study the electronic structures and stabilities of $\text{Pt}(\text{CN})_4^{2-}$ and $\text{Pt}(\text{CN})_6^{2-}$ in the gas phase. Photodetachment photoelectron spectroscopy was used to measure the adiabatic electron binding energies, vertical detachment energies and repulsive Coulomb barriers. Density functional theory (DFT) calculations were performed at the B3LYP and PW91 levels of

theory to confirm the geometries of the dianions and to aid interpretation of the experimental results.^{58,120-121}

Wang and Ziegler have also investigated the electronic properties of platinum (II) complexes using theoretical methods. Having devised a two-component relativistic time-dependent density functional theory (TDDFT) formalism, $\text{Pt}(\text{CN})_4^{2-}$, PtCl_4^{2-} and PtBr_4^{2-} were used to assess its performance.¹²² The electronic spectra and subsequent excitation energies of these complexes were calculated and compared to experimental data obtained using single crystal absorption spectroscopy.¹²³

The structure and stability of microsolvated $\text{Pt}(\text{CN})_4^{2-}$ clusters have been investigated by Milner et al. in a joint experimental and theoretical study. Resonance excitation collision induced dissociation was used to determine the stabilities and fragmentation pathways of the following clusters: $\text{Pt}(\text{CN})_4^{2-}(\text{H}_2\text{O})_n$ where $n = 1-4$, $\text{Pt}(\text{CN})_4^{2-}(\text{MeCN})_m$ where $m = 1,2$ and $\text{Pt}(\text{CN})_4^{2-}(\text{H}_2\text{O})_3\cdot\text{MeCN}$. The lowest energy structural isomers of $\text{Pt}(\text{CN})_4^{2-}(\text{H}_2\text{O})_4$ were identified using DFT at the B3LYP/LACVP+* level of theory.¹²⁴

In this chapter, TDDFT will be used to calculate the electronic spectra of the following complexes: $\text{Pt}(\text{CN})_4^{2-}$, $\text{Pt}(\text{CN})_6^{2-}$ and $\text{Pt}(\text{CN})_4^{2-}\cdot\text{H}_2\text{O}$. In order to investigate their effects on the excitation energies, the calculations will employ a range of hybrid functionals. This study will also probe the performance of several pseudopotentials for the prediction of electronic spectra.

4.2 Computational Details

DFT geometry optimisations and frequency calculations were performed on $\text{Pt}(\text{CN})_4^{2-}\cdot\text{H}_2\text{O}$, $\text{Pt}(\text{CN})_4^{2-}$ and $\text{Pt}(\text{CN})_6^{2-}$ at the following levels of theory: B3LYP, CAM-B3LYP, M062X, M11, MN12-SX and PBE0.^{58-61, 64-65} Using their previously optimised structures, TDDFT calculations were then performed on $\text{Pt}(\text{CN})_4^{2-}\cdot\text{H}_2\text{O}$, $\text{Pt}(\text{CN})_4^{2-}$ and $\text{Pt}(\text{CN})_6^{2-}$ at the respective

levels of theory. All calculations were carried out using the Gaussian 09 (G09) package, version D.01.⁹⁵

To probe its effects, the basis set employed in the calculations on $\text{Pt}(\text{CN})_4^{2-}$ was also varied. Either Def2-TZVPP or SDD pseudopotentials were used to describe the core platinum electrons, while LANL2DZ was employed in conjunction to define the valence electrons (C and N) in $\text{Pt}(\text{CN})_4^{2-}$. The effect of using LANL2DZ as pseudopotential on Pt was also explored. In this combination, 6-311++G(2d,2p) was used on C and N. In addition to these pseudopotential combinations, the LANL2DZ basis set was also tested.

The effect of solvation on the excitation energies of isolated $\text{Pt}(\text{CN})_4^{2-}$ was investigated using IEFPCM, the default version of PCM in G09. TDDFT calculations were performed at the MN12-SX/LANL2DZ level of theory and methanol was used as the solvent. The solvent chosen was the same as that used in a study by Sen et al.,⁴¹ from which the aqueous experimental spectra of $\text{Pt}(\text{CN})_4^{2-}$ and $\text{Pt}(\text{CN})_6^{2-}$ have been obtained.⁴³

4.3 Results and Discussion

4.3.1 Platinum (II) Tetracyanide

DFT ground state geometry optimisations were performed on $\text{Pt}(\text{CN})_4^{2-}$ using a range of functional/basis set combinations. The resulting D_{4h} square-planar optimised ground-state structure was found to have average Pt...C and C...N bond lengths of 2.01 and 1.19 Å, respectively.

Using their respective optimised structures, TDDFT calculations were performed at 10, 20 and 30 states. When employing CAM-B3LYP, M062X and M11, 20 states was sufficient to reproduce the two absorption bands alluded to in the experimental spectra (Figure 4.1).

However, TDDFT calculations had to be performed at 30 states when using the B3LYP, MN12-SX and PBE0 functionals.

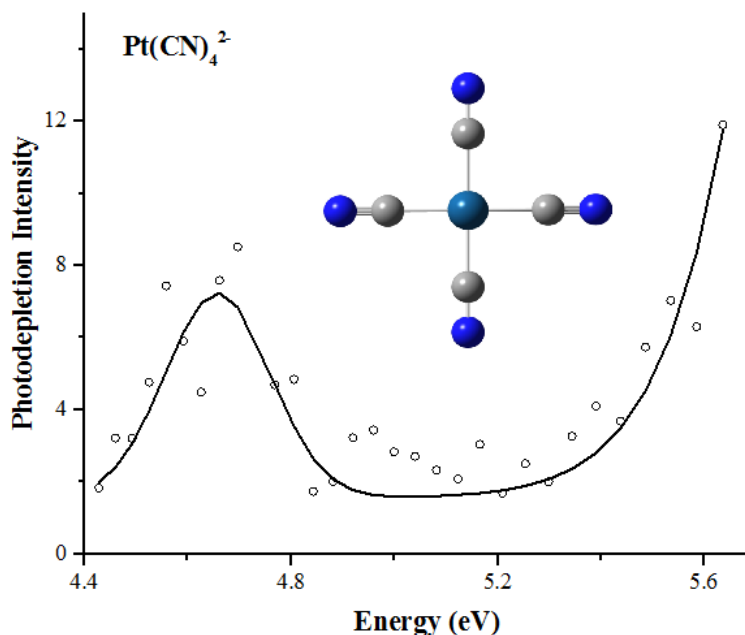


Figure 4.1: Experimental gas-phase photodepletion (absorption) spectrum of $\text{Pt}(\text{CN})_4^{2-}$. (Courtesy of Sen et al.)⁴³

As outlined in chapter 3, LANL2DZ was proven to be the best performing basis set for predicting the excitation energies of several nucleobases with the range of functionals studied for uracil, cytosine, thymine and adenine. In order to see if that conclusion was still relevant for the platinum-based complexes studied in this chapter, the basis set used in this study was also varied. With the exception of 6-311++G(2d,2p), the basis sets studied in the previous chapter (LANL2DZ and Def2-TZVPP) were employed as pseudopotentials on Pt. The SDD pseudopotential and LANL2DZ basis set was also tested. A comparison of the subsequent computational and experimental energies is provided in Table 4.1.

Table 4.1: Comparison between the theoretical excitation energies obtained using TDDFT at 30 states and the experimental, gas phase results (in eV) of $\text{Pt}(\text{CN})_4^{2-}$; where **a** and **b** are the lowest energy spectral bands.

	DEF2-TZVPP (ECP) ^a		LANL2DZ		SDD (ECP) ^a		LANL2DZ (ECP) ^b	
	a	b	a	b	a	b	a	b
B3LYP	5.21	8.07	5.16	6.79	5.05	6.48	5.12	6.23
CAM-B3LYP	5.47	8.89	5.48	7.30	5.37	7.09	5.41	6.78
M062X	5.74	8.96	5.70	7.36	5.66	7.14	5.58	6.70
M11	5.72	9.30	5.68	6.89	5.58	6.88	5.48	6.50
MN12-SX	5.26	7.27	4.38	5.80	5.19	5.79	4.15	5.63
PBE0	5.37	8.46	5.33	7.08	5.24	6.72	5.28	6.40
Experimental ^c	4.70	-	4.70	-	4.70	-	4.70	-

^a ECPs were used solely on Pt, while LANL2DZ was used for C and N.

^b ECP was used on Pt only, while 6-311++G(2d,2p) was used for C and N.

^c Ref [43]

Table 4.2: The mean absolute errors in excitation energy (eV) of $\text{Pt}(\text{CN})_4^{2-}$.

Functional	Def2-TZVPP (ECP) ^a	LANL2DZ	SDD (ECP) ^a	LANL2DZ (ECP) ^b
B3LYP	0.51	0.46	0.35	0.42
CAM-B3LYP	0.77	0.78	0.67	0.71
M062X	1.04	1.00	0.96	0.88
M11	1.02	0.98	0.88	0.78
MN12-SX	0.56	0.32	0.49	0.55
PBE0	0.67	0.63	0.54	0.58

^a ECPs were used solely on Pt, while LANL2DZ was used for C and N.

^b ECP was used on Pt only, while 6-311++G(2d,2p) was used for C and N.

The MAEs calculated in Table 4.2 show clearly the variation in functional/basis set combinations. With a relatively small error of 0.32 eV, MN12-SX/LANL2DZ produced the most accurate results in terms of predicting the experimental excitation energies. This was followed closely by the B3LYP/SDD (ECP) combination which had an error of 0.35 eV.

Comparisons between these two functionals showed that when the basis set was varied, B3LYP consistently outperformed MN12-SX, (with the exception of LANL2DZ).

M062X and M11 proved to be the worst performing functionals, displaying the highest MAEs. Calculations at these levels of theory led to a significant over prediction of the excitation energies. It has been suggested by Zhao et al. and Peverati et al. that a higher accuracy can be achieved when using the long-range versions of these functionals. Their studies deduced that the M06-L and M11-L functionals (which contain no Hartree Fock exchange), were better suited for treating systems containing transition metals.^{125,126}

Calculations using PBE0 and CAM-B3LYP also resulted in an overestimation of the excitation energies. Consequently, these functionals were deemed unsuitable for the platinum (II) systems under consideration. The performance of the functionals tested can be summarised as follows, in the order of decreasing performance: MN12-SX > B3LYP > PBE0 > CAM-B3LYP > M11 > M062X.

The SDD pseudopotential basis set produced the lowest errors overall, giving a highly accurate prediction of the first experimental band (Table 4.2). As expected, this pseudopotential also provided a relatively low computational time. This apparently high accuracy and reasonable CPU time cost makes SDD (ECP) an attractive choice. However, examination of the computed UV spectrum revealed that the pseudopotential tended to largely overestimate the position of the second experimental band. This is depicted in Figure 4.2, in which the computational UV spectra produced by B3LYP/SDD (ECP) and PBE0/SDD (ECP) are compared to the experimental spectrum.

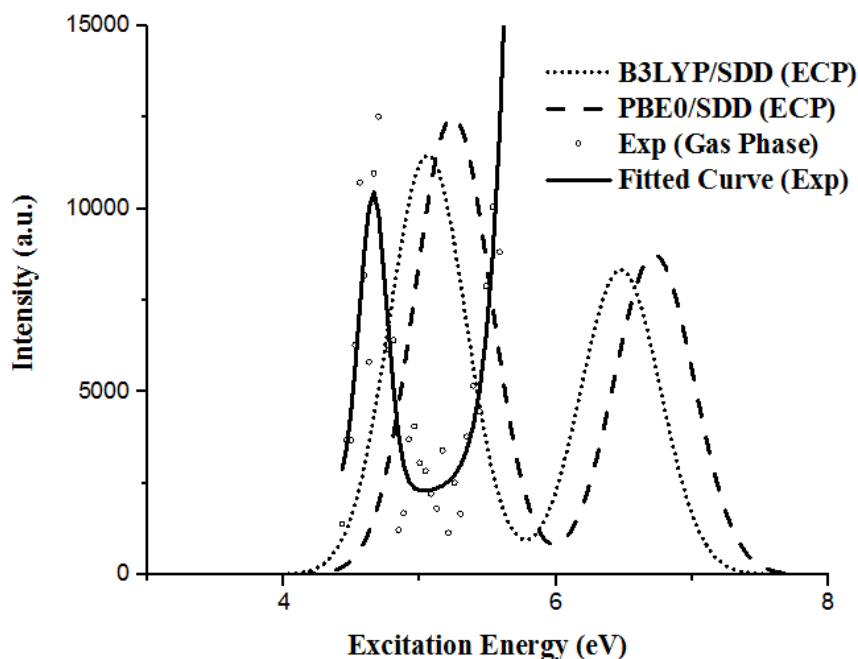


Figure 4.2: Comparison of the experimental and theoretical electronic spectra of $\text{Pt}(\text{CN})_4^{2-}$:
 \circ Experimental photodepletion (absorption) spectrum (courtesy of Sen et al.),⁴³ **—**
 Band profile for photodepletion spectrum **.....**B3LYP/SDD (ECP) and **- - - -**
 PBE0/SDD (ECP).

The inability of SDD (ECP) to replicate the pattern in the oscillator strengths of the experimental bands can also be seen in Figure 4.2 above. Due to these reasons of accuracy, LANL2DZ (specifically when used in conjunction with MN12-SX) was viewed as the better performing basis set.

Interestingly, use of the SDD pseudopotential with MN12-SX did not produce the relatively poorer performance displayed by other functionals. As can be seen in Figure 4.3, calculations employing MN12-SX/SDD (ECP) on $\text{Pt}(\text{CN})_4^{2-}$ produced UV spectra which accurately predicted the excitation energy of the higher energy band. It also predicts the higher energy band as the most intense spectral band over this region, therefore successfully replicating the pattern in oscillator strength seen in the experimental spectrum. In these respects, MN12-SX/SDD (ECP) performs comparably to MN12-SX/LANL2DZ. However, MN12-SX/SDD (ECP) grossly overestimated the position of the lowest energy band and did not represent the difference in intensity between the two spectral bands accurately.

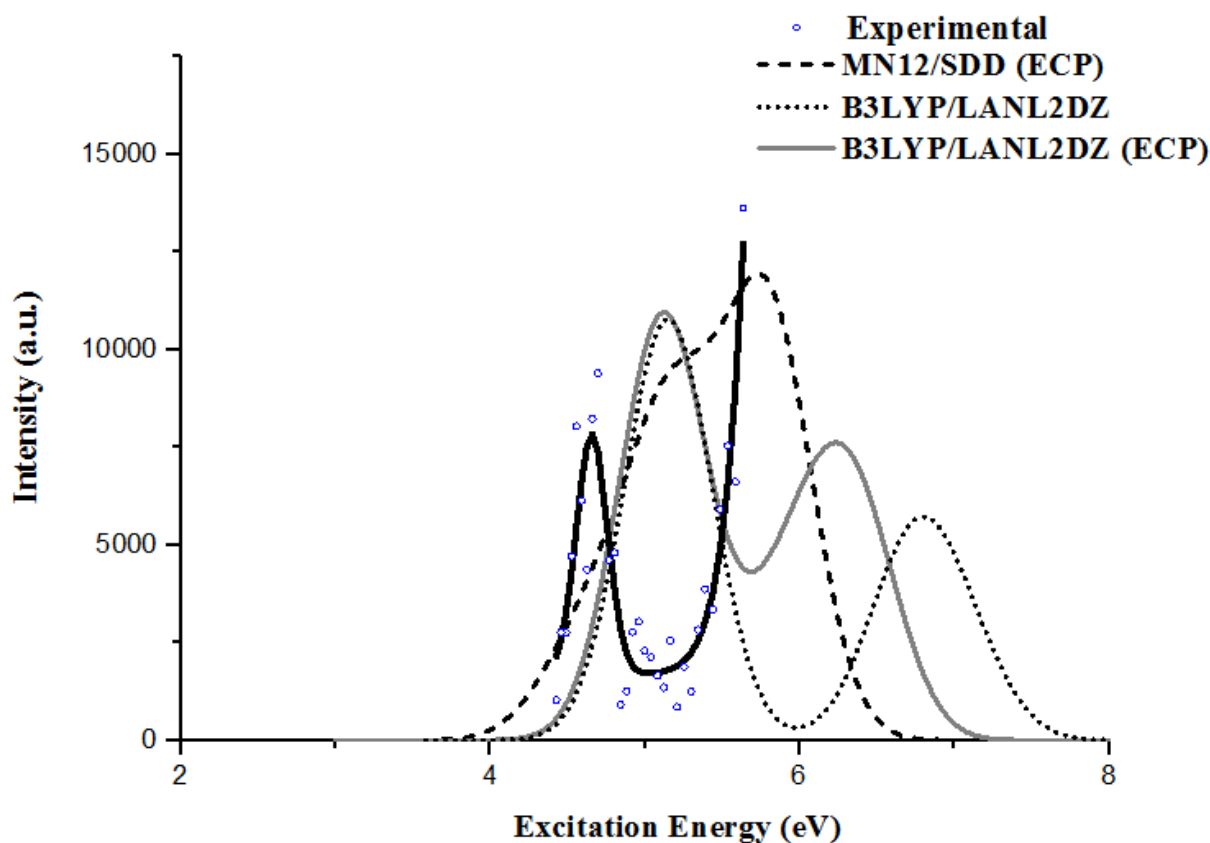


Figure 4.3: Comparison of the experimental and theoretical electronic spectra of $\text{Pt}(\text{CN})_4^{2-}$:
 ◦ Experimental photodepletion (absorption) spectrum (courtesy of Sen et al.),⁴³ — Band profile for photodepletion spectrum, - - - MN12-SX/SDD (ECP), B3LYP/LANL2DZ (ECP) and — B3LYP/SDD (ECP).

When compared to LANL2DZ, use of LANL2DZ (ECP) on Pt in conjunction with 6-311++G(2d,2p) (on C and N) resulted in a modest increase in accuracy for the prediction of the lowest energy band in the experimental UV spectrum of $\text{Pt}(\text{CN})_4^{2-}$ (Figure 4.3). Consequently, the MAEs associated with calculations employing LANL2DZ (ECP) were generally lower than those of LANL2DZ.

Although LANL2DZ (ECP) produced UV spectra that were quantitatively more accurate than the LANL2DZ basis set, LANL2DZ (ECP) gave a poorer qualitative reproduction of the experimental UV spectrum of $\text{Pt}(\text{CN})_4^{2-}$. With exception of MN12-SX/LANL2DZ (ECP), LANL2DZ (ECP) produced UV spectra in which the lowest energy band was more intense than the highest. As shown in Figure 4.3, the pattern in the intensity of the spectral bands

within LANL2DZ (ECP) spectra is in contrast with that seen in the experimental UV spectrum. With respect to LANL2DZ, a notable increase in the computational time of calculations employing the LANL2DZ (ECP) was also observed. The computational time associated with running a TDDFT calculation using LANL2DZ (ECP) at 30 states was on average 33 minutes longer than that of the LANL2DZ basis set.

Similar to the trend observed previously with the nucleobases, Def2-TZVPP (ECP) had the highest errors associated with its results, indicating a poor level of accuracy. Analysis of the computational spectra (Figure 4.4) showed that the use of this basis set led to an overestimation in the excitation energy of both spectral bands. Figure 4.4 depicts an extreme case in which M11/Def2-TZVPP predicted the energy of the second band as 9.30 eV. The expected value of this band was approximately 6 eV.

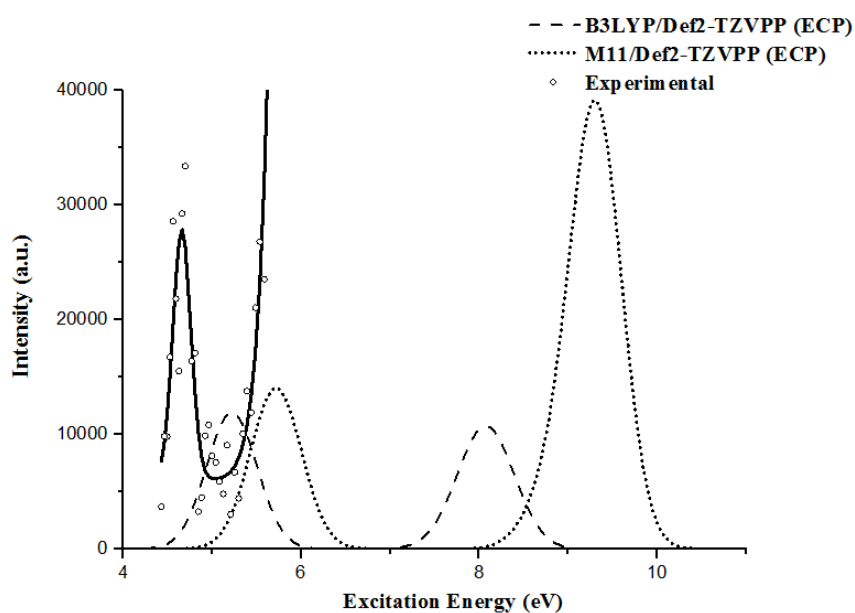


Figure 4.4: Comparison of the theoretical and experimental electronic spectra of $\text{Pt}(\text{CN})_4^{2-}$: \diamond Experimental photodepletion spectrum (courtesy of Sen et al.),⁴³ **—** Band profile for photodepletion spectrum, **.....** M11/Def2-TZVPP (ECP) and **- - -** B3LYP/Def2-TZVPP (ECP).

The computational time associated with running the Def2-TZVPP (ECP) calculations made the use of this basis set impractical for studying the electronic states of $\text{Pt}(\text{CN})_4^{2-}$.

Calculations at this level ranged in duration between 1 and 3.5 hours. This is significantly longer than the length of time taken to compute calculations involving LANL2DZ, of which the average time was 11 minutes. The poor balance between computational time and accuracy exhibited by Def2-TZVPP (ECP), when employed in the TDDFT calculations of the isolated $\text{Pt}(\text{CN})_4^{2-}$ monomer, makes the use of this pseudopotential basis set unsuitable in the study of the larger $\text{Pt}(\text{CN})_4^{2-}\cdot\text{M}$ complexes.

Using the MOs generated at MN12-SX/LANL2DZ level (Figure 4.5), assignments of the transitions were made (Table 4.3). The spectral bands at 4.38 and 5.8 eV represented transitions from the A_{1g} ground state to A_{2u} and E_u excited states, respectively. At 5.8 eV, the dominant excitations were discovered to have originated from a pair of degenerate orbitals, HOMO-1 and HOMO-2. These assignments were compared to literature to confirm their accuracy.¹²⁷

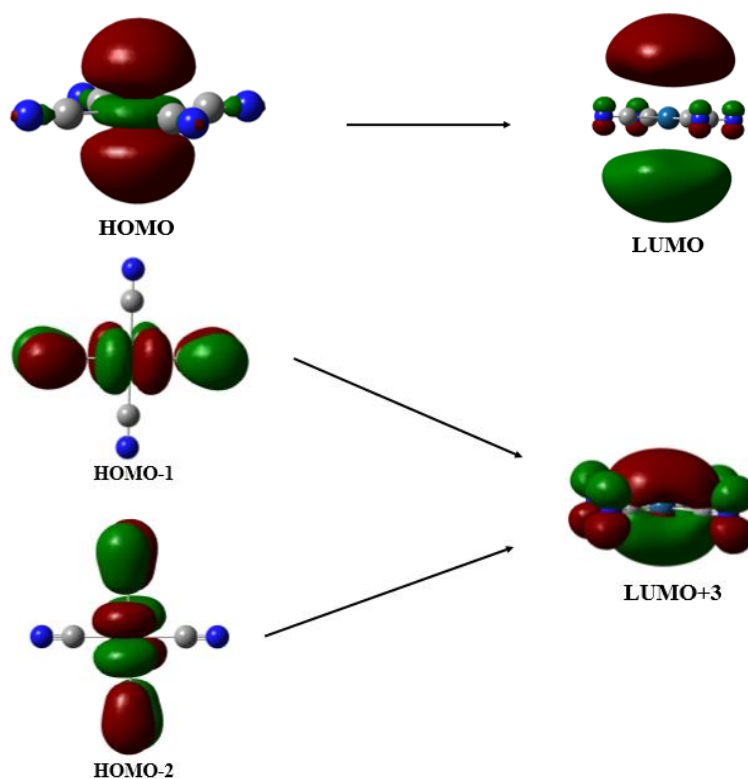


Figure 4.5: MOs involved in the electronic transitions of $\text{Pt}(\text{CN})_4^{2-}$. MOs have been calculated at the MN12-SX /LANL2DZ level of theory.

Table 4.3: Assignment of the vertical excitations of $\text{Pt}(\text{CN})_4^{2-}$ using MN12-SX/LANL2DZ data.

Excitation Energy (eV)	Oscillator Strength (a.u.)	MO Transition	CI Coefficient (% contribution)	Assignment of Transition
4.38	0.0648	HOMO \rightarrow LUMO	0.70148 (98.41)	$A_{1g} \rightarrow A_{2u}$
5.80	0.1273	HOMO-1 \rightarrow LUMO+3 HOMO-2 \rightarrow LUMO+3	0.68452 (93.71)	$A_{1g} \rightarrow A_{2u}$

An aqueous UV spectrum of $\text{Pt}(\text{CN})_4^{2-}$ has been obtained experimentally by Sen et al. in addition to a photodepletion (absorption) spectrum of $\text{Pt}(\text{CN})_4^{2-}$. A comparison of the gas-phase photodepletion and aqueous experimental UV spectra $\text{Pt}(\text{CN})_4^{2-}$ is presented in Figure 4.6. A bathochromic shift of 0.17 eV is seen for the lowest energy band in the aqueous UV spectrum of $\text{Pt}(\text{CN})_4^{2-}$. The aqueous spectrum of $\text{Pt}(\text{CN})_4^{2-}$ contains an additional spectral band of relatively weak intensity at 5.17 eV. Although the spectral band is not included in the band profile of the gas phase absorption spectrum (denoted by a solid black line in Figure 4.6), it is present in the photodepletion (absorption) spectrum of $\text{Pt}(\text{CN})_4^{2-}$ also at 5.17 eV.

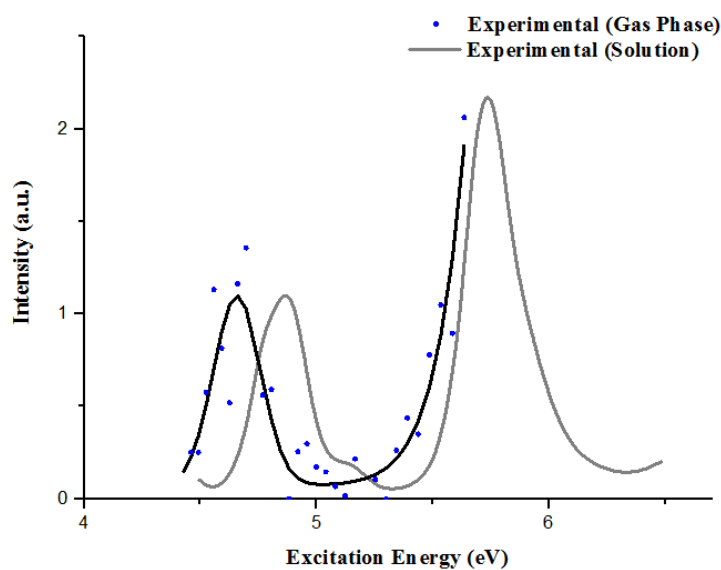


Figure 4.6: Comparison of the solution and gas phase experimental UV spectra of $\text{Pt}(\text{CN})_4^{2-}$: — Aqueous absorption spectrum and • Photodepletion (absorption) spectrum. The solid black line is a tentative band profile for the photodepletion spectrum.

The aqueous absorption spectrum of $\text{Pt}(\text{CN})_4^{2-}$ was computed using IEFPCM/TDDFT and MeOH was used as the solvent (Figure 4.6). The first 30 electronic states of $\text{Pt}(\text{CN})_4^{2-}$ were calculated at the MN12-SX/LANL2DZ level of theory. The excitation energies of $\text{Pt}(\text{CN})_4^{2-}$ produced by IEFPCM/TD-MN12-SX/LANL2DZ are listed in Table 4.4 below. The computed UV spectrum of $\text{Pt}(\text{CN})_4^{2-}$ is presented in Figure 4.7, where it has been compared with the gas phase MN12-SX/LANL2DZ and aqueous experimental UV spectra of $\text{Pt}(\text{CN})_4^{2-}$.

Table 4.4: Comparison of the experimental and computed excitation energies of $\text{Pt}(\text{CN})_4^{2-}$ (in vacuo and solution), where **a** and **b** are the lowest energy spectral bands.^{a-c}

	Excitation Energy (eV)	
	a	b
Vacuum ^a	4.38	5.80
Solution ^b	4.99	6.14
Experimental (gas phase) ^c	4.66	-
Experimental (solution) ^c	4.87	5.73

^a TD-B3LYP/LANL2DZ calculation performed at 20 states

^b TDDFT calculation performed at IEFPCM/B3LYP/LANL2DZ level (20 states)

^c Ref [43]

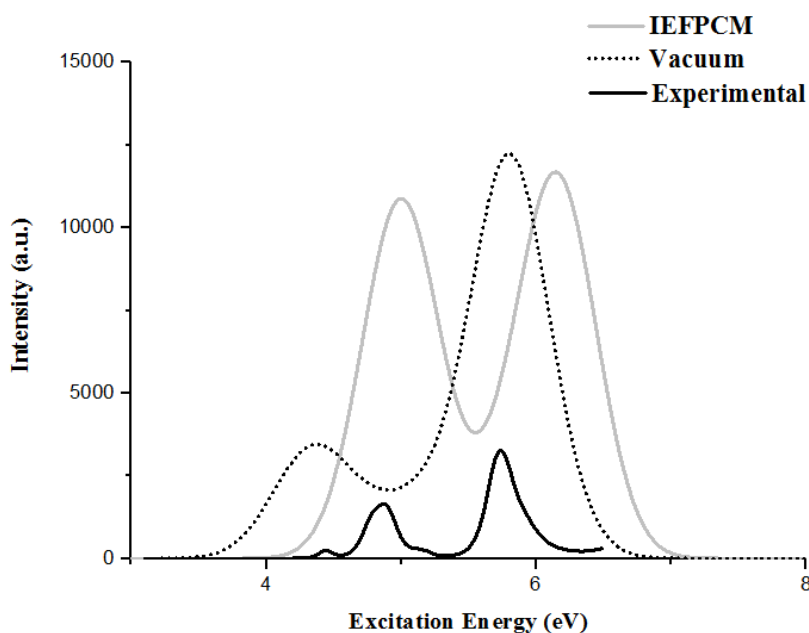


Figure 4.7: Comparison of the computed and experimental absorption spectra of $\text{Pt}(\text{CN})_4^{2-}$:
— Solution-phase absorption spectrum produced by IEFPCM/MN12-SX/LANL2DZ,
..... Gas-phase absorption spectrum produced by MN12-SX/LANL2DZ, — Aqueous experimental UV spectrum.

In comparison to the gas-phase UV spectrum, significant solvent shifts are observed in the aqueous MN12-SX/LANL2DZ spectrum for both absorption bands. A large bathochromic shift of 0.61 eV is seen for the lowest energy band in the solution phase MN12-SX/LANL2DZ spectrum of $\text{Pt}(\text{CN})_4^{2-}$. The highest energy band in the solution-phase computed spectrum of $\text{Pt}(\text{CN})_4^{2-}$ experiences a significant bathochromic shift of 0.34 eV. As shown in Figure 4.7, the solvent shift seen in the IEFPCM/MN12-SX/LANL2DZ spectrum of $\text{Pt}(\text{CN})_4^{2-}$ brings the aqueous theoretical spectrum into very good agreement with the solution phase experimental absorption spectrum of $\text{Pt}(\text{CN})_4^{2-}$.

Following solvation, the lowest band in the aqueous computed UV spectrum of $\text{Pt}(\text{CN})_4^{2-}$ is hyperchromically shifted and is three times as intense as first band in the aqueous experimental spectrum of $\text{Pt}(\text{CN})_4^{2-}$. In Figure 4.7, a notable hyperchromic shift is also observed for the highest energy band in the aqueous computed UV spectrum of $\text{Pt}(\text{CN})_4^{2-}$.

4.3.2 Platinum (IV) Hexacyanide

Geometry optimisation calculations were conducted using the B3LYP, CAM-B3LYP, M062X, M11, MN12-SX and PBE0 functionals in conjunction with LANL2DZ. During previous investigations of $\text{Pt}(\text{CN})_4^{2-}$, LANL2DZ performed best in terms of predicting the relative band positions. Therefore, it was the only basis set employed in both DFT and TDDFT calculations for $\text{Pt}(\text{CN})_6^{2-}$.

The key Pt-C and $\text{C}\equiv\text{N}$ bond lengths in the octahedral, O_h ground state optimised structure were calculated as 2.03 and 1.18 Å, respectively. The calculated bond lengths are in good agreement with other theoretical results available in the literature.¹²⁸ Frequency calculations yielded no imaginary values, confirming that these results were representative of a PES minimum.

While it was possible to conduct TDDFT calculations at 50 states when using the B3LYP, CAM-B3LYP and PBE0 functionals, 70 states were necessary for M06-2X and M11. MN12-SX required the highest number of states (90) to fully elucidate the second spectral band. It is interesting to observe in Figure 4.8, that even at their respectively high number of states, the highest energy band was still present on the rising edge of the lower energy band.

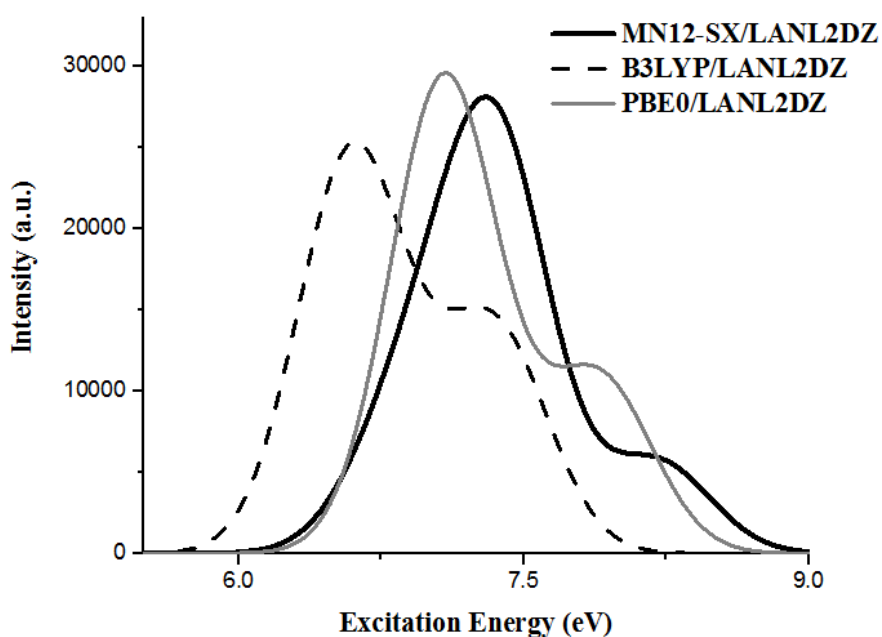


Figure 4.8: Theoretical UV spectrum of $\text{Pt}(\text{CN})_6^{2-}$ generated using LANL2DZ and the following functionals: - - -B3LYP (50 states), ——— PBE0 (50 states) and ——— MN12-SX (90 states).

The excitation energies produced from the TDDFT calculations on $\text{Pt}(\text{CN})_6^{2-}$ are presented in Table 4.5, where they have been compared to experimental excitation energies. A comparison of the excitation energies produced by the various functionals shows that B3LYP/LANL2DZ produced excitation energies that were significantly lower than the other functionals. As gas-phase experimental data was not available for $\text{Pt}(\text{CN})_6^{2-}$, it is not possible to determine precisely if B3LYP's results were a gross underestimation or in fact accurate. However,

comparisons of the computed UV spectra can be made with the aqueous experimental absorption spectrum that has been produced by Sen et al. (Figure 4.9).

Table 4.5: Comparison between the computed and experimental excitation energies of $\text{Pt}(\text{CN})_6^{2-}$, where **a** and **b** are the lowest energy spectral bands.^{a,b}

Functional	Excitation Energy (eV)	
	a	b
B3LYP	6.61	7.33
CAM-B3LYP	7.52	8.51
M062X	7.68	9.10
M11	8.05	9.09
MN12-SX	7.30	8.19
PBE0	7.09	7.89
Experimental ^b	5.64	-

^a TDDFT calculations performed at 90 states using LANL2DZ for all atoms.

^b Ref [43]

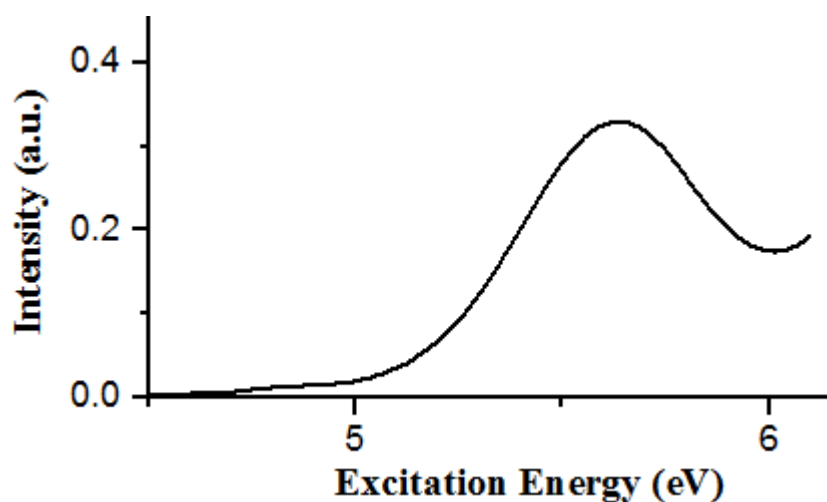


Figure 4.9: Aqueous experimental absorption spectrum of $\text{Pt}(\text{CN})_6^{2-}$ (courtesy of Sen et al.).⁴³

Comparison of the computed and experimental excitation energies for the lowest energy band in the electronic spectra of $\text{Pt}(\text{CN})_6^{2-}$ revealed B3LYP/LANL2DZ to be the best performing functional, (in terms of predicting the excitation energy of the first spectral band). Similar to

the TDDFT calculations on Pt(CN)₄²⁻, M062X and M11 were deemed the poorest performing functionals as they gave the largest overprediction of the lowest energy spectral band.

In Table 4.5, significant differences between the computed excitation energies and experimental excitation energies can be seen for all functionals. These differences can partly be attributed to the different phases of the experimental and computed UV spectra. The theoretical spectra of Pt(CN)₆²⁻ were produced by TDDFT calculations which were conducted in the gas phase. Conversely, the experimental absorption spectrum of Pt(CN)₆²⁻ was obtained in solution. Whilst comparisons of the computed and experimental absorption spectra of Pt(CN)₆²⁻ provides an indication of the density functional performance, only tentative conclusions can be drawn from these comparisons.

When employed during the study of the Pt(CN)₄²⁻ monomer, MN12-SX displayed the highest level of accuracy and produced results at reasonable computational cost. Consequently, MN12-SX/LANL2DZ data were used to assign the excited-state transitions for Pt(CN)₆²⁻ (Table 4.6). MOs associated with these assignments are presented in Figure 4.10.

Table 4.6: Assignment of the vertical excitations of Pt(CN)₆²⁻ using MN12-SX/LANL2DZ data.

Excitation Energy (eV)	Oscillator Strength (a.u.)	MO Transition	CI Coefficient (% contribution)	Assignment of Transition
7.35	0.2044	HOMO-4 → LUMO+4	0.45588 (41.57)	T _{1u} →E _g
		HOMO-3 → LUMO+3	0.59544 (70.91)	T _{1u} →E _g
		HOMO-5 → LUMO+4	0.57544 (66.23)	T _{1u} →E _g
8.19	0.1398	HOMO-14 → LUMO+4	0.61509 (75.67)	T _{1u} →E _g

At both excitation energies (7.35 and 8.19 eV), the dominant transitions were from T_{1u} to E_g states. It is interesting to observe that although the dominant transitions at 7.35 eV originated from three degenerate states, their CI coefficients vary significantly. Of these transitions, HOMO-4 \rightarrow LUMO+4 had the lowest coefficient (corresponding to 41.57%). With such a relatively low percentage in contribution, it is arguable that the HOMO-4 \rightarrow LUMO+4 transition is not representative of the overall excitations occurring at 7.35 eV. Therefore, it cannot be described as dominant.

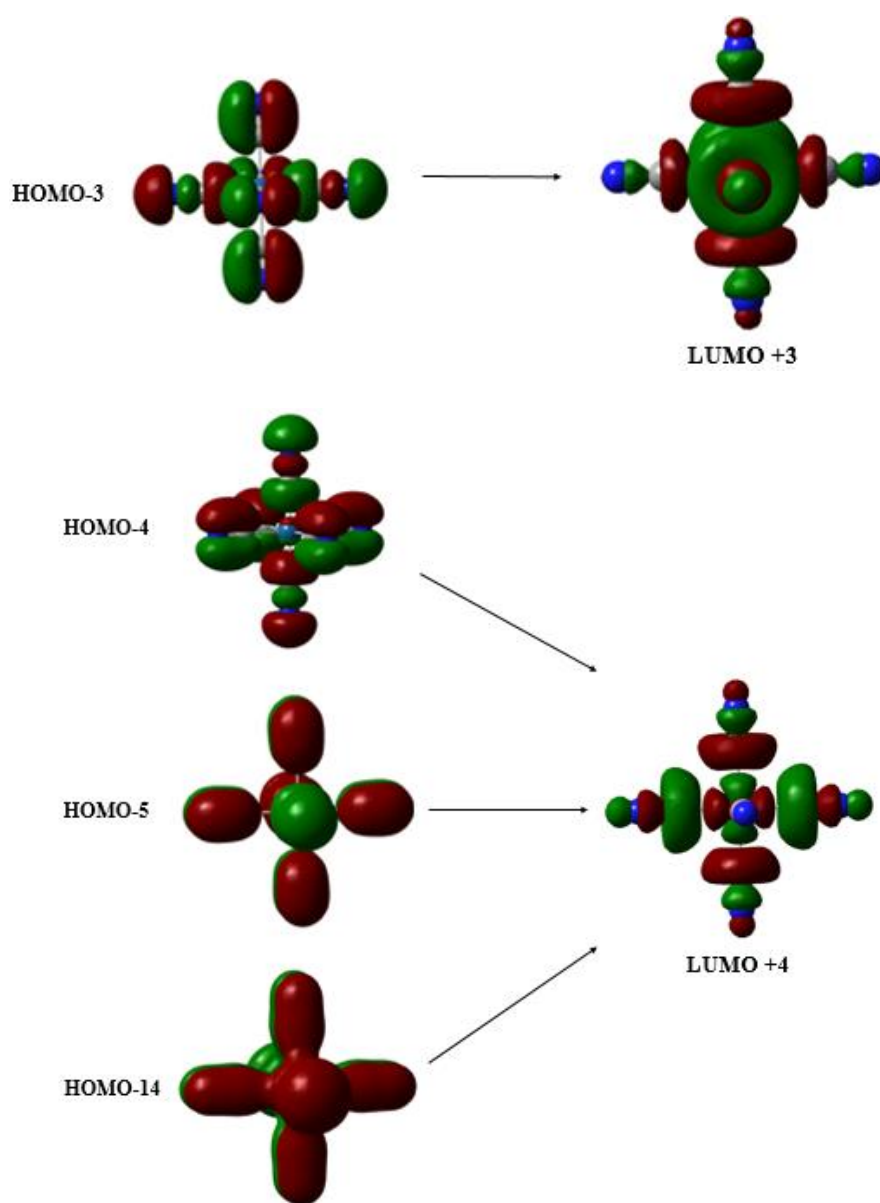


Figure 4.10: MOs involved in the electronic transitions of $\text{Pt}(\text{CN})_6^{2-}$, calculated at the MN12-SX/LANL2DZ level of theory.

4.3.3 Platinum (II) Tetracyanide·Water

DFT geometry optimisation calculations were carried out using the following functionals: B3LYP, CAM-B3LYP, M062X, M11, MN12-SX and PBE0. Figure 4.11 displays a typical structure obtained at the MN12-SX/LANL2DZ level of theory for $\text{Pt}(\text{CN})_4^{2-}\cdot\text{H}_2\text{O}$. There was little disparity between the calculated bond lengths of $\text{Pt}(\text{CN})_4^{2-}\cdot\text{H}_2\text{O}$ and its monomer $\text{Pt}(\text{CN})_4^{2-}$. The Pt-C bond length of the solvated complex was found to be the same as that of $\text{Pt}(\text{CN})_4^{2-}$ (1.19 Å) whilst the C-N length displayed a modest elongation of 0.1 Å. The distance of the N-H hydrogen bond was recorded as 1.71 Å.

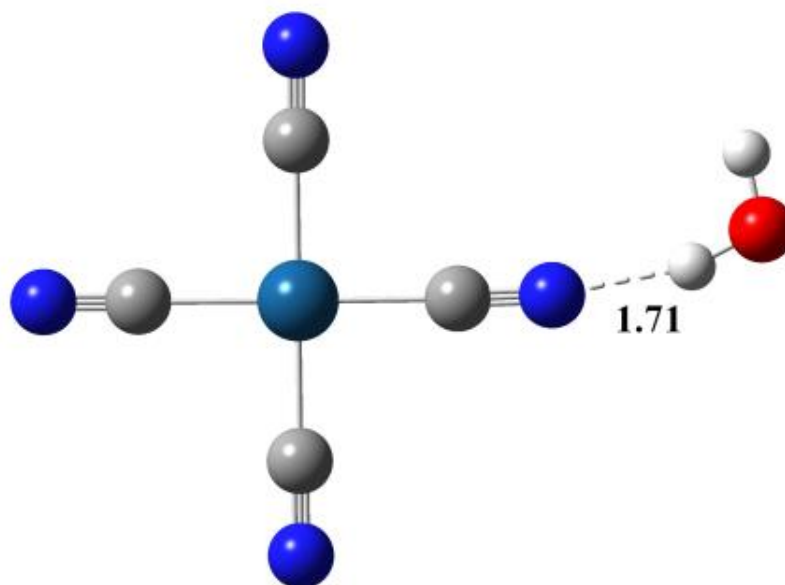


Figure 4.11: MN12-SX/LANL2DZ optimised ground state geometry of $\text{Pt}(\text{CN})_4^{2-}\cdot\text{H}_2\text{O}$. The hydrogen bond is indicated with a dashed line; hydrogen bond distance is in Å.

Following optimisation of the ground state structure, TDDFT calculations were performed at both 10 and 20 states. For all the functionals tested, two distinct bands of varying intensities were produced at 20 states. As shown in Table 4.7, these bands occurred at around 5.6 and 6.9 eV. Notably, these excitation energies were strikingly similar to the transitions of $\text{Pt}(\text{CN})_4^{2-}$.

Table 4.7: Comparison between the computed excitation energies of $\text{Pt}(\text{CN})_4^{2-}\cdot\text{H}_2\text{O}$ produced using TDDFT at 20 states, where **a** and **b** are the lowest energy spectral bands.

Functional	Excitation Energy (eV)	
	a	b
B3LYP	5.20	6.83
CAM-B3LYP	5.52	7.40
M062X	5.74	7.48
M11	5.74	7.02
MN12-SX	5.80	5.80
PBE0	5.38	7.06

It is interesting to note from Figure 4.12 how the trend in oscillator strength differs between functionals. B3LYP, CAM-B3LYP, M062X, M11 and PBE0 all produced spectra in which the first absorption band had a higher oscillator strength than the second. MN12-SX was the only functional tested which presented the second band as the most intense.

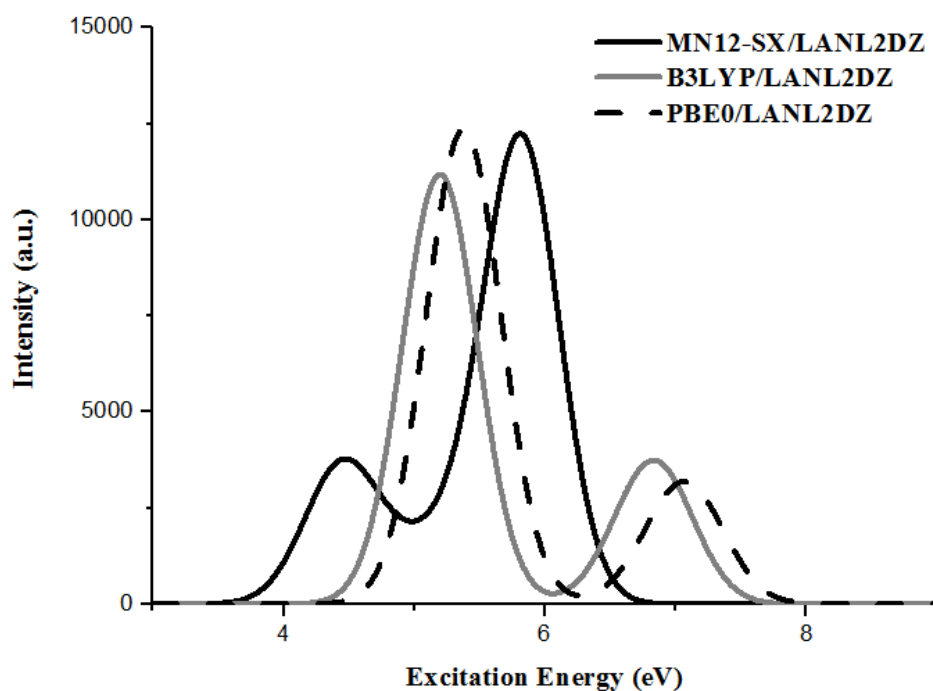


Figure 4.12: Comparison of the theoretical UV spectra produced using the following functionals and LANL2DZ: - - -PBE0, — B3LYP and — MN12-SX.

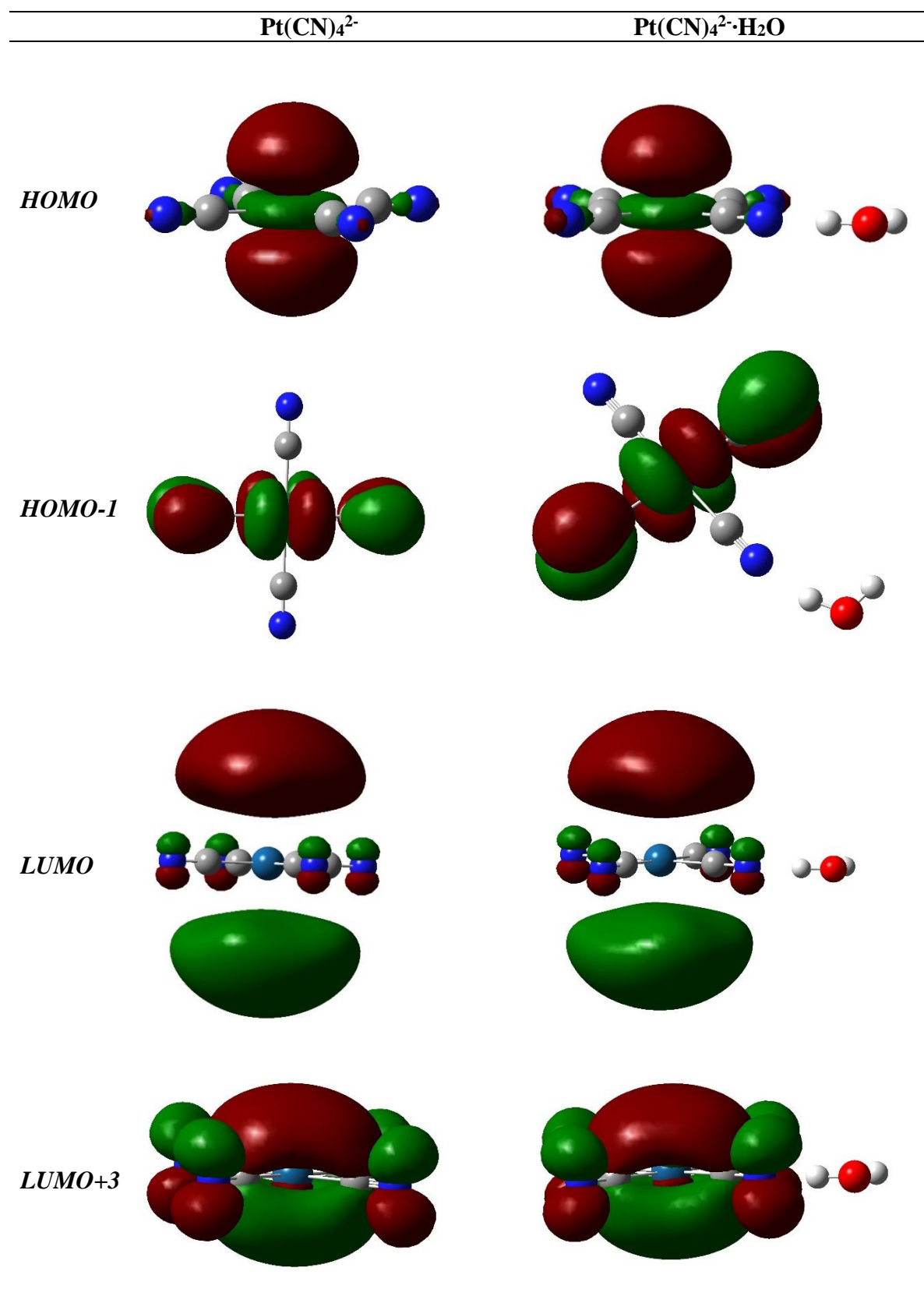
Owing to its previously good performance during the $\text{Pt}(\text{CN})_4^{2-}$ studies, TDDFT results generated by MN12-SX/LANL2DZ were used to assign the electronic transitions of $\text{Pt}(\text{CN})_4^{2-}\cdot\text{H}_2\text{O}$. These assignments are listed below in Table 4.8.

Table 4.8: Assignment of the electronic transitions of $\text{Pt}(\text{CN})_4^{2-}\cdot\text{H}_2\text{O}$.

Excitation Energy (eV)	Oscillator Strength (a.u.)	CI Coefficient (% contribution)	Assignment of Transition
4.48	0.0681	0.70060 (98.17%)	HOMO → LUMO
5.77	0.1196	0.68719 (94.45%)	HOMO-1 → LUMO+3

The dominant transitions at 4.48 and 5.77 eV corresponded respectively to the following excitations: HOMO→LUMO and HOMO-1→LUMO+3. Inspection of these MOs, reveals that these transitions involved only the orbitals in which are localised on $\text{Pt}(\text{CN})_4^{2-}$. On this basis, it can be concluded that H_2O does not appear to significantly perturb these electronic transitions of $\text{Pt}(\text{CN})_4^{2-}\cdot\text{H}_2\text{O}$. Further evidence for this comes from the strong similarities between the MOs participating in these transitions in $\text{Pt}(\text{CN})_4^{2-}\cdot\text{H}_2\text{O}$ and those in bare $\text{Pt}(\text{CN})_4^{2-}$. This is illustrated in Table 4.9 where the relevant MOs of $\text{Pt}(\text{CN})_4^{2-}$ and $\text{Pt}(\text{CN})_4^{2-}\cdot\text{H}_2\text{O}$ have been compared.

Table 4.9: A comparison between the MOs of $\text{Pt}(\text{CN})_4^{2-}$ and $\text{Pt}(\text{CN})_4^{2-}\cdot\text{H}_2\text{O}$ which are involved in the excited state transitions.



4.4 Conclusion

Density functional and basis set comparisons carried out on $\text{Pt}(\text{CN})_4^{2-}$ revealed MN12-SX/LANL2DZ to be the best performing combination followed closely by B3LYP/SDD. Examination of the MAEs showed that, with the exception of LANL2DZ, B3LYP consistently produced more accurate excitation energies. However, the use of this functional with basis sets other than LANL2DZ resulted in a significant increase in CPU time cost. It was suggested that the size of the pseudopotential used was responsible for this unexpected rise in computational time.

In summary, TDDFT calculations were performed on $\text{Pt}(\text{CN})_4^{2-}$, $\text{Pt}(\text{CN})_6^{2-}$ and $\text{Pt}(\text{CN})_4^{2-}\cdot\text{H}_2\text{O}$ complexes producing UV spectra and assignment of their excited-state transitions were made. The MOs involved in the transitions of $\text{Pt}(\text{CN})_4^{2-}\cdot\text{H}_2\text{O}$ and $\text{Pt}(\text{CN})_4^{2-}$ were found to be very similar in character, so that the hydrogen bond-bonding water molecule does not significantly perturb the electronic structure of $\text{Pt}(\text{CN})_4^{2-}$.

Chapter 5

A TDDFT Computational Study of Platinum (II) and (IV) Complexes Bound to a Single Nucleobase

5.1 Introduction

Following the discovery of cisplatin's anti-cancer properties in the 1960s, its use has become widespread in the treatment of cancer.¹²⁹ It is estimated that cisplatin and its various analogues are used in up to 50% of chemotherapeutic regimens.¹³⁰ However, the popularity and high success rate of cisplatin is overshadowed by its serious side effects including neurotoxicity and nephrotoxicity.¹²⁹⁻¹³² In an effort to overcome these side effects, recent research has focused on the chemotherapeutic use of alternative organometallic compounds.¹³⁴⁻¹³⁶

As discussed previously in Chapter 1, an area of research with considerable interest is the use of platinum complexes in photo activated chemotherapy (PACT). PACT is a combinatorial approach in which the anticancer properties of transition metals and the phototoxic effects of photosensitising agents are exploited.^{38,130} Transition metals are of specific interest as they display a variety of excited states which can easily be generated by irradiation.³⁸

Several studies have focused on the use of platinum (II) and (IV) complexes as photochemotherapeutic agents and have aimed to probe their photophysical and photochemical properties. Using NMR and mass spectrometry, Cubo et al. investigated the effects of irradiation over time in the reaction of Pt (II) and (IV) diamine complexes with

adenosine, guanine and cytidine nucleotides. The excited-state geometries and electronic properties of the Pt (II, IV) complexes were characterised using TDDFT. Calculations were performed at 32 states and employed PBE0 and LANL2DZ as an effective core potential on Pt.¹³⁶

Sen et al. conducted the first laser photodissociation study of isolated platinum dianions bound to a single nucleobase. These complexes represented model systems from which the photophysical processes associated with PDT were investigated. Photodepletion spectra of $\text{Pt}(\text{CN})_4^{2-}\cdot\text{Ur}$ and $\text{Pt}(\text{CN})_6^{2-}\cdot\text{Ur}$ were obtained and initial assignments of the electronic transitions were made.⁴¹

Later work by Sen et al. investigated the influence of the nucleobase on the photophysics of various $\text{Pt}(\text{CN})_4^{2-}\cdot\text{Nu}$ clusters using laser spectroscopy, where Nu = uracil, thymine, cytosine or adenine. All spectra contained broad absorptions bands and an increase in intensity was observed at higher energies, indicating the presence of an additional band above the spectral range. While there was little difference observed between spectra of the $\text{Pt}(\text{CN})_4^{2-}\cdot\text{Nu}$ complexes, notable variations were found in the absorption profiles of $\text{Pt}(\text{CN})_4^{2-}\cdot\text{Cy}$ and $\text{Pt}(\text{CN})_4^{2-}\cdot\text{Thy}$. In contrast to the very broad absorption band present in the $\text{Pt}(\text{CN})_4^{2-}\cdot\text{Thy}$ spectrum, the $\text{Pt}(\text{CN})_4^{2-}\cdot\text{Cy}$ spectrum contained a relatively narrow band. A correlation was found between the changes in band width and the differences in the photo fragmentation product ions.⁴³

The aim of this chapter will be to use TDDFT to calculate electronic spectra for the $\text{Pt}(\text{CN})_{4,6}^{2-}\cdot\text{Nu}$ complexes, where Nu = uracil or cytosine. To provide a more rigorous assignment of experimentally measured UV spectra, the nature of the excited-state transitions occurring within the $\text{Pt}(\text{CN})_{4,6}^{2-}\cdot\text{Nu}$ complexes will be characterised. Alongside this, the

performance of various density functionals and basis sets will be examined and their suitability to $\text{Pt}(\text{CN})_{4,6}^{2-}\cdot\text{Nu}$ complexes will be determined.

5.2 Computational Details

Ground-state geometry optimisations and frequency calculations were performed for $\text{Pt}(\text{CN})_4^{2-}\cdot\text{uracil}$, $\text{Pt}(\text{CN})_4^{2-}\cdot\text{cytosine}$ and $\text{Pt}(\text{CN})_6^{2-}\cdot\text{uracil}$ using DFT at the following levels of theory: B3LYP, CAM-B3LYP, M062X, M11, MN12-SX and PBE0.^{58-61,65-66} To study the electronic transitions of the $\text{Pt}(\text{CN})_{4,6}^{2-}\cdot\text{Nu}$ complexes, TDDFT calculations were performed at the six levels of theory using their respective optimised structures. All calculations were carried out using Gaussian 09 (G09), revision d.01.⁹⁵

To test their performance, a range of pseudopotentials were used in the DFT and TDDFT calculations for $\text{Pt}(\text{CN})_4^{2-}\cdot\text{uracil}$, $\text{Pt}(\text{CN})_4^{2-}\cdot\text{cytosine}$. The following ECPs were used on Pt: Def2-TZVPP, LANL2DZ and SDD. In calculations where LANL2DZ ECP was employed, 6-311++G(2d,2p) was used for all other atoms. The Def2-TZVPP and SDD ECPs were used in conjunction with LANL2DZ for all other atoms. By comparison with gas-phase photodepletion (absorption) spectra, the performance of the various functionals and basis sets tested were determined. In addition to the various pseudopotentials, the performance of the LANL2DZ basis set was also assessed. All calculations on $\text{Pt}(\text{CN})_6^{2-}\cdot\text{uracil}$ employed the LANL2DZ basis set.

5.3 Results and Discussion

5.3.1 $\text{Pt}(\text{CN})_4^{2-}$ ·uracil

DFT geometry optimisation calculations were performed on $\text{Pt}(\text{CN})_4^{2-}$ ·uracil and produced the ground-state structure shown in Figure 5.1 below. Frequency calculations did not generate any imaginary values, therefore it can be concluded that the optimised structures represent local minima on the PES.

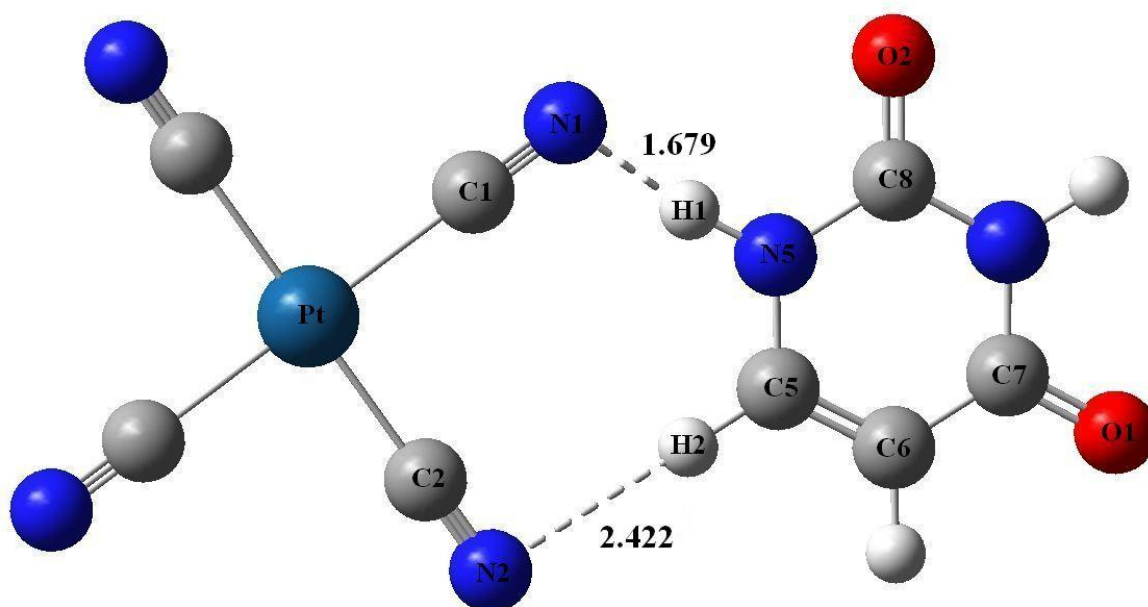


Figure 5.1: Ground-state B3LYP/LANL2DZ optimised geometry of $\text{Pt}(\text{CN})_4^{2-}$ ·uracil. Hydrogen bonds are indicated as dashed lines and bond lengths are in Angstroms.

Geometrically significant bond distances were calculated from the B3LYP/LANL2DZ optimised structure and are displayed in Table 5.1.

Table 5.1: Selected bond distances (Å) in the B3LYP/LANL2DZ optimised geometry of Pt(CN)₄²⁻·uracil.

Bond	Bond Distance (Å)
Pt–C1	2.011
Pt–C2	2.024
C1–N1	1.191
C2–N1	1.194
C1–N1···H1	1.679
C2–N2···H2	2.422
N5–H1	1.064
C5–H2	1.089
C5–C6	1.375
C7–O1	1.267
C8–O2	1.259

In comparison to its isolated constituent “monomer” parts (i.e. isolated Pt(CN)₄²⁻ and isolated uracil), there were notable differences observed in the bond lengths of Pt(CN)₄²⁻·uracil .

Compared to isolated Pt(CN)₄²⁻, the Pt–C2 bond in Pt(CN)₄²⁻·uracil was elongated by 0.01 Å. Hydrogen bonding was shown to perturb the C5–H2 and N5–H1 bonds of Pt(CN)₄²⁻·uracil. In comparison to isolated uracil, the C5–H2 and N5–H1 bonds in Pt(CN)₄²⁻·Uracil were elongated by 0.05 and 0.01 Å, respectively. The N1···H1 and N2···H2 hydrogen bond lengths were 1.679 and 2.422 Å, respectively. These values were in very good agreement with the corresponding hydrogen bond lengths reported by Sen et al.¹²⁴

TDDFT calculations were performed at the following levels of theory to study the electronic transitions of Pt(CN)₄²⁻·uracil: B3LYP, CAM-B3LYP, M062X,M11, MN12-SX and PBE0.

To assess the effect of changing the basis set on the excitation energy, the basis set used in calculations was also varied. The excitation energies produced using each functional/basis set combination and the experimental energies are listed in Table 5.2. The mean absolute errors have also been calculated for each combination and are displayed in Table 5.3.

Table 5.2: Comparison between the theoretical excitation energies obtained using TDDFT and the experimental, gas-phase results (in eV) of $\text{Pt}(\text{CN})_4^{2-}\cdot\text{uracil}$, where **a** and **b** are the lowest energy spectral bands.

	SDD (ECP)^a		LANL2DZ (ECP)^b		DEF2-TZVPP (ECP)^a		LANL2DZ	
	a	b	a	b	a	b	a	b
B3LYP	5.05	6.31	5.13	6.28	5.19	6.41	5.11	6.26
CAM-B3LYP	5.35	6.71	5.39	6.78	5.44	6.82	5.41	6.61
M062X	5.56	6.72	5.65	7.03	5.64	7.98	5.64	6.67
M11	5.50	6.88	5.49	6.58	5.64	6.87	5.62	6.76
MN12-SX	5.28	6.54	4.40	5.20	5.32	6.69	5.32	5.86
PBE0	5.22	6.51	5.28	6.31	5.33	6.58	5.28	6.48
Experimental^c	4.64	-	4.64	-	4.64	-	4.64	-

^a ECP was used solely on Pt, while LANL2DZ was used for C, N, O and H atoms.

^b ECP was used on Pt only, while 6-311++G(2d,2p) was used for C, N, O and H atoms.

^c Ref [41]

Table 5.3: The mean absolute errors in excitation energy (eV) of $\text{Pt}(\text{CN})_4^{2-}\cdot\text{uracil}$.

Functional	SDD (ECP)^a	LANL2DZ (ECP)^b	Def2-TZVPP (ECP)^a	LANL2DZ
B3LYP	0.41	0.49	0.55	0.47
CAM-B3LYP	0.71	0.75	0.80	0.77
M062X	0.92	1.01	1.00	1.00
M11	0.86	0.85	1.00	0.98
MN12-SX	0.64	0.24	0.68	0.68
PBE0	0.58	0.64	0.69	0.64

^a ECP was used solely on Pt, while LANL2DZ was used for C, N, O and H atoms.

^b ECP was used on Pt only, while 6-311++G(2d,2p) was used for C, N, O and H atoms.

Comparison of the MAEs in Table 5.3 showed that calculation employing MN12-SX/LANL2DZ (ECP) produced the lowest error in the excitation energies of $\text{Pt}(\text{CN})_4^{2-}\cdot\text{uracil}$. The value of this error (0.24 eV) was significantly lower than that of any other functional/basis set combination. However the use of MN12-SX/LANL2DZ (ECP) was not recommended for $\text{Pt}(\text{CN})_4^{2-}\cdot\text{uracil}$ because it failed to give a qualitatively accurate description

of the experimental spectrum. In contrast to the two distinct experimental bands, the highest energy band in the computational spectrum was very close in energy to that of the lower band (Figure 5.2). The intensity of these bands were also significantly lower than the intensity of the experimental bands.

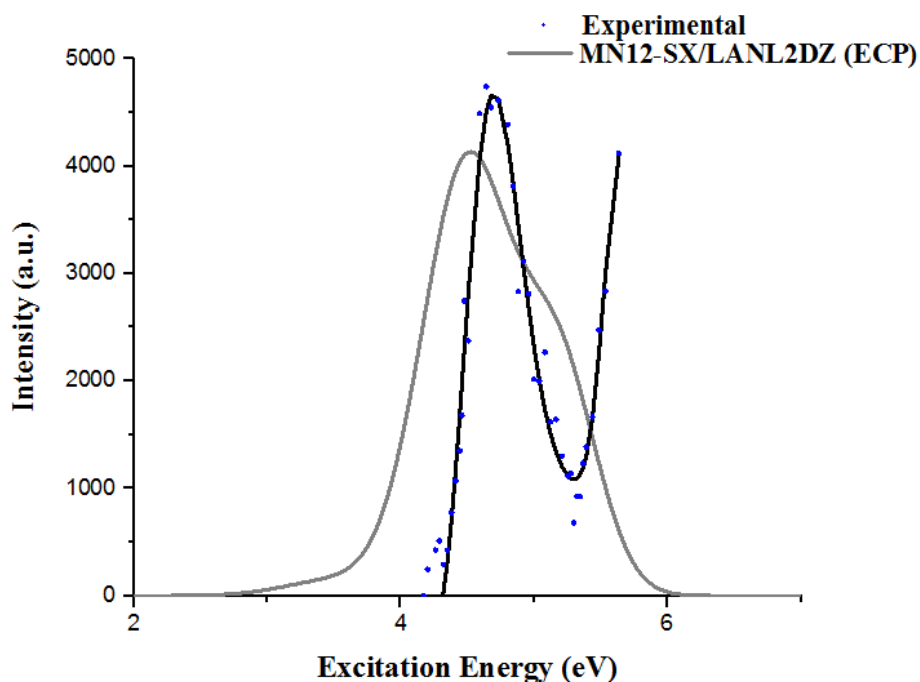


Figure 5.2: Comparison between the computed and experimental electronic spectra of $\text{Pt}(\text{CN})_4^{2-}\cdot\text{uracil}$: • Photodepletion (absorption) spectrum (courtesy of Sen et al.),⁴¹ — Band profile for photodepletion (absorption) spectrum, — MN12-SX/LANL2DZ (ECP) (90 states).

In addition, there was a relatively long computational time associated with the MN12-SX/LANL2DZ (ECP) calculation (21.1 hours). This time was lengthened by the higher number of states used. While it was generally possible to produce two absorption bands at 50 states using other functional/basis set combinations, MN12-SX/LANL2DZ (ECP) calculations had to be performed at 90 states. As previously discussed, calculations at this relatively high number of states produced bands which were uncharacteristically close in energy. In order to observe a significant separation of these bands, TDDFT calculations must

be conducted at an even higher number of states. This is likely to result in a further increase in computational time.

Calculations which employed SDD (ECP) had the lowest errors overall. In particular, the UV spectra produced using B3LYP/SDD (ECP) was found to be in very good agreement with the experimental results (Figure 5.3). The SDD and LANL2DZ basis sets gave similarly accurate results overall, in terms of predicting the excitation energies of the experimental UV bands. A comparison between the UV spectra produced by B3LYP/SDD (ECP) and B3LYP/LANL2DZ in Figure 5.3, shows that although the energy of the lowest band is described more accurately (in relation to the experimental UV spectrum) by B3LYP/ SDD (ECP), B3LYP/LANL2DZ predicts the experimental energy of the highest experimental band more accurately.

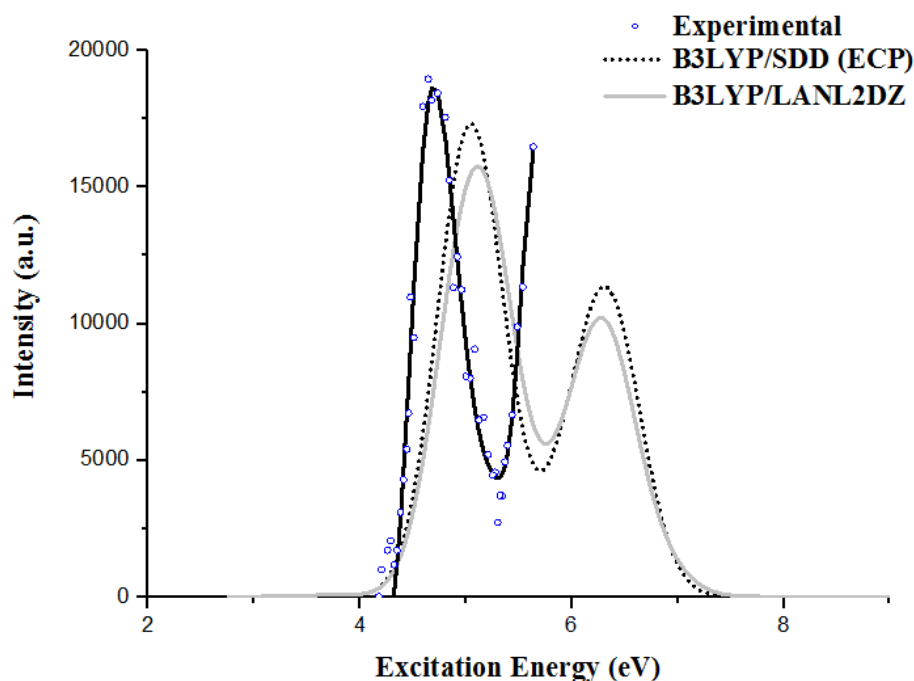


Figure 5.3: Comparison between the computed and experimental electronic spectra of $\text{Pt}(\text{CN})_4^{2-}\cdot\text{uracil}$: \circ Photodepletion (absorption) spectrum (courtesy of Sen et al.),⁴¹ **—** Band profile for photodepletion (absorption) spectrum, \cdots B3LYP/SDD (ECP) (50 states) and — B3LYP/LANL2DZ (50 states).

The computational time associated with performing a TDDFT calculation using B3LYP/SDD (ECP) was slightly longer (22 mins) than B3LYP/LANL2DZ. This increase is representative of the higher CPU time cost associated with the various TDDFT calculations which employed SDD (ECP). Taking all of this into account, B3LYP/LANL2DZ was considered to be the best performing combination.

Def2-TZVPP (ECP) was deemed the worst performing basis set due to its poor description of the highest energy spectral bands and the lengthy computational times associated with calculations. Use of this basis set resulted in the significant overestimation in the position of the highest energy spectral band. This is exemplified in Figure 5.4 where the B3LYP/Def2-TZVPP, MN12-SX/Def2-TZVPP and experimental spectra have been compared.

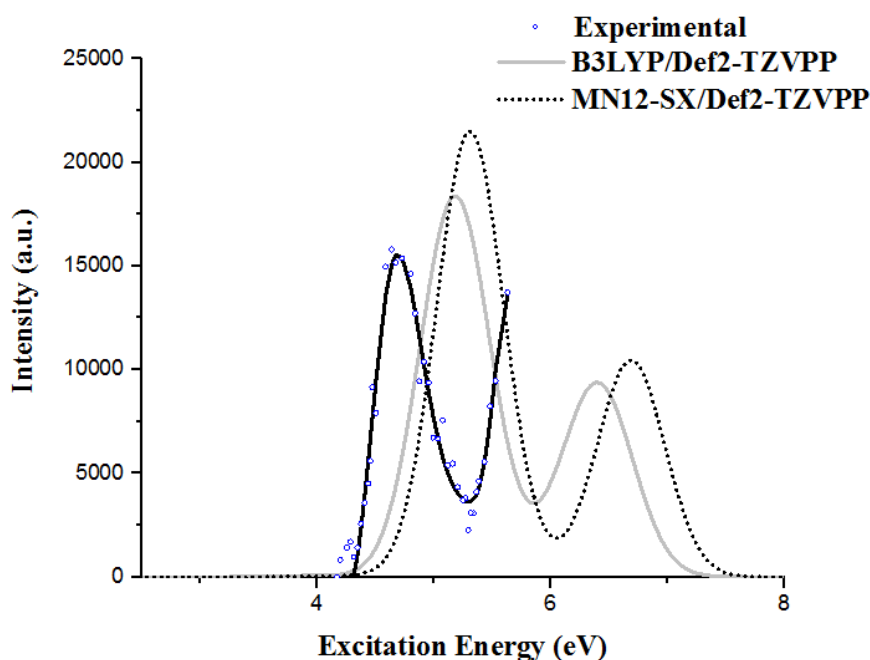


Figure 5.4: Comparison between the computed and experimental electronic spectra of $\text{Pt}(\text{CN})_4^{2-}\cdot\text{uracil}$: \circ Photodepletion (absorption) spectrum (courtesy of Sen et al.),⁴¹ — Band profile for photodepletion (absorption) spectrum, \cdots MN12-SX/Def2-TZVPP (ECP) (50 states) and — B3LYP/Def2-TZVPP (ECP) (50 states).

As Def2-TZVPP (ECP) described the position of the lowest energy band satisfactorily, its MAEs were similar to that of the LANL2DZ (ECP) and LANL2DZ basis sets. If the MAEs

took into account the highest spectral bands, the errors associated with TDDFT/Def2-TZVPP(ECP) calculations of Pt(CN)₄²⁻-uracil would be significantly higher. Additionally, TDDFT calculations employing Def2-TZVPP (ECP) had a very high computational time cost. In comparison to B3LYP/LANL2DZ, it took 21.6 hours longer to perform a TDDFT calculation at 50 states using B3LYP/Def2-TZVPP.

B3LYP and MN12-SX were considered the best performing functional as they yielded the lowest MAEs overall and their calculations had the lowest computational cost. In comparison to these functionals, CAM-B3LYP performed poorly. CAM-B3LYP largely overestimated the energy of the two experimental bands and therefore had a relatively high average error of 0.75 eV. The addition of Coulomb attenuation to B3LYP was expected to enhance the performance of this functional (in comparison to B3LYP), as it rectified the incorrect long-range behaviour of the exchange potential. This incorrect long-range behaviour was thought to be the cause of a number of B3LYP's failures such as its poor description of TDDFT excitations and charge transfer states.⁶¹ Following the examination of the MOs involved in the electronic transitions of Pt(CN)₄²⁻-uracil (Figure 5.7), it was evident that the excitations at 4.90 and 6.32 eV corresponded to charge transfer transitions. Therefore, it was interesting to observe that CAM-B3LYP provided a less accurate description of these charge transfer states in comparison to B3LYP.

The performances of B3LYP and CAM-B3LYP can be attributed to the type of charge-transfer transitions occurring at 4.90 and 6.32 eV, i.e. short-range. Although B3LYP performs poorly in its description of long-range charge transfer transitions, it is capable of describing short-range charge-transfer interactions with a high level of accuracy. Evidence for this can be found in a recent study by Peach et al. in which the electronic excitation energies were determined using the B3LYP, CAM-B3LYP and PBE functionals. The electronic transitions of variety of molecules were investigated to permit the study of a wide variety of excitations.

The study included molecules in which charge-transfer interactions are prevalent such as (dimethylamino)benzonitrile (DMABN). The errors in excitation energy associated with the various TDDFT calculations performed, were plotted against a function of spatial orbital overlap, Λ (Figure 5.5). High and low values of Λ indicate short and long-range interactions, respectively.¹³⁷

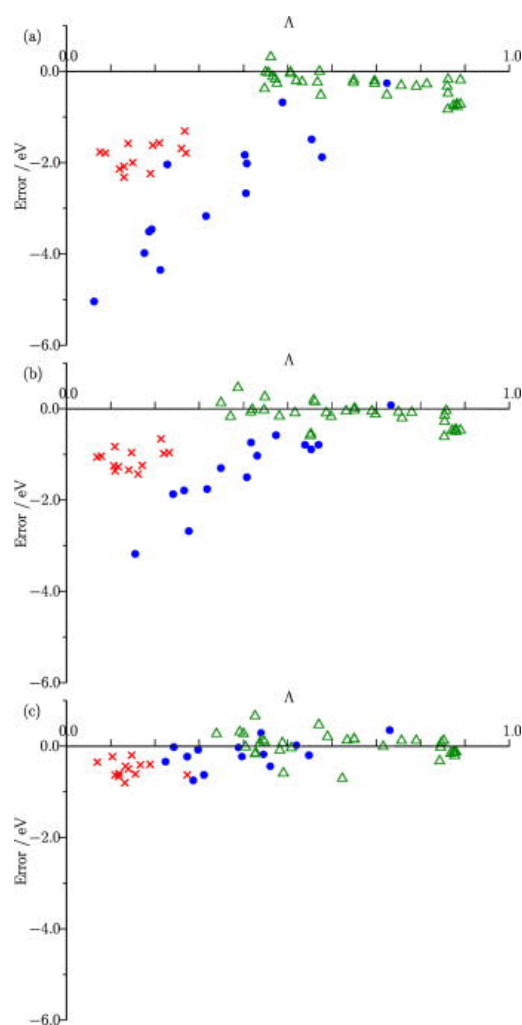


Figure 5.5: Error in excitation energy plotted against Λ values for TDDFT calculations employing the following functionals: (a) PBE (b) B3LYP and (c) CAM-B3LYP. Each point represents a single excitation: (Δ) local excitations, (\times) Rydberg excitations, and (\bullet) charge-transfer excitations. This figure has been reproduced from Ref [137]

As shown in Figure 5.5b, B3LYP predicted the excitation energies of short-range charge-transfer interactions with relatively low error, but produced relatively large errors in the

prediction of long-range charge-transfer interactions. As the charge-transfer interactions studied in $\text{Pt}(\text{CN})_4^{2-}$ -uracil are short-range, they were adequately described by B3LYP.

Figure 5.5c shows that CAM-B3LYP predicted the excitation energies of both the short and long-range charge-transfer interactions of the molecules studied with relatively little error. Based on the findings of this study by Peach et al., CAM-B3LYP was expected to yield relatively low MAEs when predicting the excitation energies of $\text{Pt}(\text{CN})_4^{2-}$ -uracil. However, it is possible that use of CAM-B3LYP led to an over-correction in the excitation energies of $\text{Pt}(\text{CN})_4^{2-}$ -uracil and therefore relatively high MAEs.

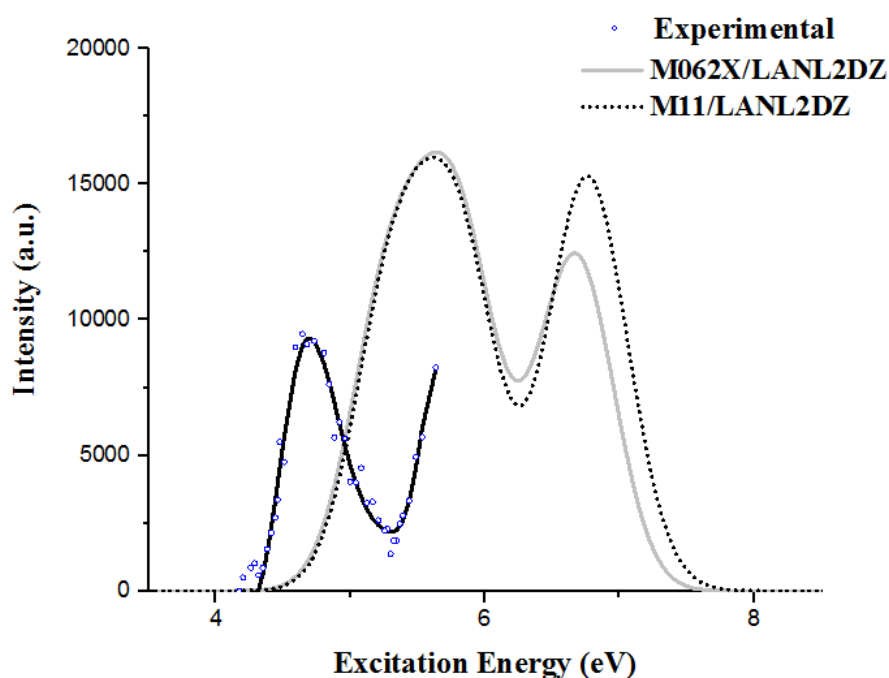


Figure 5.6: Comparison between the computed and experimental electronic spectra of $\text{Pt}(\text{CN})_4^{2-}$ -uracil: \circ Photodepletion (absorption) spectrum (courtesy of Sen et al.),⁴¹ **—** Band profile for photodepletion (absorption) spectrum, \cdots M11/LANL2DZ (50 states) and **—** B3LYP/LANL2DZ (50 states).

M062X was deemed the worst performing functional, followed by M11. As depicted in Figure 5.6, both functionals greatly overestimated the energies of the two experimental

spectral bands. Consequently, the average errors of M062X and M11 were respectively 0.50 and 0.44 eV higher than the best performing functional, B3LYP.

B3LYP/LANL2DZ was considered the best performing functional/basis set combination and its UV spectral data was used to assign the electronic transitions of $\text{Pt}(\text{CN})_4^{2-}$ ·uracil. A summary of these assignments are presented in Table 5.4.

Table 5.4: Assignment of the electronic transitions of $\text{Pt}(\text{CN})_4^{2-}$ ·uracil. Excitation energies have been calculated using B3LYP/LANL2DZ.

Excitation Energy (eV)	Oscillator Strength (a.u.)	MO Transition	CI Coefficient (% contribution)	Assignment of Transition
4.90	0.1760	HOMO-6 → LUMO	0.67229 (90.39)	$e_g \rightarrow \pi^*$
6.32	0.1945	HOMO-6 → LUMO+1	0.52585 (55.30)	HOMO-6 → π^*
		HOMO-14 → LUMO	0.41652 (34.70)	HOMO-14 → π^*

As discussed previously, the excited state transitions characterising the two absorption bands were all charge transfer in nature. Examination of the MOs involved in each transition showed that electron density was being transferred from platinum to uracil (Figure 5.7). The transition at 4.90 eV corresponded to electron density moving from an e_g orbital on platinum to a π^* orbital on uracil. Interestingly, the e_g orbital was also involved in the lowest energy transition of isolated $\text{Pt}(\text{CN})_4^{2-}$.

The transition at 6.32 eV was also to π^* orbital on uracil but had originated from the HOMO-6 orbital localised on platinum. Attention should be drawn to the relatively low CI coefficient of this transition. The CI coefficient corresponding to 55% suggested that there was more than one transition which made a significant contribution to the band at 6.32 eV. Following HOMO-6 → LUMO+1, the second highest contribution was made by the HOMO-14

→LUMO transition. In contrast to HOMO-6, electron density in the HOMO-14 orbital was distributed on both molecules in $\text{Pt}(\text{CN})_4^{2-}\cdot\text{uracil}$ (ie. $\text{Pt}(\text{CN})_4^{2-}$ and uracil).

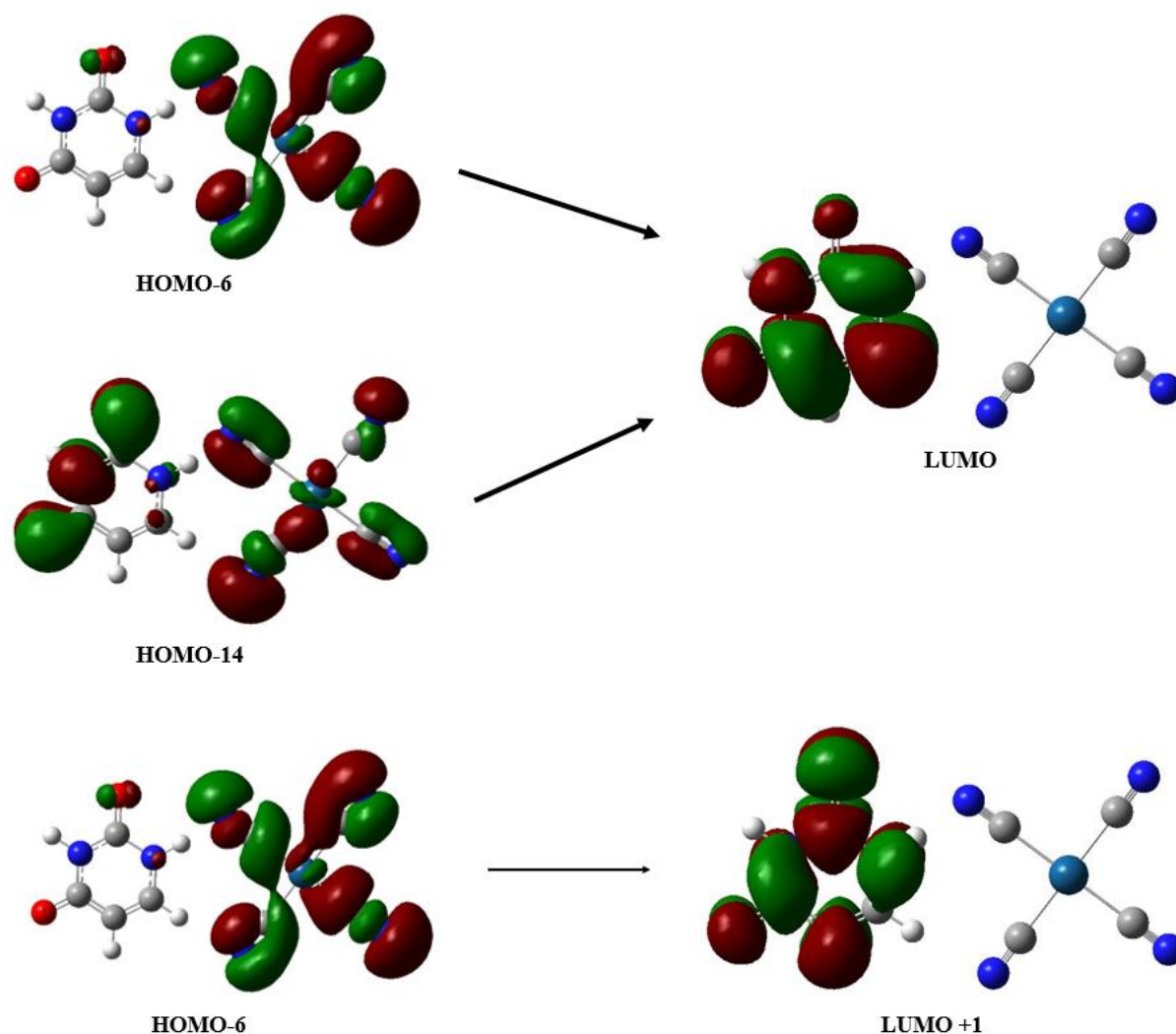


Figure 5.7: Molecular orbitals involved in the electronic transitions of $\text{Pt}(\text{CN})_4^{2-}\cdot\text{uracil}$. MOs were calculated at the B3LYP/LANL2DZ level of theory.

5.3.2 $\text{Pt}(\text{CN})_4^{2-}\cdot\text{cytosine}$

A series of DFT calculations were performed on $\text{Pt}(\text{CN})_4^{2-}\cdot\text{cytosine}$ at the B3LYP, CAM-B3LYP, M062X, M11, MN12-SX and PBE0 levels of theory. The resulting ground-state optimised geometry of $\text{Pt}(\text{CN})_4^{2-}\cdot\text{cytosine}$ is shown in Figure 5.8.

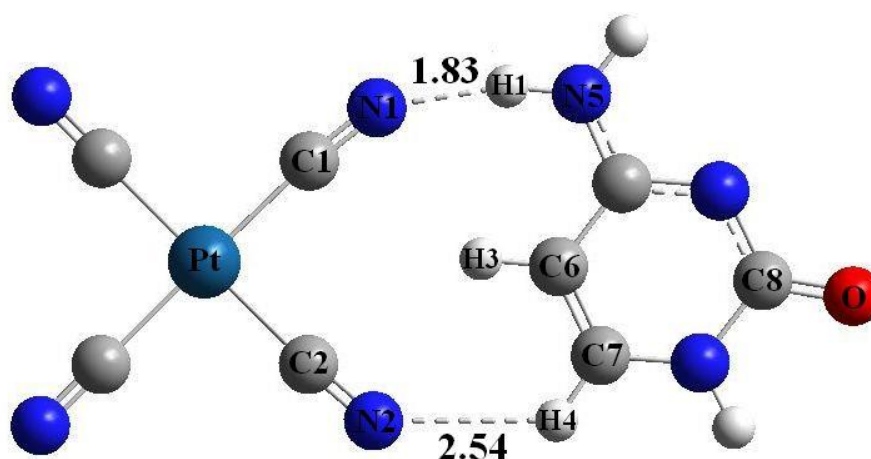


Figure 5.8: B3LYP/LANL2DZ optimised ground state geometry of $\text{Pt}(\text{CN})_4^{2-}$ ·cytosine. Hydrogen bonds are indicated as dashed lines and bond distances are in Å.

Significant bond lengths in the B3LYP/LANL2DZ optimised geometry of $\text{Pt}(\text{CN})_4^{2-}$ ·cytosine were calculated and are displayed in Table 5.5. Similar to $\text{Pt}(\text{CN})_4^{2-}$ ·uracil, the calculated bond lengths in $\text{Pt}(\text{CN})_4^{2-}$ ·cytosine were slightly elongated in comparison its isolated constituent “monomers”, (i.e. isolated $\text{Pt}(\text{CN})_4^{2-}$ and isolated cytosine). Increases of 0.015, 0.003 and 0.029 Å were observed for the Pt–C2, C1–N1, and N5–H1 bonds, respectively.

Table 5.5: Key bond distances (Å) in the B3LYP/LANL2DZ optimised geometry of $\text{Pt}(\text{CN})_4^{2-}$ ·cytosine.

Bond	Bond Distance (Å)
Pt–C1	2.018
Pt–C2	2.026
C1–N1	1.191
C2–N2	1.193
C1–N1···H1	1.827
C2–N2···H4	2.538
N1–H3	2.542
N2–H3	2.693
N5–H1	1.039
C7–H4	1.086
C6–C7	1.365
C8–O	1.276

Using the six DFT optimised structures, a series of TDDFT calculations were performed at 50 states. To substantiate the conclusions made for Pt(CN)₄²⁻·uracil, the basis set was again varied. The excitation energies produced from these calculations are displayed in Table 5.6. The MAEs were also calculated for each functional/basis set combination and are presented in Table 5.7.

Table 5.6: Comparison between the theoretical excitation energies obtained using TDDFT and the experimental, gas-phase results (in eV) of Pt(CN)₄²⁻·cytosine; where **a** and **b** are the lowest energy spectral bands.

Functional	SDD (ECP) ^a		LANL2DZ (ECP) ^b		Def2-TZVPP (ECP) ^a		LANL2DZ	
	a	b	a	b	a	b	a	b
B3LYP	5.19	6.56	5.29	6.17	5.30	6.58	5.28	6.58
CAM-B3LYP	5.51	6.85	5.58	6.72	5.53	7.06	5.64	6.81
M062X	5.81	6.79	5.81	6.35	5.86	6.93	5.86	6.79
M11	5.80	6.85	5.74	6.48	5.83	6.76	5.93	6.83
MN12-SX	4.93	5.72	4.19	-	5.35	6.48	4.72	5.79
PBE0	5.37	6.75	5.44	6.49	5.46	6.93	5.46	6.75
Experimental^c	4.75	-	4.75	-	4.75	-	4.75	-

^a ECPs were used solely on Pt, while LANL2DZ was used for C and N.

^b ECP was used on Pt only, while 6-311++G(2d,2p) was used for C and N.

^c Ref [43]

Table 5.7: The mean absolute errors in excitation energy (eV) of Pt(CN)₄²⁻·cytosine.

Functional	SDD (ECP) ^a	LANL2DZ (ECP) ^b	Def2-TZVPP (ECP) ^a	LANL2DZ
B3LYP	0.44	0.54	0.55	0.53
CAM-B3LYP	0.76	0.83	0.78	0.89
M062X	1.06	1.06	1.11	1.11
M11	1.05	0.99	1.08	1.18
MN12-SX	0.18	0.56	0.60	0.03
PBE0	0.62	0.69	0.71	0.71

^a ECPs were used solely on Pt, while LANL2DZ was used for C and N.

^b ECP was used on Pt only, while 6-311++G(2d,2p) was used for C and N.

The trend observed in the density functional performance for $\text{Pt}(\text{CN})_4^{2-}$ ·cytosine, generally followed that of $\text{Pt}(\text{CN})_4^{2-}$ ·uracil. Calculations employing the MN12-SX and B3LYP functionals reproduced the experimental spectra reasonably well. With the exception of MN12-SX/LANL2DZ and MN12-SX/SDD (ECP), B3LYP produced slightly lower errors than MN12-SX overall. MN12-SX/LANL2DZ and MN12-SX/SDD (ECP) had the lowest errors of the functional/basis set combinations tested (0.03 and 0.18 eV, respectively). As shown in Figure 5.9, an extremely good agreement was found between the experimental and MN12-SX/LANL2DZ spectra. In addition to the highly accurate excitation energies produced, MN12-SX/LANL2DZ also successfully replicated the energy between the experimental bands.

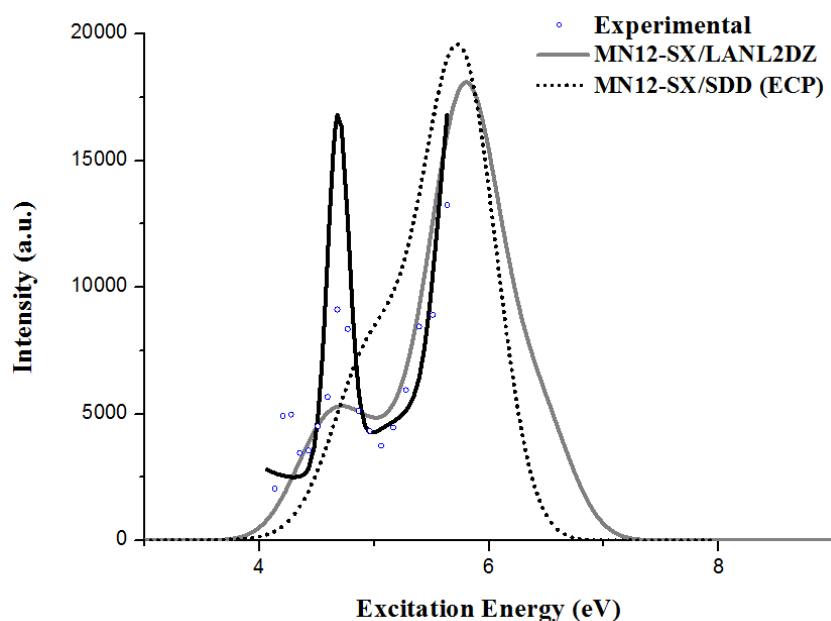


Figure 5.9: Comparison of the computed and experimental UV spectra of $\text{Pt}(\text{CN})_4^{2-}$ ·cytosine: \circ Photodepletion (absorption) spectrum (courtesy of Sen et al.),⁴³ — Band profile for photodepletion (absorption) spectrum, MN12-SX/SDD (ECP) (50 states) and — MN12-SX/LANL2DZ (50 states).

The errors listed in Table 5.7 also show that there was little deviation between the excitation energies of MN12-SX/SDD (ECP) and the experimental energies. Further analysis of the spectrum in Figure 5.7 showed that while MN12-SX/SDD (ECP) overestimated the energy of

the lowest band, it slightly underestimated the position of highest energy band. This underestimation resulted from the failure of MN12-SX/SDD (ECP) to reproduce the ca. 1 eV separation between the spectral bands seen in the experimental UV spectrum.

Of the B3LYP/basis set variations tested, the two best performing combinations were found to be B3LYP/SDD (ECP) and B3LYP/LANL2DZ. At 0.44 and 0.53 eV, the respective errors associated with the B3LYP/SDD (ECP) and B3LYP/LANL2DZ calculations were significantly higher than that of MN12-SX/SDD (ECP) or MN12-SX/LANL2DZ.

In comparison to MN12-SX/SDD (ECP), the UV spectrum of B3LYP/SDD (ECP) contained two well defined spectral bands with a difference of 1.37 eV (Figure 5.10). The bands in both B3LYP/SDD (ECP) and B3LYP/LANL2DZ spectra were of very similar intensity and width. The intensity of both these spectral bands were much higher in the UV spectra B3LYP/SDD (ECP) and B3LYP/LANL2DZ than in that of MN12-SX/SDD (ECP) or MN12-SX/LANL2DZ.

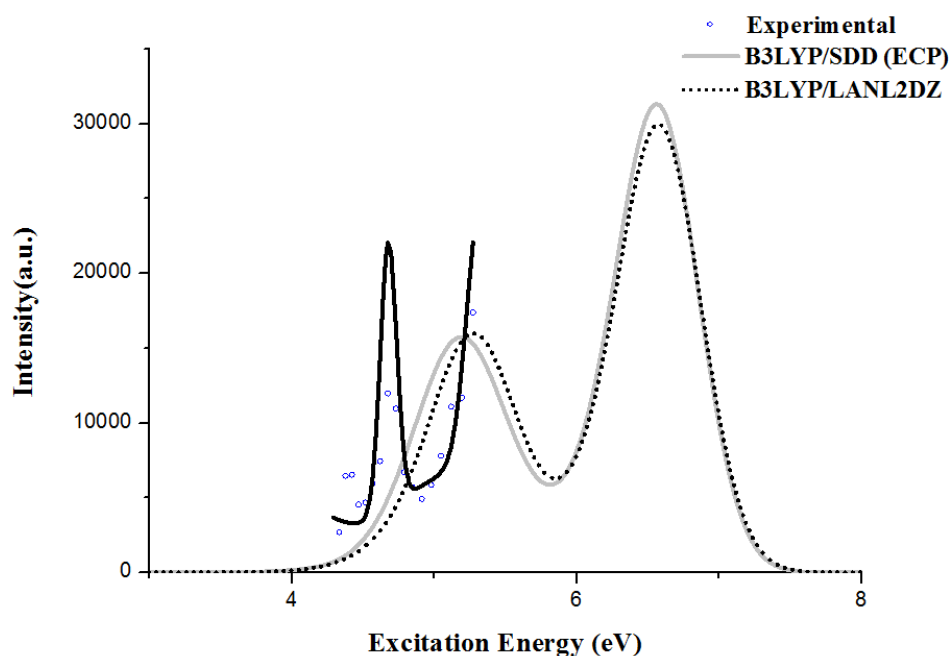


Figure 5.10: Comparison of the computed and experimental UV spectra of $\text{Pt}(\text{CN})_4^{2-}$ · cytosine: \circ Photodepletion (absorption) spectrum (courtesy of Sen et al.),⁴³ — Band profile for photodepletion (absorption) spectrum, \cdots B3LYP/LANL2DZ (50 states) and — B3LYP/SDD (ECP) (50 states).

B3LYP/SDD (ECP) and B3LYP/LANL2DZ exemplify the typical performance of the SDD (ECP) and LANL2DZ basis sets. Both basis sets performed in a similarly accurate manner, producing spectral bands of similar energies and intensities. In comparison to LANL2DZ, SDD (ECP) tended to better describe the position of the lowest energy spectral band. With regards to the higher energy band, a marginally better agreement was generally found between the experimental and theoretical LANL2DZ spectra.

In spite of the better agreement between the experimental and MN12-SX/LANL2DZ spectra, B3LYP/LANL2DZ was considered the better performing functional/basis set combination due to the considerably smaller CPU time cost. The computational time required to perform a TDDFT calculation at 50 states using MN12-SX/LANL2DZ was on average 1.51 hours less than B3LYP/LANL2DZ. The high computational cost associated with B3LYP/LANL2DZ made its use impractical for studying the excited states of $\text{Pt}(\text{CN})_4^{2-}$ -cytosine.

Adhering to the trend seen in the study $\text{Pt}(\text{CN})_4^{2-}$ -uracil, calculations employing CAM-B3LYP produced much higher errors than B3LYP. The poor performance of CAM-B3LYP was attributed to the failure of this functional to accurately describe short-range CT excitations. As will be discussed, the electronic transitions of $\text{Pt}(\text{CN})_4^{2-}$ -cytosine corresponded to short-range CT transitions. It is possible that the modification of the exchange potential in CAM-B3LYP resulted in the overcorrection of these CT transitions. Therefore, these transitions were better described by B3LYP in comparison to CAM-B3LYP.

As a result of their lengthy computational times and high MAEs, M062X and M11 were deemed the poorest performing density functionals. M062X and M11 consistently overestimated the energy of the lowest experimental band by an average of 1.08 eV. Consequently, the MAEs of M062X and M11 were on approximately double that of B3LYP.

The trend in basis set performance also followed the pattern observed during the study of $\text{Pt}(\text{CN})_4^{2-}$ -uracil. For the purpose of predicting the excitation energies, LANL2DZ was deemed the best performing basis set followed closely by SDD (ECP). When employed as a pseudopotential on Pt, LANL2DZ (ECP) performed satisfactorily. As demonstrated by the B3LYP/ LANL2DZ (ECP) and PBE0/ LANL2DZ (ECP) UV spectra in Figure 5.11, the position and intensity of the lowest energy band was described suitably by LANL2DZ (ECP). Furthermore, LANL2DZ (ECP) often predicted the position of the highest energy experimental band most accurately (Table 5.6). However, the pseudopotential basis set often failed to reproduce the relative band intensities observed in the experimental spectrum. The lowest energy band was often more intense than the highest energy band.

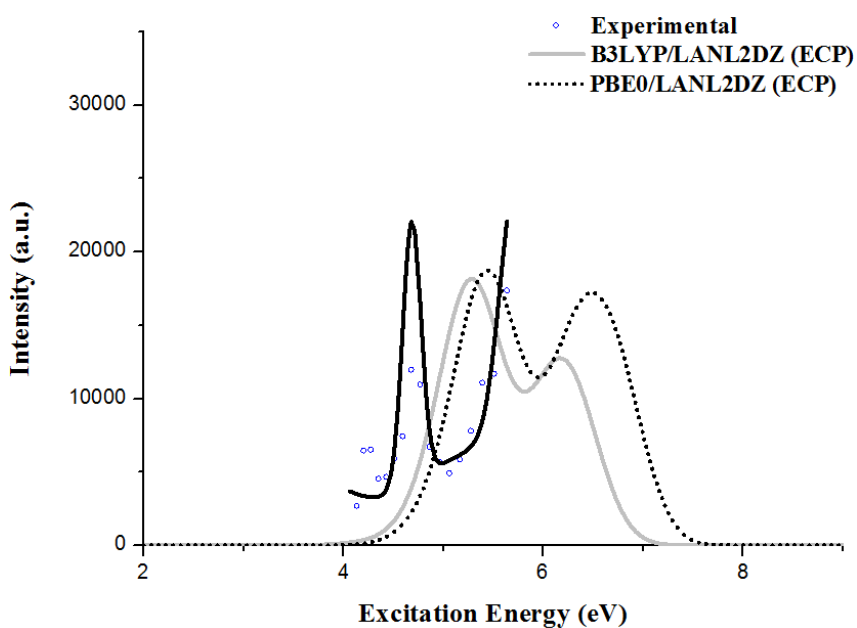


Figure 5.11: Comparison of the computed and experimental UV spectra of $\text{Pt}(\text{CN})_4^{2-}$ -cytosine: \circ Photodepletion (absorption) spectrum (courtesy of Sen et al.),⁴³ **—** Band profile for photodepletion (absorption) spectrum, **.....** PBE0/LANL2DZ (ECP) (90 states) and **—** B3LYP/LANL2DZ (ECP) (90 states).

The main drawback of using LANL2DZ (ECP) was the lengthy computational time associated with TDDFT calculations and the high number of states which calculations had to be performed at. While most TDDFT calculations could be conducted at 50 states using other

basis sets, LANL2DZ (ECP) often required 90 states. At 50 states, calculations employing LANL2DZ (ECP) seldom produced two spectral bands. In an extreme case, it was necessary to perform a TDDFT calculation at 150 states using MN12-SX/LANL2DZ (ECP), as the spectrum calculated at 90 states produced one band of extremely low intensity. However, calculations performed at 150 states using MN12-SX/LANL2DZ (ECP) still did not reproduce the two spectral bands seen in the experimental spectrum. Similar to the TDDFT calculations of Pt(CN)₄²⁻·uracil, Def2-TZVPP (ECP) was considered the worst performing basis set in terms of its calculations that employed Def2-TZVPP (ECP) had a significantly longer computational time and produced UV spectra in which the position of the highest energy band was grossly overestimated.

Given that B3LYP/LANL2DZ was considered the best performing functional/basis set combination, its data were used to assign the electronic transitions of Pt(CN)₄²⁻·cytosine in Table 5.8. The MOs involved in these transitions are depicted in Figure 5.12.

Table 5.8: Assignment of the electronic transitions of Pt(CN)₄²⁻·cytosine using TD-B3LYP/LANL2DZ results.

Excitation Energy (eV)	Oscillator Strength (a.u.)	MO Transition	CI Coefficient (% contribution)	Assignment of Transition
5.25	0.1129	HOMO-1 → LUMO+3	0.68211 (93.05)	$\pi \rightarrow$ LUMO+3
6.59	0.5137	HOMO-3 → LUMO+2	0.43219 (37.36)	HOMO-3 → π^*
		HOMO-5 → LUMO+2	0.35380 (25.03)	HOMO-5 → π^*

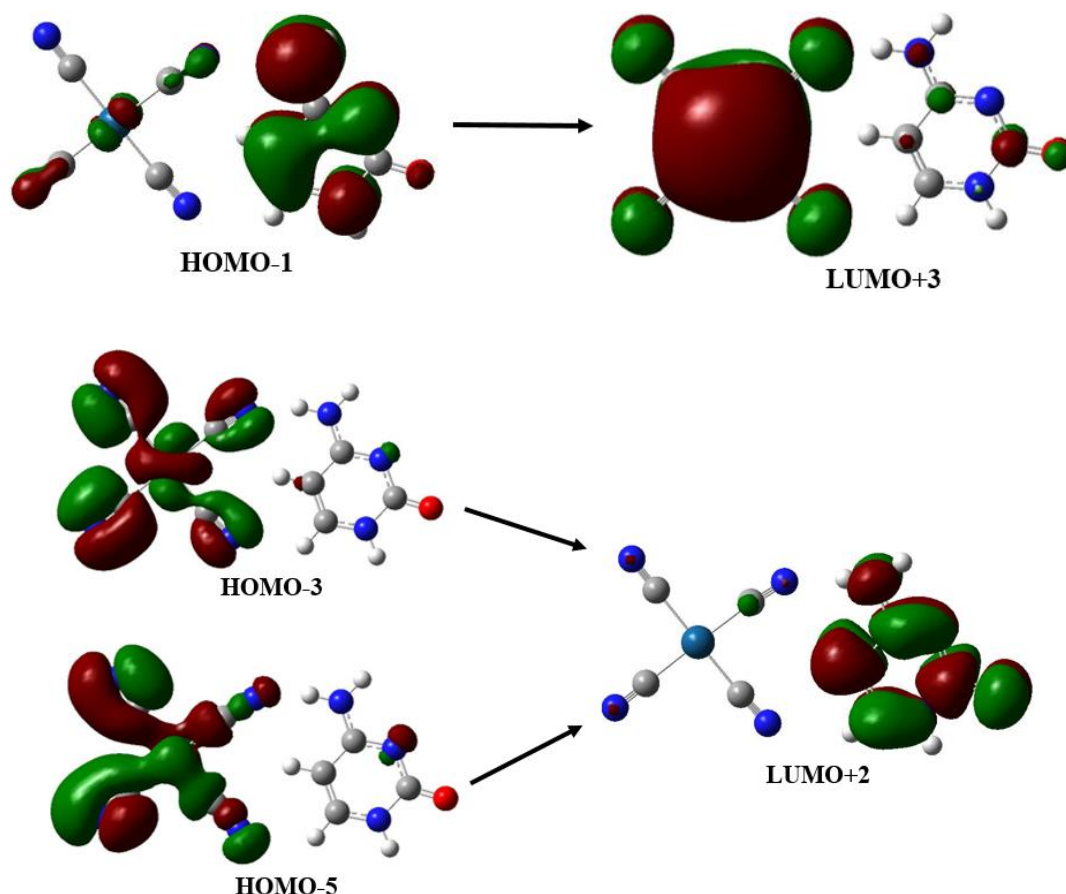


Figure 5.12: MOs involved in the electronic transitions of Pt(CN)₄²⁻·cytosine. MOs were calculate using B3LYP/LANL2DZ.

As previously stated, the transitions at 5.25 and 6.59 eV corresponded to charge transfer interactions. Examination of the HOMO-1 and LUMO+3 orbitals revealed that the excitation at 5.25 involved a transition from a π orbital localised on the nucleobase to an MO localised on the platinum complex. At 6.59 eV, the dominant transition originated from the HOMO-3 orbital which is localised in platinum to a π^* orbital on cytosine. However, the HOMO-3 \rightarrow LUMO+2 transition had a relatively small CI coefficient of 0.43 and therefore indicated that there were other transitions which made a significant contribution to the excited state. Other dominant transitions included HOMO-5 \rightarrow LUMO+2. The similarities between the HOMO-3 and HOMO-5 orbitals can be seen in Figure 5.12. As in HOMO-3, electron density in HOMO-5 is situated in an orbital localised on Pt(CN)₄²⁻.

5.3.3 Pt(CN)₆²⁻·uracil

The previous studies of Pt(CN)₄²⁻·uracil and Pt(CN)₄²⁻·cytosine had deemed LANL2DZ the best performing basis set, therefore ground-state geometry optimisation calculations were performed using only this basis set. The six functionals tested during the previous investigations of Pt(CN)₄²⁻·uracil and Pt(CN)₄²⁻·cytosine were used in DFT and TDDFT calculations. Figure 5.13 displays the ground-state optimised structure produced by B3LYP/LANL2DZ.

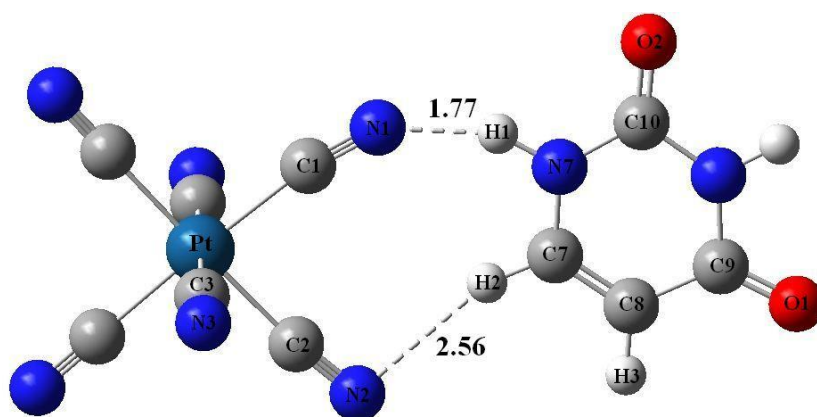


Figure 5.13: Ground state structure of B3LYP/LANL2DZ optimised Pt(CN)₆²⁻·uracil.

Using the B3LYP/LANL2DZ optimised structure, the key bond lengths within the complex were calculated and are listed in Table 5.9.

Table 5.9: Selected bond distances (Å) in the B3LYP/LANL2DZ optimised geometry of Pt(CN)₆²⁻·uracil.

Bond	Bond Distance (Å)
Pt–C1	2.047
Pt–C2	2.049
C1–N1	1.183
C2–N2	1.187
C3–N3	1.186
C1–N1···H1	1.773
C2–N2···H2	2.563
N7–H1	1.046
C7–H2	1.087
C6–C7	1.373
C9–O1	1.265
C10–O2	1.257

In comparison to Pt(CN)₄²⁻·uracil, Pt(CN)₆²⁻·uracil formed weaker ionic hydrogen bonds. The C1-N1···H1 and C2-N2···H2 hydrogen bond lengths of Pt(CN)₆²⁻·uracil were 0.09 and 0.14 Å longer, respectively, than that of Pt(CN)₄²⁻·uracil. The calculated hydrogen bond lengths were in very good agreement with literatures values obtained by Sen et al.⁴¹

The electronic transitions of Pt(CN)₆²⁻·uracil were studied using TDDFT at the B3LYP, CAM-B3LYP, M062X, M11, MN12-SX and PBE0 levels of theory. The excitation energies of the two spectral bands produced by the various functionals are outlined in Table 5.10 below. The MAEs have been calculated for each functional and are shown in Table 5.11.

Table 5.10: Comparison between the computed and experimental excitation energies of Pt(CN)₆²⁻·uracil, where **a** and **b** are the lowest energy spectral bands.^{a,b}

Functionals	Excitation Energy (eV)	
	a	b
B3LYP	4.94	6.32
CAM-B3LYP	5.18	7.21
M062X	5.33	7.49
M11	5.35	6.82
MN12-SX	5.23	6.55
PBE0	5.11	6.49
Experimental ^b	4.90	-

^a TDDFT calculations performed at 30 states using the LANL2DZ basis set for all atoms.

^b Ref [41]

Table 5.11: Mean absolute error in excitation energies (eV) for Pt(CN)₆²⁻·uracil.

Functional	Mean Absolute Error (eV)
B3LYP	0.04
CAM-B3LYP	0.28
M062X	0.43
M11	0.45
MN12-SX	0.33
PBE0	0.21

A comparison of the MAEs showed that calculations employing B3LYP/LANL2DZ produced errors significantly lower than the other functionals. The low error associated with

B3LYP/LANL2DZ (0.04 eV) indicates a very good agreement between the computed and experimental UV spectra of $\text{Pt}(\text{CN})_6^{2-}$ -uracil. As shown in Figure 5.14, B3LYP/LANL2DZ also predicts a significantly lower excitation energy for the highest energy spectral band, compared to the other functionals.

Interestingly, CAM-B3LYP/LANL2DZ performs relatively well in terms of predicting the excitation energy of the first band in the experimental UV spectrum of $\text{Pt}(\text{CN})_6^{2-}$ -uracil. Previous use of this functional in the TDDFT calculations of $\text{Pt}(\text{CN})_4^{2-}$ -uracil and $\text{Pt}(\text{CN})_4^{2-}$ -cytosine, resulted in relatively high MAEs. CAM-B3LYP/LANL2DZ predicted the energy of the first spectral band accurately but gave a poor description of the higher energy bands in the UV spectra of $\text{Pt}(\text{CN})_6^{2-}$ -uracil. At 30 states, CAM-B3LYP/LANL2DZ produced a UV spectrum in which the second spectral band was present on the rising edge of the highest energy band (Figure 5.14). The small spacing in between the higher energy bands produced by CAM-B3LYP/LANL2DZ was in contrast to the three distinct spectral bands produced by M062X/LANL2DZ (Figure 5.14).

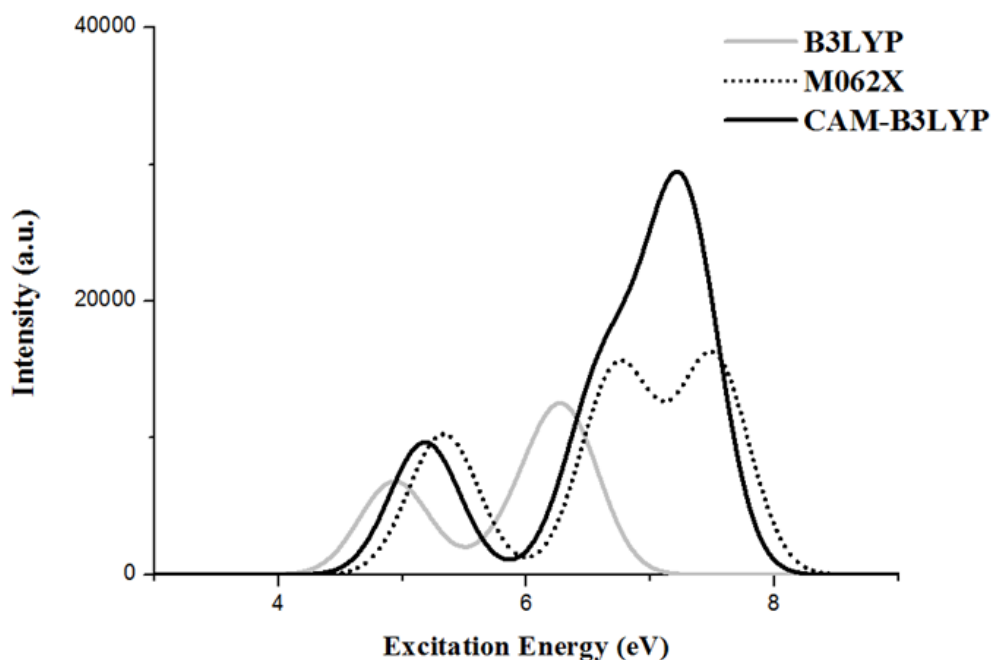


Figure 5.14: Comparison of the computed UV spectra of $\text{Pt}(\text{CN})_6^{2-}$ -uracil: — B3LYP/LANL2DZ, ····· M062X/LANL2DZ and — CAM-B3LYP/LANL2DZ.

Similar to the trend exhibited by Pt(CN)₄²⁻·uracil and Pt(CN)₄²⁻·cytosine, the M062X and M11 functionals were deemed the worst performing density functionals in terms of predicting the excitation energies of Pt(CN)₆²⁻·uracil. Although M062X/LANL2DZ and M11/LANL2DZ produced relatively high MAEs (in comparison to the other functionals), the MAEs of M062X/LANL2DZ and M11/LANL2DZ for Pt(CN)₆²⁻·uracil are significantly lower than that of Pt(CN)₄²⁻·uracil and Pt(CN)₆²⁻·cytosine.

Attention should be drawn to the general magnitude of the MAEs. In comparison to Pt(CN)₄²⁻·uracil and Pt(CN)₄²⁻·cytosine, errors associated with the TDDFT calculations of Pt(CN)₆²⁻·uracil were much smaller, indicating a better agreement between the theoretical and experimental UV spectra overall.

B3LYP was considered to be the best performing functional, therefore the results from the TD-B3LYP/LANL2DZ calculation were used to study the nature of the electronic transitions in Pt(CN)₆²⁻·uracil.

Table 5.12: Assignment of the vertical excitations of Pt(CN)₆²⁻·uracil using B3LYP/LANL2DZ data.

Excitation Energy (eV)	Oscillator Strength (a.u.)	MO Transition	CI Coefficient (% contribution)	Assignment of Transition
4.94	0.1679	HOMO → LUMO	0.67120 (90.10)	$\pi \rightarrow \pi^*$
6.32	0.2631	HOMO → LUMO+1	0.54835 (60.14)	$\pi \rightarrow \pi^*$
		HOMO-12 → LUMO	0.37327 (27.87)	$\pi \rightarrow \pi^*$

Unlike Pt(CN)₄²⁻·uracil and Pt(CN)₄²⁻·cytosine, the electronic transitions of Pt(CN)₆²⁻·uracil were not charge-transfer in nature. The absorption bands at 4.94 and 6.32 eV were associated

with transitions involving orbitals that were localised exclusively on the nucleobase. Both excitations at 4.94 and 6.32 eV corresponded to $\pi \rightarrow \pi^*$ transitions localised on uracil. These assignments were in line with the initial characterisations made by Sen et al.

In addition to HOMO \rightarrow LUMO+1, the HOMO-12 \rightarrow LUMO transition made a notable contribution to the excited state at 6.32eV. Examination of the HOMO-12 and LUMO orbitals in Figure 5.15 revealed that this transition was also $\pi \rightarrow \pi^*$ in nature.

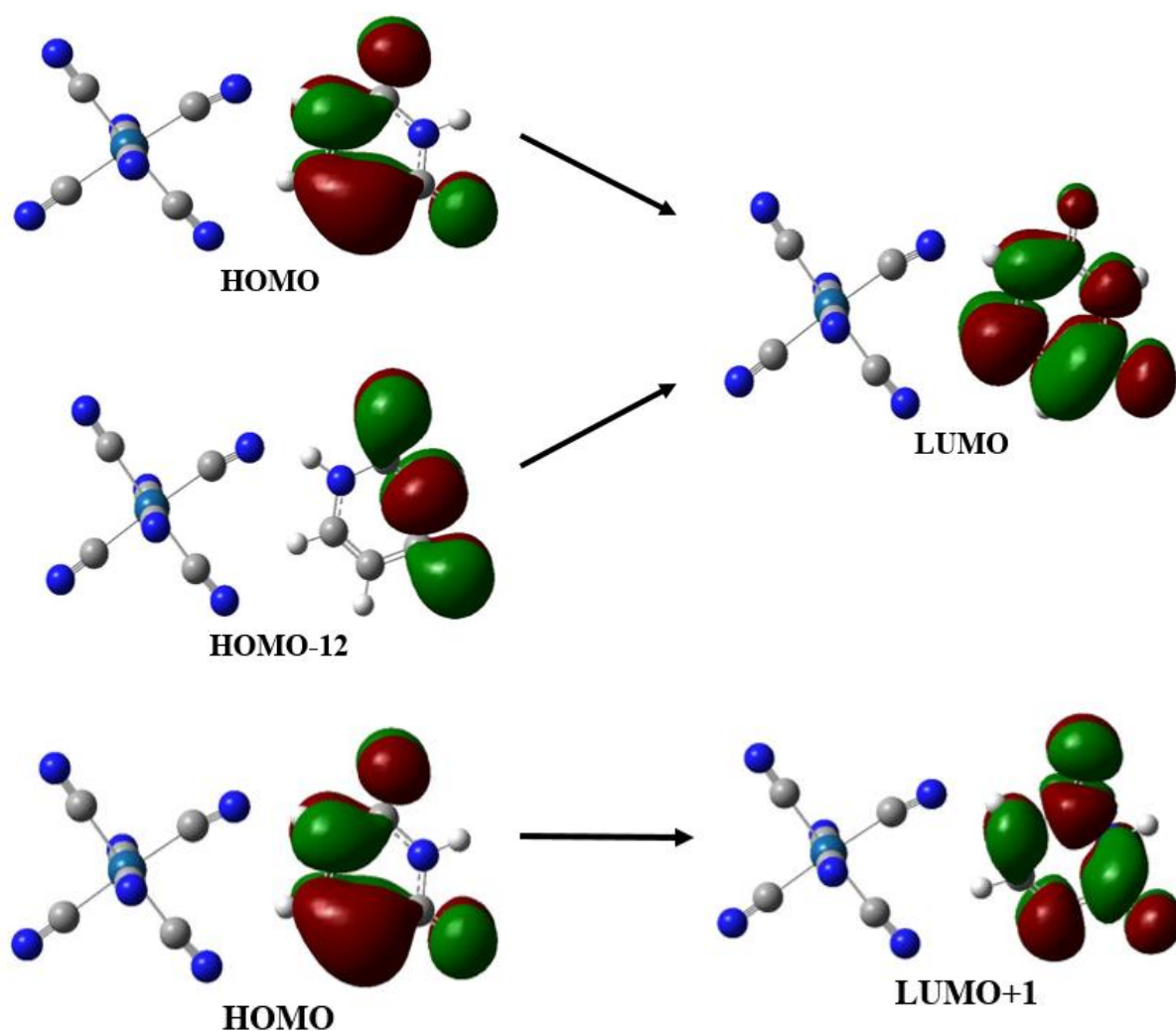


Figure 5.15: MOs involved in the electronic transitions of Pt(CN)₆²⁻·uracil. MOs were calculated at the B3LYP/LANL2DZ level of theory.

5.4 Conclusion

The electronic transitions of $\text{Pt}(\text{CN})_4^{2-}$ -uracil, $\text{Pt}(\text{CN})_4^{2-}$ -cytosine and $\text{Pt}(\text{CN})_6^{2-}$ -uracil were studied using TDDFT at the following levels of theory: B3LYP, CAM-B3LYP, M062X, M11, MN12-SX and PBE0. Using the computed UV spectra, the electronic transitions of $\text{Pt}(\text{CN})_4^{2-}$ -Uracil and $\text{Pt}(\text{CN})_4^{2-}$ -Cytosine were characterised and were found to be of a short-range charge-transfer nature. In contrast to the electronic transitions of $\text{Pt}(\text{CN})_4^{2-}$ -uracil and $\text{Pt}(\text{CN})_4^{2-}$ -cytosine, MOs that were of $\pi\pi^*$ character and were localised on the nucleobase dominated the electronic transitions of $\text{Pt}(\text{CN})_6^{2-}$ -uracil.

Comparison of the density functionals and basis sets used in calculations revealed B3LYP/LANL2DZ to be the best performing functional/basis set combination, in terms of predicting the excitation energies of the experimental UV spectra. Generally, calculations employing B3LYP/LANL2DZ had low associated MAEs and were of a low computational time cost. M062X and M11 functionals were deemed the worst performing as their use often led to a significant over prediction of the experimental excitation energies. Def2-TZVPP was considered the worst performing basis set as it often produced the highest MAEs and had a lengthy computational time associated with its use.

References

1. Wyttenbach, T., & Bowers, M. T. (1999). Gas phase conformations of biological molecules: the hydrogen/deuterium exchange mechanism. *Journal of the American Society for Mass Spectrometry*, *10*(1), 9-14. doi: [http://dx.doi.org/10.1016/S1044-0305\(98\)00121-4](http://dx.doi.org/10.1016/S1044-0305(98)00121-4)
2. Becke, A. D. (1993). A new mixing of Hartree–Fock and local density-functional theories. *The Journal of Chemical Physics*, *98*(2), 1372-1377. doi:<http://dx.doi.org/10.1063/1.464304>
3. Smith, N. A., & Sadler, P. J. (2013). Photoactivatable metal complexes: from theory to applications in biotechnology and medicine. *Philosophical Transactions of the Royal Society of London A: Mathematical, Physical and Engineering Sciences*, *371*(1995), 20120519.
4. Hecht, J. (1992). *The Laser Guide Book*. United States of America: McGraw-Hill. ISBN 978-0071359672
5. Rizzo, T. R., Park, Y. D., Peteanu, L., & Levy, D. H. (1985). Electronic spectrum of the amino acid tryptophan cooled in a supersonic molecular beam. *The Journal of Chemical Physics*, *83*(9), 4819-4820. doi:<http://dx.doi.org/10.1063/1.449009>
6. Zabuga, A. V., Kamrath, M. Z., Boyarkin, O. V., & Rizzo, T. R. (2014). Fragmentation mechanism of UV-excited peptides in the gas phase. *The Journal of Chemical Physics*, *141*(15), 154309. doi:<http://dx.doi.org/10.1063/1.4897158>
7. Rosu, F., Gabelica, V., De Pauw, E., Antoine, R., Broyer, M., & Dugourd, P. (2012). UV spectroscopy of DNA duplex and quadruplex structures in the gas phase. *The Journal of Physical Chemistry A*, *116*(22), 5383-5391.
8. Talbot, F. O., Rullo, A., Yao, H., & Jockusch, R. A. (2010). Fluorescence resonance energy transfer in gaseous, mass-selected polyproline peptides. *Journal of the American Chemical Society*, *132*(45), 16156-16164.
9. Quantum Mechanical Studies of Non Covalent DNA-Protein Interactions. (2010). In C. F. Matta (Ed.), *Quantum Biochemistry: Electronic Structure and Biological Activity*. Weinheim: Wiley-VCH.
10. Ghosh, P.K. (1983). *Introduction to Photoelectron Spectroscopy*. John Wiley & Sons. ISBN 0-471-06427-0.
11. Dhandayuthapani, S., Via, L. E., Thomas, C. A., Horowitz, P. M., Deretic, D., & Deretic, V. (1995). Green fluorescent protein as a marker for gene expression and cell

biology of mycobacterial interactions with macrophages. *Molecular microbiology*, 17(5), 901-912.

12. Mooney, C. R., Horke, D. A., Chatterley, A. S., Simperler, A., Fielding, H. H., & Verlet, J. R. (2013). Taking the green fluorescence out of the protein: dynamics of the isolated GFP chromophore anion. *Chemical Science*, 4(3), 921-927.
13. Horke, D. A., & Verlet, J. R. R. (2012). Photoelectron spectroscopy of the model GFP chromophore anion. *Physical Chemistry Chemical Physics*, 14(24), 8511-8515. doi: 10.1039/C2CP40880E
14. Ullrich, S., Schultz, T., Zgierski, M. Z., & Stolow, A. (2004). Electronic relaxation dynamics in DNA and RNA bases studied by time-resolved photoelectron spectroscopy. *Physical Chemistry Chemical Physics*, 6(10), 2796-2801.
15. Chatterley, A. S., West, C. W., Roberts, G. M., Stavros, V. G., & Verlet, J. R. (2014). Mapping the ultrafast dynamics of adenine onto its nucleotide and oligonucleotides by time-resolved photoelectron imaging. *The Journal of Physical Chemistry Letters*, 5(5), 843-848.
16. De Leon, A., Jalbout, A. F., & Basiuk, V. A. (2010). [80]Fullerene–amino acid interactions: Theoretical insights. *International Journal of Quantum Chemistry*, 110(4), 953-959. doi: 10.1002/qua.21780
17. Foresman, J. B., Frisch, AE. (1996). *Exploring Chemistry with Electronic Structure Methods*. Gaussian Inc. ISBN:0-9636769-3-8
18. Macleod, N. A., & Simons, J. P. (2003). Protonated neurotransmitters in the gas-phase: clusters of 2-aminoethanol with phenol. *Physical Chemistry Chemical Physics*, 5(6), 1123-1129.
19. Ling, S., Yu, W., Huang, Z., Lin, Z., Harańczyk, M., & Gutowski, M. (2006). Gaseous arginine conformers and their unique intramolecular interactions. *The Journal of Physical Chemistry A*, 110(44), 12282-12291.
20. Plummer, C. E., Stover, M. L., Bokatzian, S. S., Davis, J. T., Dixon, D. A., & Cassady, C. J. (2015). An Experimental and Computational Study of the Gas-Phase Acidities of the Common Amino Acid Amides. *The Journal of Physical Chemistry B*.
21. Zhao, Y., Tishchenko, O., & Truhlar, D. G. (2005). How well can density functional methods describe hydrogen bonds to π acceptors? *The Journal of Physical Chemistry B*, 109(41), 19046-19051.
22. Jensen, F. (2013). *Introduction to computational chemistry*. John Wiley & Sons.

23. Řezáč, J., Nachtigallová, D., Mazzoni, F., Pasquini, M., Pietraperzia, G., Becucci, M., Hobza, P. (2015). Binding Energies of the π -Stacked Anisole Dimer: New Molecular Beam—Laser Spectroscopy Experiments and CCSD(T) Calculations. *Chemistry – A European Journal*, 21(18), 6637-6637. doi: 10.1002/chem.201500662
24. Řezáč, J., & Hobza, P. (2013). Describing Noncovalent Interactions beyond the Common Approximations: How Accurate Is the “Gold Standard,” CCSD(T) at the Complete Basis Set Limit? *Journal of Chemical Theory and Computation*, 9(5), 2151-2155. doi: 10.1021/ct400057
25. Cramer, C. J. (2013). *Essentials of computational chemistry: theories and models*. John Wiley & Sons.
26. Topol, I. A., Burt, S. K., Russo, N., & Toscano, M. (1999). Theoretical calculations of glycine and alanine gas-phase acidities. *Journal of the American Society for Mass Spectrometry*, 10(4), 318-322. doi: 10.1016/s1044-0305(98)00160-3
27. Ehrlich, S., Moellmann, J., & Grimme, S. (2012). Dispersion-corrected density functional theory for aromatic interactions in complex systems. *Accounts of chemical research*, 46(4), 916-926.
28. Grimme, S., Antony, J., Ehrlich, S., & Krieg, H. (2010). A consistent and accurate ab initio parametrization of density functional dispersion correction (DFT-D) for the 94 elements H-Pu. *The Journal of chemical physics*, 132(15), 154104.
29. Marques, M. A., & Gross, E. K. U. (2004). Time-dependent density functional theory. *Annual Review of Physical Chemistry*, 55(1), 427-455.
30. Rogers, D. M., Besley, N. A., O'Shea, P., & Hirst, J. D. (2005). Modeling the absorption spectrum of tryptophan in proteins. *The Journal of Physical Chemistry B*, 109(48), 23061-23069.
31. Fricker, S. (Ed.). (2012). *Metal compounds in cancer therapy*. Springer Science & Business Media.
32. Shaili, E. (2014). Platinum anticancer drugs and photochemotherapeutic agents: recent advances and future developments. *Science progress*, 97(1), 20-40.
33. Florea, A. M., & Büsselberg, D. (2011). Cisplatin as an anti-tumor drug: cellular mechanisms of activity, drug resistance and induced side effects. *Cancers*, 3(1), 1351-1371.
34. Kartalou, M., & Essigmann, J. M. (2001). Mechanisms of resistance to cisplatin. *Mutation Research/Fundamental and Molecular Mechanisms of Mutagenesis*, 478(1-2), 23-43. doi: [http://dx.doi.org/10.1016/S0027-5107\(01\)00141-5](http://dx.doi.org/10.1016/S0027-5107(01)00141-5)

35. Juarranz, Á., Jaén, P., Sanz-Rodríguez, F., Cuevas, J., & González, S. (2008). Photodynamic therapy of cancer. Basic principles and applications. *Clinical and Translational Oncology*, 10(3), 148-154.
36. Wan, M. T., & Lin, J. Y. (2014). Current evidence and applications of photodynamic therapy in dermatology. *Clinical, cosmetic and investigational dermatology*, 7, 145.
37. Knoll, J. D., & Turro, C. (2015). Control and utilization of ruthenium and rhodium metal complex excited states for photoactivated cancer therapy. *Coordination chemistry reviews*, 282, 110-126.
38. Farrer, N. J., Salassa, L., & Sadler, P. J. (2009). Photoactivated chemotherapy (PACT): the potential of excited-state d-block metals in medicine. *Dalton Transactions*, (48), 10690-10701.
39. Bednarski, P. J., Mackay, F. S., & Sadler, P. J. (2007). Photoactivatable platinum complexes. *Anti-Cancer Agents in Medicinal Chemistry (Formerly Current Medicinal Chemistry-Anti-Cancer Agents)*, 7(1), 75-93.
40. Zhao, Y., Roberts, G. M., Greenough, S. E., Farrer, N. J., Paterson, M. J., Powell, W. H., ... & Sadler, P. J. (2012). Two-Photon-Activated Ligand Exchange in Platinum (II) Complexes. *Angewandte Chemie*, 124(45), 11425-11428.
41. Sen, A., & Dessent, C. E. (2014). Mapping the UV Photophysics of Platinum Metal Complexes Bound to Nucleobases: Laser Spectroscopy of Isolated Uracil· Pt (CN) 4²⁻–and Uracil· Pt (CN) 6²⁻–Complexes. *The Journal of Physical Chemistry Letters*, 5(19), 3281-3285.
42. Sen, A., Luxford, T. F., Yoshikawa, N., & Dessent, C. E. (2014). Solvent evaporation versus proton transfer in nucleobase–Pt (CN) 4²⁻, 6²⁻–dianion clusters: a collisional excitation and electronic laser photodissociation spectroscopy study. *Physical Chemistry Chemical Physics*, 16(29), 15490-15500.
43. Sen, A., & Dessent, C. E. (2014). Communication: Photoactivation of nucleobase bound platinum II metal complexes: Probing the influence of the nucleobase. *The Journal of chemical physics*, 141(24), 241101.
44. Rafique, S., Idrees, M., Nasim, A., Akbar, H., & Athar, A. (2010). Transition metal complexes as potential therapeutic agents. *Biotechnology and Molecular Biology Reviews*, 5(2), 38-45.
45. Lumpkin, R. S., Kober, E. M., Worl, L. A., Murtaza, Z., & Meyer, T. J. (1990). Metal-to-ligand charge-transfer (MLCT) photochemistry: experimental evidence for the participation of a higher lying MLCT state in polypyridyl complexes of ruthenium (II) and osmium (II). *Journal of Physical Chemistry*, 94(1), 239-243.

46. Cárdenas-Jirón, G. I., Barboza, C. A., López, R., & Menéndez, M. I. (2011). Theoretical study on the electronic excitations of a porphyrin-polypyridyl ruthenium (II) photosensitizer. *The Journal of Physical Chemistry A*, 115(43), 11988-11997.
47. Cao, G.-J., Xu, H.-G., Li, R.-Z., & Zheng, W. (2012). Hydrogen bonds in the nucleobase-gold complexes: Photoelectron spectroscopy and density functional calculations. *The Journal of Chemical Physics*, 136(1), 014305. doi:<http://dx.doi.org/10.1063/1.367194>
48. Ullrich, C. A.; Yang, Z.-h. (2014). A brief compendium of time-dependent density functional theory. *Brazilian Journal of Physics*, 44 (1), 154-188.
49. Sholl, D.; Steckel, J. A. (2011). *Density functional theory: a practical introduction*. John Wiley & Sons.
50. Born, M.; Oppenheimer, J. R. (1927). On the Quantum Theory of Molecules. *Annalen der Physik*, 84 (457).
51. Parr, R. G.; Ghosh, S. K. (1986). Thomas-Fermi theory for atomic systems. *Proceedings of the National Academy of Sciences*, 83 (11), 3577-3579.
52. Burke, K.; Wagner, L. O. (2013). DFT in a nutshell. *International Journal of Quantum Chemistry*, 113 (2), 96-101.
53. Morgan III, J., Thomas-Fermi and Other Density-Functional Theories. In *Springer Handbook of Atomic, Molecular, and Optical Physics*, Drake, G., Ed. Springer New York: 2006; 295-306.
54. Hohenberg, P.; Kohn, W. (1964). Inhomogeneous electron gas. *Physical review*, 136 (3B), B864.
55. Capelle, K. (2006). A bird's-eye view of density-functional theory. *Brazilian Journal of Physics*, 36 (4A), 1318-1343.
56. Kohn, W.; Sham, L. J. (1965). Self-Consistent Equations Including Exchange and Correlation Effects. *Physical Review*, 140 (4A), A1133-A1138.
57. Peverati, R.; Truhlar, D. G. (2014). Quest for a universal density functional: the accuracy of density functionals across a broad spectrum of databases in chemistry and physics. *Philosophical Transactions of the Royal Society of London A: Mathematical, Physical and Engineering Sciences*, 372.
58. Becke, A. D., Density-functional thermochemistry. III (1993). The role of exact exchange. *The Journal of Chemical Physics*, 98 (7), 5648-5652;
59. Adamo, C.; Barone, V. (1999). Toward reliable density functional methods without adjustable parameters: The PBE0 model. *The Journal of Chemical Physics*, 110 (13), 6158-6170.

60. Lee, C.; Yang, W.; Parr, R. G. (1988). Development of the Colle-Salvetti correlation-energy formula into a functional of the electron density. *Physical Review B*, 37 (2), 785-789.
61. Yanai, T.; Tew, D. P.; Handy, N. C. (2004). A new hybrid exchange–correlation functional using the Coulomb-attenuating method (CAM-B3LYP). *Chemical Physics Letters*, 393 (1–3), 51-57.
62. Kobayashi, R.; Amos, R. D. (2006). The application of CAM-B3LYP to the charge-transfer band problem of the zincbacteriochlorin–bacteriochlorin complex. *Chemical Physics Letters*, 420 (1–3), 106-109.
63. Wong, B. M., & Hsieh, T. H. (2010). Optoelectronic and excitonic properties of oligoacenes: substantial improvements from range-separated time-dependent density functional theory. *Journal of chemical theory and computation*, 6(12), 3704-3712.
64. Jensen, L.; Govind, N. (2009). Excited States of DNA Base Pairs Using Long-Range Corrected Time-Dependent Density Functional Theory. *The Journal of Physical Chemistry A*, 113 (36), 9761-9765.
65. Zhao, Y.; Truhlar, D. (2008). The M06 suite of density functionals for main group thermochemistry, thermochemical kinetics, noncovalent interactions, excited states, and transition elements: two new functionals and systematic testing of four M06-class functionals and 12 other functionals. *Theoretical Chemistry Accounts*, 120 (1-3), 215-241.
66. Peverati, R.; Truhlar, D. G. (2011). Improving the Accuracy of Hybrid Meta-GGA Density Functionals by Range Separation. *The Journal of Physical Chemistry Letters*, 2 (21), 2810-2817.
67. Aquino, A. J. A.; Nachtigallova, D.; Hobza, P.; Truhlar, D. G.; Hättig, C.; Lischka, H. (2011). The charge-transfer states in a stacked nucleobase dimer complex: A benchmark study. *Journal of Computational Chemistry*, 32 (7), 1217-1227.
68. Yu, H. S.; Zhang, W.; Verma, P.; He, X.; Truhlar, D. G. (2015). Nonseparable exchange-correlation functional for molecules, including homogeneous catalysis involving transition metals. *Physical Chemistry Chemical Physics*, 17 (18), 12146-12160.
69. Peverati, R.; Truhlar, D. G. (2012). Screened-exchange density functionals with broad accuracy for chemistry and solid-state physics. *Physical Chemistry Chemical Physics*, 14 (47), 16187-16191.
70. Marques, M. L.; Gross, E. U. (2003). Time-Dependent Density Functional Theory. In *A Primer in Density Functional Theory*, Springer Berlin Heidelberg, 620, 144-184.
71. Elliott, P.; Furche, F.; Burke, K. (2009). Excited States from Time-Dependent Density Functional Theory. In *Reviews in Computational Chemistry*, John Wiley & Sons, Inc, 91-165.

72. Gross, E. U.; Maitra, N. (2012). Introduction to TDDFT. In *Fundamentals of Time-Dependent Density Functional Theory*. Springer Berlin Heidelberg, 201 (837), 53-99.
73. Tai, H.-C.; Zhao, Y.; Farrer, N. J.; Anastasi, A. E.; Clarkson, G.; Sadler, P. J.; Deeth, R. J. (2012). A Computational Approach to Tuning the Photochemistry of Platinum (IV) Anticancer Agents. *Chemistry – A European Journal*, 18 (34), 10630-10642.
74. Varsano, D.; Di Felice, R.; Marques, M. A. L.; Rubio, A. (2006). A TDDFT Study of the Excited States of DNA Bases and Their Assemblies. *The Journal of Physical Chemistry B*, 110 (14), 7129-7138; Tsolakidis, A.; Kaxiras, E. (2005). A TDDFT Study of the Optical Response of DNA Bases, Base Pairs, and Their Tautomers in the Gas Phase. *The Journal of Physical Chemistry A*, 109 (10), 2373-2380.
75. Gupta, V. P. (2015). *Principles and Applications of Quantum Chemistry*. Elsevier Science.
76. Evarestov, R. A. (2013). *Quantum Chemistry of Solids: LCAO Treatment of Crystals and Nanostructures*. Springer Berlin Heidelberg.
77. Ren, H.-S.; Li, Y.-K.; Zhu, Q.; Zhu, J.; Li, X.-Y. (2012). Spectral shifts of the $n \rightarrow \pi^*$ and $\pi \rightarrow \pi^*$ transitions of uracil based on a modified form of solvent reorganization energy. *Physical Chemistry Chemical Physics*, 14 (38), 13284-13291.
78. Improtà, R., & Barone, V. (2004). Absorption and fluorescence spectra of uracil in the gas phase and in aqueous solution: A TD-DFT quantum mechanical study. *Journal of the American Chemical Society*, 126(44), 14320-14321.
79. Weigend, F.; Ahlrichs, R. (2005). Balanced basis sets of split valence, triple zeta valence and quadruple zeta valence quality for H to Rn: Design and assessment of accuracy. *Physical Chemistry Chemical Physics*, 7 (18), 3297-3305.
80. Wu, Y., Shan, G. G., Li, H. B., Wu, S. X., Ren, X. Y., Geng, Y., & Su, Z. M. (2015). Correction: Theoretical study and design of multifunctional phosphorescent platinum (II) complexes containing triarylboron moieties for efficient OLED emitters. *Physical Chemistry Chemical Physics*, 17(6), 4771-4771.
81. Tao, J.; Perdew, J. P.; Staroverov, V. N.; Scuseria, G. E. (2003). Climbing the density functional ladder: Nonempirical meta-generalized gradient approximation designed for molecules and solids. *Physical Review Letters*, 91 (14), 146401.
82. O Dohn, A.; B Moller, K.; PA Sauer, S. (2013). Optimizing the structure of Tetracyanoplatinate (II): a comparison of relativistic density functional theory methods. *Current Inorganic Chemistry*, 3 (3), 213-219.
83. Becke, A. D. (1988). Density-functional exchange-energy approximation with correct asymptotic behavior. *Physical Review A*, 38 (6), 3098-3100.

84. Shukla, M. K.; Leszczynski, J. (2004). TDDFT investigation on nucleic acid bases: Comparison with experiments and standard approach. *Journal of Computational Chemistry*, 25 (5), 768-778.
85. Zhang, L.; Tian, L.; Li, M.; He, R.; Shen, W. (2014). A theoretical study on tuning the electronic structures and photophysical properties of newly designed platinum(II) complexes by adding substituents on functionalized ligands as highly efficient OLED emitters. *Dalton Transactions*, 43 (17), 6500-12.
86. Abdel Ghani, N. T.; Mansour, A. M. (2011). Novel Pd(II) and Pt(II) complexes of N,N-donor benzimidazole ligand: Synthesis, spectral, electrochemical, DFT studies and evaluation of biological activity. *Inorganica Chimica Acta*, 373 (1), 249-258.
87. DeFusco, A., Ivanic, J., Schmidt, M. W., & Gordon, M. S. (2011). Solvent-induced shifts in electronic spectra of uracil. *The Journal of Physical Chemistry A*, 115(18), 4574-4582.
88. Das I. 2012. An Introduction To Physical Chemistry. New Age International (P) Limited.
89. Lewars, E. G. (2010). *Computational Chemistry: Introduction to the Theory and Applications of Molecular and Quantum Mechanics*. Springer Netherlands.
90. Skyner, R. E.; McDonagh, J. L.; Groom, C. R.; van Mourik, T.; Mitchell, J. B. O. (2015). A review of methods for the calculation of solution free energies and the modelling of systems in solution. *Physical Chemistry Chemical Physics*, 17 (9), 6174-6191.
91. Tomasi, J.; Mennucci, B.; Cammi, R. (2005). Quantum mechanical continuum solvation models. *Chemical reviews*, 105 (8), 2999-3094.
92. Tomasi, J.; Mennucci, B. (2002). Self-consistent Reaction Field Methods. In *Encyclopedia of Computational Chemistry*, John Wiley & Sons, Ltd.
93. Han, D.; Wu, Y.; Cai, H.; Pang, C.; Zhao, L. (2015). DFT/TDDFT investigation on the electronic structures and photophysical properties of a series of substituted N-heterocyclic carbene (NHC) platinum(II) complexes. *Synthetic Metals*, 209, 455-460.
94. Gustavsson, T.; Bányász, Á.; Lazzarotto, E.; Markovitsi, D.; Scalmani, G.; Frisch, M. J.; Barone, V.; Improta, R. (2006). Singlet Excited-State Behavior of Uracil and Thymine in Aqueous Solution: A Combined Experimental and Computational Study of 11 Uracil Derivatives. *Journal of the American Chemical Society*, 128 (2), 607-619.
95. Frisch, M. J.; Trucks, G. W.; Schlegel, H. B.; Scuseria, G. E.; Robb, M. A.; Cheeseman, J. R.; Scalmani, G.; Barone, V.; Mennucci, B.; Petersson, G. A.; Nakatsuji, H.; Caricato, M.; Li, X.; Hratchian, H. P.; Izmaylov, A. F.; Bloino, J.; Zheng, G.; Sonnenberg, J. L.; Hada, M.; Ehara, M.; Toyota, K.; Fukuda, R.; Hasegawa, J.; Ishida, M.; Nakajima, T.; Honda, Y.; Kitao, O.; Nakai, H.; Vreven, T.; Montgomery Jr., J. A.; Peralta, J. E.; Ogliaro, F.; Bearpark, M. J.; Heyd, J.; Brothers,

- E. N.; Kudin, K. N.; Staroverov, V. N.; Kobayashi, R.; Normand, J.; Raghavachari, K.; Rendell, A. P.; Burant, J. C.; Iyengar, S. S.; Tomasi, J.; Cossi, M.; Rega, N.; Millam, N. J.; Klene, M.; Knox, J. E.; Cross, J. B.; Bakken, V.; Adamo, C.; Jaramillo, J.; Gomperts, R.; Stratmann, R. E.; Yazyev, O.; Austin, A. J.; Cammi, R.; Pomelli, C.; Ochterski, J. W.; Martin, R. L.; Morokuma, K.; Zakrzewski, V. G.; Voth, G. A.; Salvador, P.; Dannenberg, J. J.; Dapprich, S.; Daniels, A. D.; Farkas, Ö.; Foresman, J. B.; Ortiz, J. V.; Cioslowski, J.; Fox, D. J. (2009). *Gaussian 09*, Gaussian, Inc.: Wallingford, CT, USA.
96. Tomasi, J.; Mennucci, B.; Cancès, E. (1999). The IEF version of the PCM solvation method: an overview of a new method addressed to study molecular solutes at the QM ab initio level. *Journal of Molecular Structure: THEOCHEM*, 464 (1–3), 211-226.
 97. King, S. B.; Yandell, M. A.; Stephansen, A. B.; Neumark, D. M. (2014). Time-resolved radiation chemistry: Dynamics of electron attachment to uracil following UV excitation of iodide-uracil complexes. *The Journal of Chemical Physics*, 141 (22), 224310.
 98. King, S. B.; Yandell, M. A.; Neumark, D. M. (2013). Time-resolved photoelectron imaging of the iodide-thymine and iodide-uracil binary cluster systems. *Faraday Discussions*, 163, 59-72; discussion 117-38.
 99. King, S. B.; Stephansen, A. B.; Yokoi, Y.; Yandell, M. A.; Kunin, A.; Takayanagi, T.; Neumark, D. M. (2015). Electron accommodation dynamics in the DNA base thymine. *The Journal of Chemical Physics*, 143 (2), 024312.
 100. Chai, J.-D.; Head-Gordon, M. (2008) Long-range corrected hybrid density functionals with damped atom-atom dispersion corrections. *Physical Chemistry Chemical Physics*, 10 (44), 6615-6620.
 101. Mak, C. C.; Peslherbe, G. H. (2014). Relaxation Pathways of Photoexcited Iodide–Methanol Clusters: A Computational Investigation. *The Journal of Physical Chemistry A*, 118 (25), 4494-4501.
 102. Hay, P. J.; Wadt, W. R. (1985). Ab initio effective core potentials for molecular calculations. Potentials for K to Au including the outermost core orbitals. *The Journal of Chemical Physics*, 82 (1), 299-310; McLean, A. D.; Chandler, G. S. (1980). Contracted Gaussian basis sets for molecular calculations. I. Second row atoms, Z=11–18. *The Journal of Chemical Physics* 72 (10), 5639-5648; Weigend, F.; Ahlrichs, R. (2005). Balanced basis sets of split valence, triple zeta valence and quadruple zeta valence quality for H to Rn: Design and assessment of accuracy. *Physical Chemistry Chemical Physics*, 7 (18), 3297-3305.
 103. Gabelica, V. (2014). *Nucleic Acids in the Gas Phase*. Springer Berlin Heidelberg
 104. Leszczynski, J. (2003). Uracil and Thymine. In *Computational Chemistry: Reviews of Current Trends*, Leszczynski, J., Ed. World Scientific Publishing, 8, 290-304.

105. Pluta, T.; Kolaski, M.; Medved', M.; Budzák, Š. (2012). Dipole moment and polarizability of the low-lying excited states of uracil. *Chemical Physics Letters*, 546, 24-29.
106. Vydrov, O. A.; Scuseria, G. E. (2006). Assessment of a long-range corrected hybrid functional. *The Journal of Chemical Physics*, 125 (23), 234109.
107. Zhao, Y.; Pu, J.; Lynch, B. J.; Truhlar, D. G. (2004). Tests of second-generation and third-generation density functionals for thermochemical kinetics. *Physical Chemistry Chemical Physics*, 6 (4), 673-676; Rohrdanz, M. A.; Martins, K. M.; Herbert, J. M., (2009). A long-range-corrected density functional that performs well for both ground-state properties and time-dependent density functional theory excitation energies, including charge-transfer excited states. *The Journal of Chemical Physics*, 130 (5), 054112.
108. Peach, M. J. G.; Helgaker, T.; Salek, P.; Keal, T. W.; Lutnaes, O. B.; Tozer, D. J.; Handy, N. C. (2006). Assessment of a Coulomb-attenuated exchange-correlation energy functional. *Physical Chemistry Chemical Physics*, 8 (5), 558-562.
109. Spackman, M. A.; Weber, H. P.; Craven, B. M., Energies of molecular interactions from Bragg diffraction data (1988). *Journal of the American Chemical Society*, 110 (3), 775-782; Kazakevich, Y. V.; El'tekov, Y. A. (1987). Adsorption of Nucleic Bases on Modified Silicas. *Russian Journal of Physical Chemistry*, 61 (2), 233 - 234.
110. Ran, J.; Hobza, P. (2009). Nature of Bonding in Nine Planar Hydrogen-Bonded Adenine...Thymine Base Pairs. *The Journal of Physical Chemistry B*, 113 (9), 2933-2936.
111. Preuss, M.; Schmidt, W. G.; Seino, K.; Furthmuller, J.; Bechstedt, F. (2004). Ground- and excited-state properties of DNA base molecules from plane-wave calculations using ultrasoft pseudopotentials. *Journal of Computational Chemistry*, 25 (1), 112-22.
112. Nitta, H.; Kawata, I. (2012). A close inspection of the charge-transfer excitation by TDDFT with various functionals: An application of orbital- and density-based analyses. *Chemical Physics*, 405, 93-99; Dreuw, A.; Head-Gordon, M. (2004). Failure of Time-Dependent Density Functional Theory for Long-Range Charge-Transfer Excited States: The Zincbacteriochlorin–Bacteriochlorin and Bacteriochlorophyll–Spheroidene Complexes. *Journal of the American Chemical Society* 126 (12), 4007-4016.
113. Gutowski, M.; Skurski, P.; Jordan, K. D.; Simons, J. (1997). Energies of dipole-bound anionic states. *International journal of quantum chemistry*, 64 (2), 183-191.
114. Fortenberry, R. C.; Lukemire, J. A. (2015). Electronic and rovibrational quantum chemical analysis of C3P⁻: the next interstellar anion? *Monthly Notices of the Royal Astronomical Society* 453 (3), 2824-2829.
115. Theis, M. L.; Candian, A.; Tielens, A. G. G. M.; Lee, T. J.; Fortenberry, R. C. (2015). Electronically Excited States of Anisotropically Extended Singly-Deprotonated PAH Anions. *The Journal of Physical Chemistry A* 119 (52), 13048-13054.

116. Stephansen, A. B.; King, S. B.; Yokoi, Y.; Minoshima, Y.; Li, W.-L.; Kunin, A.; Takayanagi, T.; Neumark, D. M. (2015). Dynamics of dipole- and valence bound anions in iodide-adenine binary complexes: A time-resolved photoelectron imaging and quantum mechanical investigation. *The Journal of Chemical Physics*, *143* (10), 104308.
117. Dunning, T. H. (1989). Gaussian basis sets for use in correlated molecular calculations. I. The atoms boron through neon and hydrogen. *The Journal of Chemical Physics*, *90* (2), 1007-1023.
118. Wysokiński, R.; Hernik, K.; Szostak, R.; Michalska, D. (2007). Electronic structure and vibrational spectra of cis-diammine(oxalato)platinum(II), a potential cisplatin analogue: DFT and experimental study. *Chemical Physics*, *333* (1), 37-48;
119. Gao, H. (2011). Theoretical studies of molecular structures and properties of platinum (II) antitumor drugs. *Spectrochimica Acta Part A: Molecular and Biomolecular Spectroscopy*, *79* (3), 687-693;
120. Wang, X.-B.; Wang, Y.-L.; Woo, H.-K.; Li, J.; Wu, G.-S.; Wang, L.-S. (2006). Free tetra- and hexa-coordinated platinum-cyanide dianions, and : A combined photodetachment photoelectron spectroscopic and theoretical study. *Chemical Physics*, *329* (1-3), 230-238.
121. Perdew, J. P.; Chevary, J. A.; Vosko, S. H.; Jackson, K. A.; Pederson, M. R.; Singh, D. J.; Fiolhais, C. (1992). Atoms, molecules, solids, and surfaces: Applications of the generalized gradient approximation for exchange and correlation. *Physical Review B: Condensed Matter and Materials Physics*, *46* (11), 6671-6687.
122. Wang, F.; Ziegler, T.; van Lenthe, E.; van Gisbergen, S.; Baerends, E. J. (2005). The calculation of excitation energies based on the relativistic two-component zeroth-order regular approximation and time-dependent density-functional with full use of symmetry. *The Journal of Chemical Physics*, *122* (20), 204103.
123. Wang, F.; Ziegler, T. (2005). Theoretical study of the electronic spectra of square-planar platinum (II) complexes based on the two-component relativistic time-dependent density-functional theory. *The Journal of Chemical Physics*, *123* (19), 194102.
124. Milner, E. M.; Nix, M. G. D.; Dessent, C. E. H. (2011). Evidence for hydrogen bond network formation in microsolvated clusters of Pt(CN)₄²⁻: collision induced dissociation studies of Pt(CN)₄²⁻·(H₂O)_n n = 1-4, and Pt(CN)₄²⁻·(MeCN)_m m = 1, 2 cluster ions. *Physical Chemistry Chemical Physics*, *13* (41), 18379-18385.
125. Zhao, Y.; Truhlar, D. G. (2008). Density Functionals with Broad Applicability in Chemistry. *Accounts of Chemical Research*, *41* (2), 157-167; Peverati, R.; Truhlar, D.

- G. (2014). Quest for a universal density functional: the accuracy of density functionals across a broad spectrum of databases in chemistry and physics. *Philosophical Transactions of the Royal Society of London A: Mathematical, Physical and Engineering Sciences*, 372
126. Zhao, Y.; Truhlar, D. G. (2006). A new local density functional for main-group thermochemistry, transition metal bonding, thermochemical kinetics, and noncovalent interactions. *The Journal of Chemical Physics*, 125 (19), 194101; Peverati, R.; Truhlar, D. G. (2012). M11-L: A Local Density Functional That Provides Improved Accuracy for Electronic Structure Calculations in Chemistry and Physics. *The Journal of Physical Chemistry Letters*, 3 (1), 117-124.
127. Mason, W. R.; Gray, H. B. (1968). ELECTRONIC STRUCTURES OF SQUARE-PLANAR COMPLEXES. *Journal of the American Chemical Society*, 90 (21), 5721
128. Pernpointner, M. (2007). A fully relativistic study of the and photodetachment spectra. *Chemical Physics*, 338 (1), 44-52.
129. Gasser, G., Ott, I., & Metzler-Nolte, N. (2011). Organometallic Anticancer Compounds. *Journal of Medicinal Chemistry*, 54(1), 3-25.
130. Lottner, C., Knuechel, R., Bernhardt, G., & Brunner, H. (2004). Combined chemotherapeutic and photodynamic treatment on human bladder cells by hematoporphyrin–platinum(II) conjugates. *Cancer Letters*, 203(2), 171-180.
131. Muhammad, N., & Guo, Z. (2014). Metal-based anticancer chemotherapeutic agents. *Current Opinion in Chemical Biology*, 19, 144-153.
132. Zhang, C. X., & Lippard, S. J. (2003). New metal complexes as potential therapeutics. *Current Opinion in Chemical Biology*, 7(4), 481-489.
133. Wheate, N. J., Walker, S., Craig, G. E., & Oun, R. (2010). The status of platinum anticancer drugs in the clinic and in clinical trials. [10.1039/C0DT00292E]. *Dalton Transactions*, 39(35), 8113-8127.
134. Bruijninx, P. C. A., & Sadler, P. J. (2008). ‘New Trends for Metal Complexes with Anticancer Activity’. *Current opinion in chemical biology*, 12(2), 197-206.
135. Clarke, M. J., & Sadler, P. J. (2013). *Metallopharmaceuticals I: DNA Interactions* (Vol. 1): Springer Science & Business Media.
136. Cubo, L., Pizarro, A. M., Quiroga, A. G., Salassa, L., Navarro-Ranninger, C., & Sadler, P. J. (2010). Photoactivation of trans diamine platinum complexes in aqueous solution and effect on reactivity towards nucleotides. *Journal of Inorganic Biochemistry*, 104(9), 909-918.

137. Peach, M. J. G., Benfield, P., Helgaker, T., & Tozer, D. J. (2008). Excitation energies in density functional theory: An evaluation and a diagnostic test. *The Journal of Chemical Physics*, 128(4), 044118.